SPECIFIC ION EFFECTS ON TRANSIENT POLYMERS: A NEW STRATEGY FOR PROGRAMMABLE MICROCAPUSLES

BY

SHIJIA TANG

DISSERTATION

Submitted in partial fulfillment of the requirements
for the degree of Doctor of Philosophy in Materials Science and Engineering
in the Graduate College of the
University of Illinois at Urbana-Champaign, 2018

Urbana, Illinois

Doctoral Committee:

Professor Jeffrey S. Moore, Chair
Professor Paul V. Braun
Assistant Professor Qian Chen
Assistant Professor Christopher M. Evans

ABSTRACT

Transient polymers are emerging materials that transform from macromolecules to small molecules triggered by predefined environmental stimuli. Distinct from traditional degradable polymers, transient materials undergo domino like chain unzipping reactions, leading to controlled and complete depolymerization upon one cleavage. Taking advantage of the unique feature of triggered materials transience, this dissertation focuses on developing transient polymer microcapsules for programmable payload release. In Chapter 2, a rapid solvent evaporation strategy was developed to prepare transient polymer microcapsules with a low-ceiling-temperature polymer, cyclic poly(phthalaldehyde) (cPPA), as the shell wall materials. Chapter 3 described an ion co-activation effect that modulated cPPA depolymerization rates in the presence of acid. In Chapter 4, we further investigated the ion specificity in the co-activation effect and anion solvation properties were found to significantly impact the co-activation behavior. Based on the specific ion co-activation effect, we developed programmable microcapsules whose payload release kinetics depends on the ionic species in the solutions. Chapter 5 further expanded the co-activation effect in Lewis acid solutions that achieved depolymerization in mild environment. In Chapter 6, several studies were devoted to understand the molecular and interfacial mechanisms of the ion co-activation effect. Chapter 7 reviewed current topics on the Hofmeister effect and constructed a crude model on auto-catalytic microcapsules. The thesis research offers an encapsulation strategy and ion library for triggered release microcapsules and will be of significance for designing logic gate responsive microcapsules, reversible activation-deactivation materials and self-regulating reaction networks in autonomous chemical system.

ACKNOWLEDGEMENTS

When I am asked what the most important accomplishment I have achieved is, I always answer that I am most proud of this experience in University of Illinois and being a Moore group alumni. This journey is not only a record of research contribution but also a record of myself growing into a stronger and independent researcher. I will always cherish the invaluable experience I have gained in the University of Illinois. And of course, I have received countless inspirations from excellent advisors, collaborators, colleagues and friends. It is their support, intelligence, patience that have resulted in the work today.

First, I would like to thank my advisor Prof. Jeffrey Moore. Jeff is undoubtedly the most amazing professor/educator/advisor. I have known the research in the Moore group when I read a paper about self-healing materials in my sophomore year. Coming to the University of Illinois and joining the legendary Moore group is definitely a dream comes true. I really appreciate Jeff offers me the opportunity to join the group. Over the years, Jeff has influenced me with his research and life philosophy and set excellent examples in my future career. He also trained me to be a stronger and independent researcher and person. The conversations I had with Jeff are beneficial for my professional and personal life. I would also like to thank my thesis committee members, Prof. Paul Braun, Prof. Qian Chen, and Prof. Chris Evans. We had fruitful discussions during my prelim exam and this thesis research has received their invaluable suggestions, guidance and encouragement.

I also have the honor to be an AMS group member. I am thankful to work in the BP project and collaborate with Prof. Nancy Sottos, Prof. Scott White, Dr. Mostafa Yourdkhani, Shuqi Lai, Thu Doan and Mike Odarczenko. We had a lot of fruitful discussions and I gained

countless feedback from these creative and talented researchers during BP subgroup meetings and AMS group meetings. I have learned the encapsulation technologies from the world class research group. And attending AMS group meeting is always inspiring and I have learned that the true beauty of research comes from the interdisciplinary minds and collaborations.

Special thanks to Liuyan Tang. She is a talented student and my research "sister" and has fighted with me shoulder by shoulder during the hardest part of my PHD. I will always remember Dec/31/2016, when we finally determined the ion co-activation effect after struggling for two months. We had a lot of discussions and healthy debate for research projects. I also would like to thank Dr. Yang Song, Dr. Ke Yang, and Dr. Hefei Dong for their tremendous help during the time spending together in the office. We had great time chatting and hanging out together in the lab and outside the office sharing research and life experience. We have had many phone calls after they graduate and they supported my research and gave me career advice. I also would like to thank Anna Yang for helping me overcome research difficulties, brainstorming in the café, and guiding me to grow spiritually.

I also have received great help and feedback in my research from Dr. Xing Jiang, Dr. Xiaocun Lu, Dr. Adam Feinberg, Dr. Vivian Lau, Dr. Gabe Rudebusch, Dr. Charles Diesendruck, Dr. Catherine Possanza Casey, Dr. Josh Grolman, Dr. Josh Kaitz, Dr. Olivia Lee, Dr. Windy Santa Cruz, Dr. Pin-Nan Cheng, Dr. Jun Li and Huiying Liu. Their passion about research, creativity and pursuit to perfection motivates me to be a better researcher and grow significantly.

I also would like to thank the help I have received from the talented students and postdocs in the past and current Moore group: Dr.Tomohiro Shiraki, Dr. Maxwell Robb, Dr. Ian Robertson, Jose Zavala, Abigail Halmes, Po Yang, and Hao Yu. Also thanks to RAL Crew: Dr.

Bora Inci, Dr. Semin Lee, Dr. Scott Sisco Dr. Nina Sekerak, Dr. James Herbison, Dr. Michael Evans, Dr. Yi Ren, Dr. Nagarjuna Gavvalapalli, Dr. Nagamani Chikkanagari, Dr. Etienne Chenard, Dr. Shawn Miller, Dr. Kristin Hutchins, Dr. Yu Cao, Dr. Yun Liu, Dr. Lily Robertson, Dr. Ken Schwieter, Dr. Haibin Wei, Kevin Cheng, Anderson Coates, Chris Pattillo, Timothy Moneypenny, and Chengtian Shen. I also would like to thank my undergraduate students: Wenfei Liu, Hanqing Ye, and Justin Shang. It is have been lot of fun to work with you. I am proud of everything you have accomplished and I wish you the very best in your future career. Last but not least, I would like to thank Ashley Trimmell who has been managing the group business. She helps me a lot with placing orders, schedule meetings and always be there for me to bother and ask a lot of questions.

I also would like to thank all the friends I have met in the University of Illinois and all my friends in the US and China. No one can survive grad school alone. Even though we are from different departments, programs and we each have our own challenges, you are always there for me to share the thick and the thin. Thank you for all your support and I wish you the best in your professional and personal life: Dr. Ruizhi Li, Dr. Zehua Bao, Dr. Yue Wu, Dr. Liang Liu, Le Wang, Binyue Hou, Hui Li, Xuejin Zhang and Emma Li.

I also want to thank my parents. You are the best parents and always love me and are proud of me. I am always looking forward to our weekly calls to share our daily lives and stories. You have inspired me to be a better person and a better researcher. I also would like to thank my boyfriend, Andrea Alberti, my family in Champaign-Urbana. Meeting Andrea is one of the best things happening to me and I know it is God who have sent you to take care of me. We have created many beautiful memories and I am looking forward to create many more. Last, I would like to thank God for bringing me to UIUC and guide me along the way. I cannot express how

grateful and blessed I feel to have learned more about you in the past few years. I am thankful for all the prayers and guidance that shape me into a better person.

TABLE OF CONTENTS

CHAPTER 1 : INTRODUCTION 1
1.1 Overview of Polymer Microcapsules and Triggered Release 1
1.2 Microencapsulation Methodologies for Core-Shell Microcapsules 4
1.3 Strategies for Environmentally Triggered Microcapsules 9
1.4 Transient Polymers as Shell Wall Materials for Triggered Release Microcapsules 12
1.5 References 17

CHAPTER 2 : LOW-CEILING-TEMPERATURE POLYMER MICROCAPSULES WITH HYDROPHOBIC PAYLOADS *VIA* RAPID SOLVENT EVAPORATION……..24
2.1 Introduction 24
2.2 Kinetically Trapped Core-Shell cPPA Microcapsules *via* Rapid Solvent Evaporation 27
2.3 Effect of Materials Compositions on Microcapsule's Morphology and Loading 41
2.4 Acid Triggered Payload Release Profiles from cPPA Microcapsules 45
2.5 Generality of the Rapid Solvent Evaporation Method to Alternative Core and Shell Wall Materials 46
2.6 Experimental Details 49
2.7 References 56

CHAPTER 3 : INVESTIGATING ION CO-ACTIVATION EFFECT ON TRANSIENT POLYMER MICROCAPSULES 60
3.1 Introduction 60
3.2 Ion Co-Activation Effect of LiCl on cPPA Microcapsule's Shell Wall Depolymerization 61
3.3 Ion Co-Activation Effect of LiCl in Alternative Acid Solutions 68
3.4 Control Experiments to Validate the Co-Activation Effect of LiCl 71
3.5 Experimental Details 75
3.6 References 83

CHAPTER 4 : PROGRAMMABLE PAYLOAD RELEASE TRIGGERED BY A SPECIFIC ION CO-ACTIVATION EFFECT……85
4.1 Introduction 85
4.2 Ion Specificity in the Co-Activation Effect 86
4.3 Concentration Dependence in the Specific Ion Co-Activation Effect 95

4.4 Payload Release Rates Modulated by the Specific Ion Co-Activation Effect 97
4.5 Experimental Details 98
4.6 References 108

CHAPTER 5: DEPOLYMERIZATION TRIGGERED BY LEWIS ACIDS AND COACTIVATORS……..……..111
5.1 Introduction 111
5.2 Effect of Lewis Acids on cPPA Depolymerization 112
5.3 Ion Co-activation Effects in Lewis Acid Solutions 115
5.4 Experimental Details 117
5.5 References 121

CHAPTER 6 : EFFORTS TOWARDS MECHANISMS OF SPECIFIC ION CO-ACTIVATION EFFECT ON TRANSIENT POLYMER MICROCAPSULES……...……122
6.1 Introduction……122
6.2 Specific Ion Co-Activation Effect in Homogeneous and Heterogeneous Systems……..124
6.3 Probe Co-Activation Effect on Depolymerization Intermediates……...…..126
6.4 Summary: Proposed Approaches to Assign Multi-Scale Contributions in the Specific Ion Co-Activation Effect……131
6.5 Experimental Details……..134
6.6 References……..…….……...136

CHAPTER 7 : OUTLOOK: HOFMEISTER EFFECT ON MACROMOLECULES AND POTENTIAL APPLICATIONS IN AUTOCATALYTIC PAYLOAD RELEASE FROM TRANSIENT POLYMER MICROCAPSULES……137
7.1 Motivation……..137
7.2 Current State of Hofmeister Effect……...……137
7.3 Models for Autocatalytic Payload Release from Transient Polymer Microcapsules…...141
7.4 References...……...……147

CHAPTER 1 : INTRODUCTION

1.1 OVERVIEW OF POLYMER MICROCAPSULES AND TRIGGERED RELEASE

Compartmentalization is critical for evolutions of cells and organisms.[1] Membranes and proteins construct the physical boundaries and separate chemicals and nutritions in different organelles. These microscopic compartments allow biochemical reactions and molecular interactions to proceed simultaneously and/or in a programmed sequential fashion, directing mass transport and self-organization into complex hierarchical structures. In synthetic analogues, designing an autonomous self-regulating chemical systems needs equivalent artificial compartments that are able to recognize, translate, and amplify input signals into chemical outputs and reaction cascades. Polymer microcapsules, vesicles and micelles are synthetic compartments with macromolecules as the physical boundary. They are promising components with functional payloads and programmed to release with temporal and spatial control for building autonomous chemical systems. Among these polymeric compartments, microcapsules consist of diverse shell walls and payloads of different chemical and physical properties. The payloads remain dormant inside the microcapsules and are delivered on-demand upon the rupture or transformation of the shell walls to initiate the payload's functions. Microencapsulation improves payload's stability against oxidation and heat, and has found applications in drug delivery,[2,3] cosmetics,[4,5] food & beverage,[6] agrochemicals,[7] and self-healing composite materials.[8]

Gaining temporal control in payload delivery is important for integrating microcapsules and other compartments into autonomous chemical systems. The payload release kinetic profiles depend on the structures and compositions of microcapsules, the properties of the shell wall

polymers, and the solubility of the encapsulated payloads. For example, matrix-based microcapsules (microparticles) with biodegradable polymers are useful in drug delivery to achieve controlled release in a time frame that matches the biological systems (typically days to months). In drug delivery, tri-phasic payload release kinetic profiles are commonly observed (Figure 1.1). This is attributed to different payload delivery mechanisms: burst release caused by the unencapsulated and surface bounded drugs (phase I), controlled release driven by diffusion (phase II), and release induced by shell wall erosion (phase III). The burst release stage is usually uncontrollable and thereby not desired for drug delivery applications. This burst release stage can be shortened by optimizing the encapsulation procedures, formulations, and post-processing methods.[9] Phase II and III of the release kinetic profiles can be tuned by changing molecular weight and crystallinity of the matrix/shell wall polymers, environments of the microcapsule's suspensions, drug-drug or drug-polymer interactions, etc.[10]

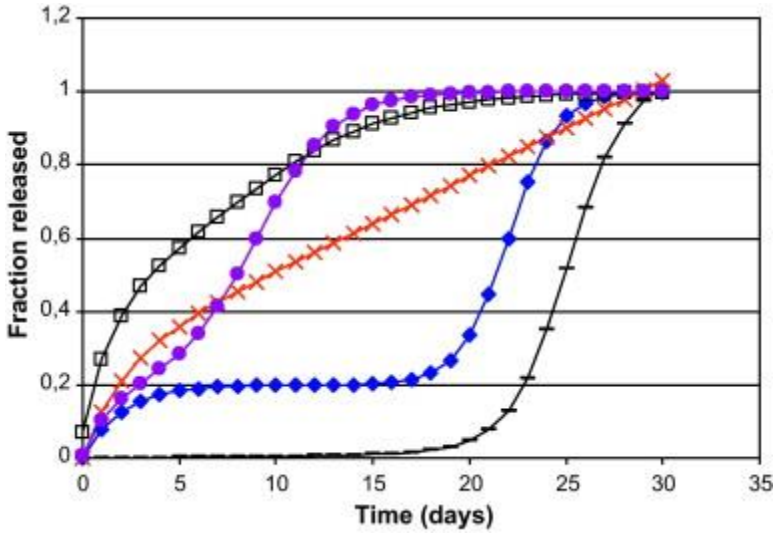

Figure 1.1. Tri-phasic drug release kinetic profiles in poly(lactic-co-glycolic acid)-based drug delivery systems. Phase I, burst release of surface bounded drugs; phase II, diffusion driven drug release; phase III, erosion driven drug release. (Reprinted with permission from reference [10]. Copyright © 2011 Elsevier B. V.)

On the contrary, burst release triggered by a specific stimuli is beneficial for applications such as self-healing materials. The self-healing materials repair material's "wound" *in situ* with minimum external intervention. Sometimes, instantaneous property recovery is required to prevent catastrophic failures. For example, immediate transparency recovery of a broken windshield is useful to protect passengers during a collision. Because the core-shell microcapsules have the potential to release payloads completely in a burst release kinetic profile, the core-shell morphology is desirable for self-healing applications.[3,11]

In addition to releasing the encapsulated payloads from mechanically ruptured microcapsules, environmentally triggered payload release from core-shell microcapsules are attracting increasing interest. Triggered release microcapsules offer temporal and spatial controls of payload delivery. Various chemistry strategies,[12,13] manufacture methodologies,[6,9] and mathematics models[14] have been developed to advance these fields. Precedent literatures have reported microcapsules triggered by various environmental stimuli, including contact and endogenous stimuli, such as pH, ions, redox, and enzymes; remote and exogenous stimuli, such as photo-irradiation, thermal radiation, sonication, microwave, and magnetic energy. The applications of these triggered release microcapsules range from cancer therapy, anticorrosive/antimicrobial coatings, batteries and electronics, to personal care products (Figure 1.2). For example, pH-responsive microcapsules encapsulated with antitumor drugs deliver payloads after internalized by cancer tissues, where the intracellular acidic environments triggered the shell wall disassembly.[15] This allows more spatially accurate and efficient drug delivery. Another example is to incorporate thermo-responsive microcapsules/microspheres for lithium batteries that autonomously shut down once the local temperature increases over the

safety threshold.[16,17] Several studies also reported microcapsules that serve as microreactors for one-pot reaction cascades.[18–20]

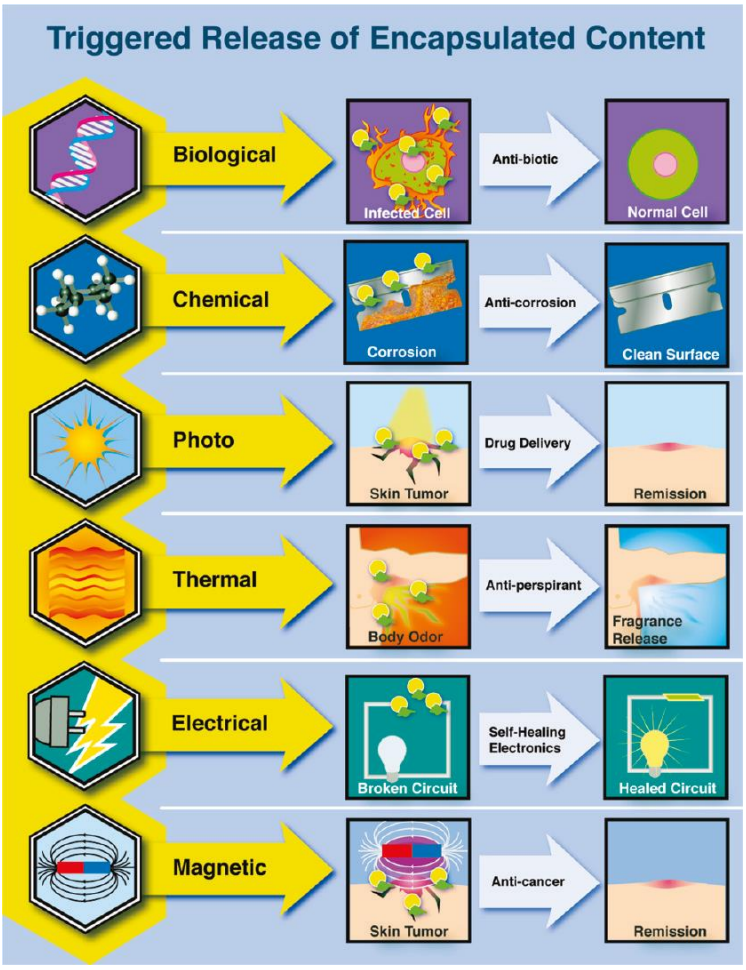

Figure 1.2. Triggered release mechanisms and applications of environmentally triggered microcapsules. (Reprinted with permission from reference [12]. Copyright © 2011 American Chemical Society)

1.2 MICROENCAPSULATION METHODOLOGIES FOR CORE-SHELL MICROCAPSULES

Development of encapsulation methodologies drives the production of advanced microcapsules for various applications. Emerging from our interest to develop synthetic analogues for autonomous chemical systems and self-healing applications, the main focus of this dissertation is the development of core-shell microcapsules with solid polymer shell walls. Considerations for selecting an encapsulation methodology for target payloads include their

chemical properties, phase (liquid, solids, gas), hydrophilicity, solubility and volatility. Four major encapsulation methodologies are shown in Figure 1.3.

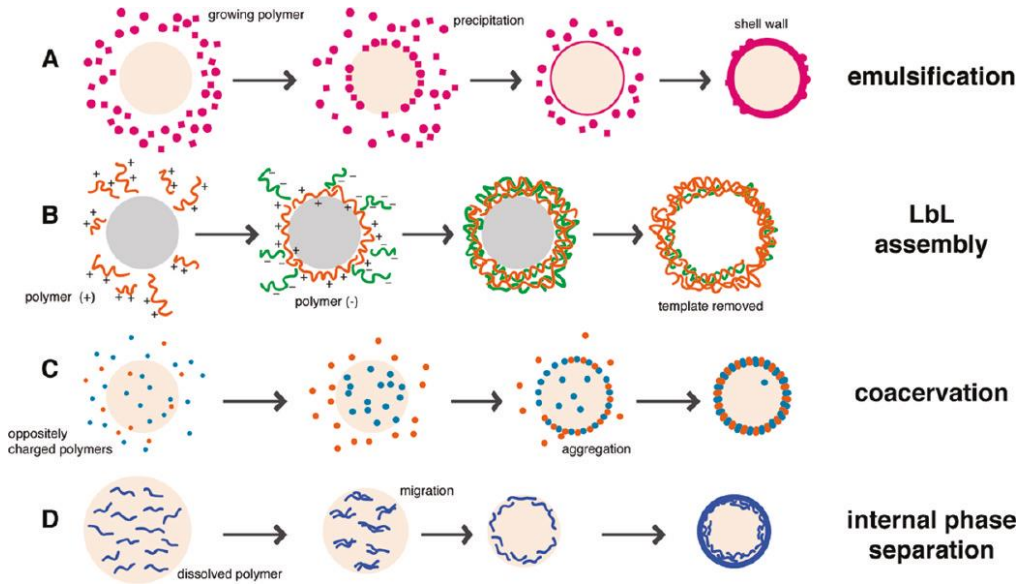

Figure 1.3. Schemes of encapsulation methodologies for producing core-shell microcapsules: (a) interfacial polymerization, (b) layer-by-layer assembly, (c) coacervation, and (d) internal phase separation (also called solvent evaporation).(Reprinted with permission from reference [12] *Copyright © 2011 American Chemical Society)*

1.2.1 Microcapsules Prepared by Interfacial Polymerization

Emulsion based interfacial polymerization is one of the most affordable and versatile encapsulation methods (Figure 1.3a). Typically, oil-in-water (O/W), water-in-oil (W/O) or oil-in-oil (O/O) emulsions are generated by mechanical agitation. A crosslinked polymer network form at the interfaces of the continuous and the dispersed phases dissolved with complementary reactants, separately. Commonly employed chemicals for shell wall formation are amines, isocyanates, alcohols and acid chlorides. The microcapsules prepared by interfacial polymerization have ultrathin and robust shell walls and 90 wt% of the microcapsules are loaded with the payloads. This method is also scalable and versatile to encapsulate different functional

payloads and reactive chemicals, which are of interest to develop self-healing materials. Microcapsules with dicyclopentadiene (DCPD) were demonstrated to recover material's mechanical properties. Charge transfer salts,[21] liquid metal gallium-indium,[22] carbon nanotubes[23] or functionalized carbon nanoparticles[24] were encapsulated for reconstructing electronic conductivity. Color changing microcapsules upon mechanical rupture were developed for damage indication coatings.[25–27] Several strategies have also been developed to reinforce the microcapsule's barrier properties by forming polyurethane/poly(urea-formaldehyde) double layered shell walls in microcapsules.[28] Microcapsules with superior stability were also prepared with a coating of polydopamine.[29]

1.2.2 Microcapsules Prepared by Layer-by-Layer Assembly and Coacervation

The Layer-by-layer (LbL) assembly method produces microcapsules based on electrostatic interactions of charge complementary polyelectrolytes (Figure 1.3b).[15] The polyelectrolytes are deposited onto sphere-shaped templates ($CaCO_3$, polystyrene, etc), which are removed after forming shell walls. Positively and negatively charged polyelectrolytes are deposited alternatively onto the surface of the sphere-shaped templates in a stepwise manner. The advantage of LbL method is the ability to load various core materials after the shell wall formation, because the shell wall is semipermeable. The permeability of the shell walls is also reversible by tuning charge density through environment variations (pH, ions, redox).[30] The main limit in the applications of these microcapsules are their shell wall's mechanical properties. Reinforcement strategies such as doping inorganic nanoparticles in the shell walls promote the stability of these microcapsules against air-drying.[31,32]

Coacervation method produces microcapsules with solid shell walls based on charge complementary polymers (Figure 1.3c). Similar to interfacial polymerization, charge

complementary polymers are dissolved separately in the continuous and the dispersed phases of the emulsions. The electrostatic interactions between the polymers and their chain entanglements are driving forces to form the shell walls.[33]

1.2.3 Microcapsules Prepared by Solvent Evaporation Method

Emulsion-based solvent evaporation method is suitable for systems with readily prepared polymers (Figure 1.3d).[9,34–38] The driving force for shell wall formation in this method is the evaporation of the solvent that precipitates the polymers at the interfaces. This method can be used to prepare both matrix-based microparticles and core-shell microcapsules. This method has been applied in large-scale production of biodegradable polymer microparticles for drug delivery applications.[9,34] The core-shell microcapsules prepared by the solvent evaporation method have good mechanical properties, because of the relatively thick shell walls (~10% relative to the microcapsule's diameters). One limitation of this method is few polymer/payload combinations are available to satisfy the interfacial wetting requirements to form the core-shell morphology. We will elaborate on this matter in Chapter 2, 2.1.

1.2.4 Microcapsules Prepared by Flow-Focusing Microfluidic Devices

Microcapsules prepared from emulsion templates generated by a flow-focusing microfluidic device is a rising research area. The flow-focusing microfluidic devices generate emulsion droplets with precise control of dimensions, structures, and compositions, compared with polydisperse emulsion droplets generated by mechanical agitation. The microfluidics method provides monodisperse microcapsules that serve as model systems for property analysis and structural variations. The Weitz group has made significant contributions in developing functional microcapsules, polymersomes and complex emulsions with flow-focusing microfluidic devices.[39] Microcapsules prepared by water-in-oil-in-water (W/O/W) double

emulsion templates are the most widely applied (Figure 1.4). To form solid shell walls in W/O/W method, typically, the middle fluid oil phase consists of photocurable monomers and photoinitiators, and the middle fluid polymerizes under UV irradiation. Alternatively, shell wall polymers can be dissolved in the middle fluid and the shell wall form after solvent evaporation.

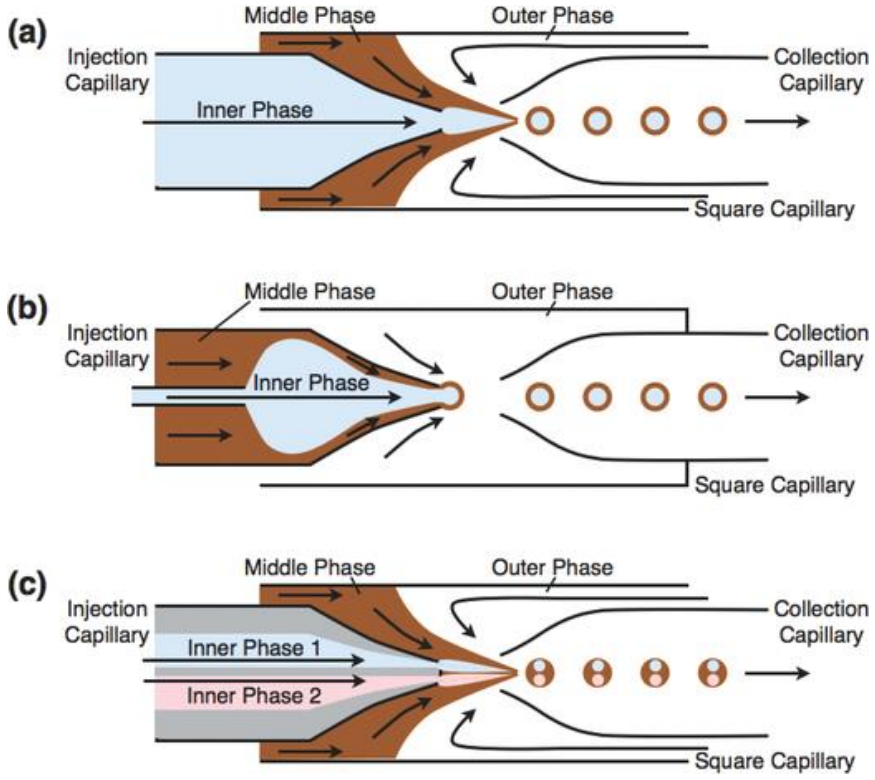

Figure 1.4. Three configurations of flow-focusing microfluidic devices for producing W/O/W double emulsion templates with (a) thick middle phases, (b) ultra-thin middle phases, and (c) multiple inner droplets. (Reprinted with permission from reference [39] *Copyright © 2014 WILEY-VCH)*

Microfluidic devices with various configurations have been developed to produce single, double, and triple emulsions for a variety of applications. Gas-filled microcapsules with robust shell walls were fabricated by W/O/W double emulsion to enhance the signal contrasts in acoustic imaging applications.[40] Development of triple emulsions, hydrocarbon/water/photocurable oil/water, enhanced the retention of volatile hydrocarbon payloads such as fragrance (α-pinene) with a thin layer of water around the hydrocarbon core.[41]

Another triple emulsion system is water/fluorocarbon/photocurable oil/water, where payloads with different polarity (water, ethanol, hexadecane) has been encapsulated successfully.[42] Chu *et al.* also developed multi-level hierarchical complex emulsions *via* a cascade of flow-focusing microfluidic devices.[43] A thermo-responsive polymer, poly(*N*-isopropylacrylamide) (pNIPAM), was selectively formed at the outer layer of the emulsion droplets A temperature variation triggered the collapse of the pNIPAM layer and released the internal droplets.

1.3 STRATEGIES FOR ENVIRONMENTALLY TRIGGERED MICROCAPSULES

To achieve triggered payload release from core-shell microcapsules, chemically modified and engineered shell walls have been designed. Based on whether the environmental stimuli intimately or remotely trigger the shell wall and release the encapsulated payloads, the triggered release strategies are categorized into endogenous triggers (pH, ion, redox, enzyme, etc) and exogenous triggers (irradiation, microwave, sonication, etc).[3]

1.3.1 Endogenous Triggered Release Microcapsules

Acid or base triggered microcapsules are developed based on shell walls with chemical linkers and backbones that either degrade or dissolve in response to pH variations. For example, ketal hydrolysis chemistries have been employed in preparing acid sensitive microcapsules/microparticles with interfacial polymerization.[44] Broaders *et al*. has reported using diethylaminoketal (DEAK) and trimesoyl chloride to form crosslinked shell walls. The microcapsules and degradation products were demonstrated to be biocompatible. *In vitro* experiments showed that these microcapsules were triggered by the acidification of the cells and delivered the encapsulated hydrophobic drugs. Several studies have also reported libraries of ketal linkers with different length and substitute groups. Tunable ketal chemistries have been developed by the Frechet's group to synthesize acid sensitive polyureas and polyurethanes

microparticles.[45] A recent report from Thayumanavan's group has systematically examined the effect of substitute groups of ketals on their degradation kinetics.[46]

Redox-responsive microcapsules are important applications in biomedical applications. Thiol-disulfide redox-responsive groups are one of the most commonly employed. Microcapsules shell wall crosslinked by the disulfide groups are stable outside the cells in an oxidizing environment. When the microcapsules are uptake by the cells, the disulfide groups are reduced into thiol groups in the intracellular reducing environments, unzipping the crosslinking networks and releasing the payloads.[47] Another example is to use redox reactions to control the permeability of the microcapsules. Ma *et al.* reported microcapsules with multi-layer organometallic polyelectrolytes poly(ferrocenysilane) (PFS).[30] When the microcapsules were exposed in $FeCl_3$ (1 mM) solutions, the PFS microcapsules expanded and became permeable to 4.4 kDa dextran molecules. The sensitivity of the microcapsules to oxidants (1 mM $FeCl_3$) was remarkable and was hypothesized due to increasing positive charges upon oxidation that caused repulsion between the charge complementary layers and disrupted the shell wall integrity. Lv *et al.* reported redox-responsive microcapsules with conducting polymers, polypyrrole and polyaniline, as the shell walls. The polyaniline microcapsules collapsed upon reduction and released the encapsulated healing agents.

Ion-responsive microcapsules are less commonly explored in the literature but have many potential variations in designing environmentally triggered microcapsules. In early studies, Okahata *et al*. demonstrated microcapsules with phospholipid bilayer membranes as the shell wall materials. The release of payloads (NaCl) was regulated by phase transition temperature (45 °C from rigid solids to liquid crystals) of the lipid bilayers and/or the cleating of Ca^{2+} with the lipid's phosphoethanolamine groups.[48,49] Chu *et al.* reported microcapsules with porous

membrane consisting of linear grafted poly(N-isopropylacrylamide-co-benzo-18-crown[6]-acrylamide) (poly(NIPAM-*co*-BCAm)). The benzo-18-crown[6]acrylamide (BCAm) moieties are the ion recognition unit. The binding of metal ions (Ba^{2+} or Pb^{2+}) with BCAm shifted the lower critical solution temperature (LCST) of pNIPAM, which isothermally triggered the transition of the membranes into swollen phases, closing the pores of the membranes and slowing down the payload release. Another polymer with benzo-15-crown[5]acrylamide moieties was found to have a squirting payload release mechanism. The binding of K^+ with the crown ether moieties triggered significant shrinking of the microcapsules and squeezed the payloads out.[50]

1.3.2 Exogenous Triggered Release Microcapsules.

Photo-irradiation provides external triggered release mechanisms and are desirable for microcapsules in cosmetics and radiation therapy applications. One strategy for designing light-sensitive microcapsules is to incorporate chromophores such as azobenzene. Azobenzene absorbs energy in both visible (> 400 nm) and UV (300-400 nm) spectrums. Under visible light, azobenzene converts from a *cis* to a *trans* isomer, and under UV light, azobenzene converts from a *trans* to a *cis* isomer.[51] The *cis* azo moieties form aggregates and rupture the shell walls to release payloads under UV irradiation.[52]

Another strategy is based on the optothermal triggered release mechanism. Composite microcapsules are prepared with shell walls containing inorganic nanoparticles. The nanoparticles absorb irradiation energy and increase local temperatures of the shell walls, thus either rupturing the shell walls[53] or triggering phase transitions of the shell walls to deliver the payloads.[54] Yavuz *et al.* reported gold nanocages with hollow interiors and porous wall structures. The nanocages were coated with thermo-responsive pNIPAM. After irradiation by a

laser beam, the surface temperature increased and triggered the transition of pNIPAM from extended conformations to collapsed conformations. The collapsed polymer released the encapsulated cargos on demand.

Similarly, microcapsules doped with $MnCO_3$,[55] TiO_2 nanoparticles,[56] or carbon nanotubes[53] have also been reported to deliver payloads under photo-irradiation or microwave irradiation.[55] Meanwhile, hybrid microcapsules with Fe_3O_4 is a useful strategy for magnetic-responsive microcapsules.[57] The payload release can be controlled spatially by a magnetic field and temporally by a thermal-induced self-rupturing mechanism.

1.4 TRANSIENT POLYMERS AS SHELL WALL MATERIALS FOR TRIGGERED RELEASE MICROCAPSULES

Transient polymers are emerging polymer materials that can autonomously transform from macromolecules to small molecules in an amplified and complete fashion. Different from traditional degradable polymers, which need n-1 cleavages for complete depolymerization, transient polymers need one single cleavage at the chain end or at a random site, followed by continuous depolymerization from the cleavage to unzip the backbones autonomously. In addition to the feature of controlled and clean depolymerization, transient polymers are also beneficial for chemical and signal amplifications because one cleavage results in multiple copies of small molecules. In the last decade, this class of polymers has been applied to sensors/point-of-care assays,[58,59] lithography,[60] microcapsules,[61] adhesives,[62] and transient electronics packaging.[63,64]

To achieve continuous depolymerization upon cleavage, previously reported polymers are designed based on two mechanisms. One approach is to initiate sequential intramolecular elimination and/or cyclization reactions once cleaved and these polymers depolymerize in a self-

immolative manner. Alternatively, kinetically trapped low ceiling temperature (T_c) polymers are synthesized below their T_c. Upon cleavage, when $T > T_c$, these polymers revert back to monomers driven by thermodynamic equilibrium. Several types of polymers have been synthesized based on these two mechanisms, including polyphthalaldehyde (linear and cyclic), poly(ethyl glyoxylate), poly(benzyl ethers), and polycarbamates. Representative backbones and corresponding mechanisms are summarized in Figure 1.5.[65]

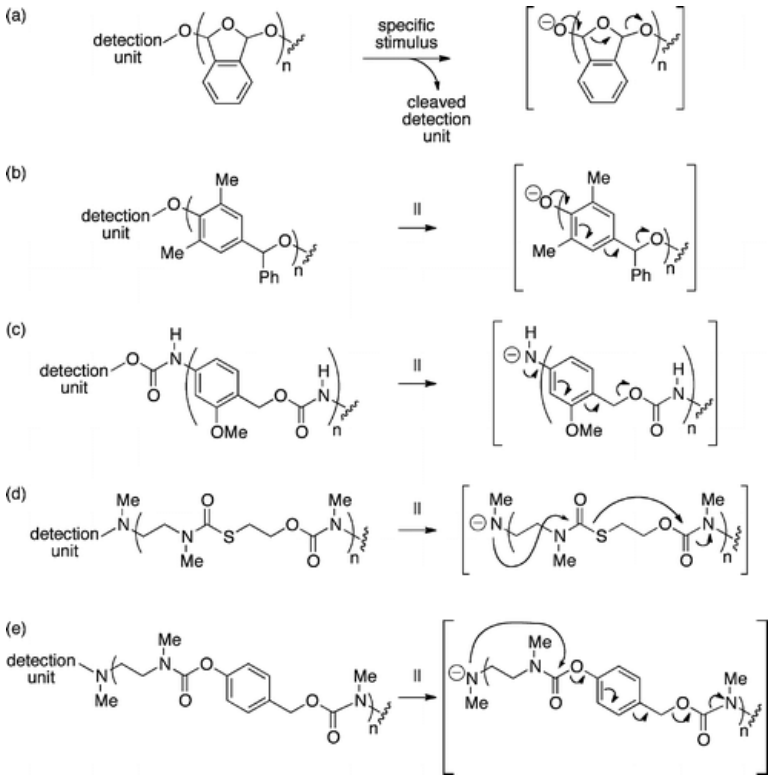

Figure 1.5. Representative transient polymer backbones and their depolymerization mechanisms. (Reprinted with permission from reference [65] *Copyright © 2014 American Chemical Society)*

1.4.1 Self-Immolative Transient Polymers

Sagi *et al.* reported the first self-immolative polymer (SIP) prepared from a phenyl carbamate (Figure 1.5c).[66] Removing the end capping groups triggered sequential 1,6-elimination and decarboxylation reactions, resulting in CO_2 and azaquinones as the

depolymerization products. Furthermore, quinones reacted with water molecules in the solvent and generated 4-aminobenzylalcohol as the final depolymerization products. A signal amplification system was also designed based on this SIP using a precursor of fluorescent amine. The polymers have significantly reduced fluorescence because the amines were masked as carbamates. Upon end group cleavage, the self-immolative reactions produced the fluorescent amines, thus amplifying the signals. Modified polymer backbones based on this SIP also served as prepolymers to form crosslinked shell walls for triggered release microcapsules.[67] Depolymerization kinetics was modulated by modifying backbones with cyclizing spacers (Figure 1.5d-e).[68–71] Recently, the Shabat group introduced chemiluminescence features in self-immolative polycarbamates. The depolymerization generated phenolate-dioxetane, which decomposed through a chemiexcitation process with amplified signals.[72–74] This strategy further advances the applications of SIP in (bio)imaging, molecular sensors, and light-emitting materials.

The Phillips group has advanced the synthesis and applications of transient polymers. Poly(benzyl ethers) is one of the newest transient polymers, which depolymerize through sequential quinone methide elimination (Figure 1.5b).[75] In addition to solution phase depolymerization, solid phase depolymerization of poly(benzyl ethers) was demonstrated with the detection units as the pendent groups, which increased the number of accessible detection units (often considered as the rate-limiting step) at the interfaces of the bulk polymers and solution or air.[76] This strategy provides opportunities to apply transient polymers as bulk materials.

1.4.2 Low-Ceiling-Temperature Transient Polymers

Polyphthalaldehyde (PPA) ($T_c \approx$ -40 °C) [77,78] in Figure 1.5a belongs to low-ceiling-temperature polymers. Ceiling temperature is where depolymerization and polymerization reach equilibrium.[79] Above ceiling temperature, the polymers become thermodynamically unstable and tend to revert back to small molecules. Kinetically stabilized PPA can be synthesized by anionic polymerization and capping the chain termini. The end capping group can be stimuli-responsive units. The removal of end groups trigger the cascade depolymerization.[80] To incorporate functionality, copolymers of *o*-phthalaldehyde (*o*-PA) with substituted benzaldehydes were synthesized by anionic polymerization. Another strategy for obtaining kinetically stabilized PPA is cationic polymerization, which has been recently discovered that a cyclic polymer, cyclic poly(phthaladehyde) (cPPA), is the sole product.[81] The cationic polymerization has more tolerance for monomer (*o*-PA) impurities that provides a facile approach to synthesize cPPA of molecular weight 10-200 kDa with satisfactory yields.

Another class of low-ceiling-temperature polymer is polyglyoxylate. This class of polymers is attractive because the depolymerization products, glyoxylate, is demonstrated to be nontoxic in invertebrate and plant ecotoxicity models, and the ceiling temperature of poly(ethyl glyoxylate) (PEtG, T_c = 37 °C) is of interest in biological applications.[82] Fan *et al.* have systematically designed and investigated polyglyoxylates with different ester substitutes[83] and stimuli-responsive end-capping groups with chloroformate derivatives.[83,84] Highly reactive chloroformates allow the end-capping procedures to complete *in situ* at -20 °C (lower than the T_c of PEtG). Redox-responsive, UV-responsive, acid-responsive, and multi-responsive end-capping groups were prepared to incorporate multiple triggered depolymerization features in PEtG. A triblock amphiphilic copolymer of PEtG and polyethylene glycol (PEG), PEG-PEtG-PEG, was

found to form micellar nanostructures through self-assembly and released payload in response to UV irradiation. Cyclopolymerization of PEtG and PPA was also demonstrated by Kaitz *et al. via* cationic polymerization.[85] Copolymers with tunable glass transition temperatures and thermal degradation temperatures were obtained, allowing applications that require tunable mechanical properties and thermal stabilities.

1.5 REFERENCES

(1) Lehn, J. M. Toward Self-Organization and Complex Matter. *Science* **2002**, *295*, 2400–2403.

(2) Ramazani, F.; Chen, W.; Van Nostrum, C. F.; Storm, G.; Kiessling, F.; Lammers, T.; Hennink, W. E.; Kok, R. J. Strategies for Encapsulation of Small Hydrophilic and Amphiphilic Drugs in PLGA Microspheres: State-of-the-Art and Challenges. *Int. J. Pharm.* **2016**, *499*, 358–367.

(3) Kamaly, N.; Yameen, B.; Wu, J.; Farokhzad, O. C. Degradable Controlled-Release Polymers and Polymeric Nanoparticles: Mechanisms of Controlling Drug Release. *Chem. Rev.* **2016**, *116*, 2602–2663.

(4) Ammala, A. Biodegradable Polymers as Encapsulation Materials for Cosmetics and Personal Care Markets. *Int. J. Cosmet. Sci.* **2013**, *35*, 113–124.

(5) Lei, Y.; Xu, L.; Joyee, C. Polyurea Capsules Prepared with Aliphatic Isocyanates and Amines. U.S. Patent 13,969,038, Dec 19, 2013.

(6) Bakry, A. M.; Abbas, S.; Ali, B.; Majeed, H.; Abouelwafa, M. Y.; Mousa, A.; Liang, L. Microencapsulation of Oils: A Comprehensive Review of Benefits, Techniques, and Applications. *Compr. Rev. Food Sci. Food Saf.* **2016**, *15*, 143–182.

(7) Burakowska-Meise, E.; Bem, V.; Joanna Mecfel-Marczewski; Klimov, E.; Kolb, K.; Matthias Bratz; BOWE, S. J.; Repage, R.; Frihauf, J. Agrochemical Microcapsules with a Shell of Polyvinylalcohol and Polyoxazoline. Eur. Pat. Appl. 069455, Aug 18, 2015.

(8) White, S. R.; Blaiszik, B. J.; Kramer, S. L. B.; Olugebefola, S. C.; Moore, J. S.; Sottos, N. R. Self-Healing Polymers and Composites. *Am. Sci.* **2011**, *99*, 392–399.

(9) Li, M.; Rouaud, O.; Poncelet, D. Microencapsulation by Solvent Evaporation: State of the Art for Process Engineering Approaches. *Int. J. Pharm.* **2008**, *363*, 26–39.

(10) Fredenberg, S.; Wahlgren, M.; Reslow, M.; Axelsson, A. The Mechanisms of Drug Release in Poly(lactic-Co-Glycolic Acid)-Based Drug Delivery Systems - A Review. *Int. J. Pharm.* **2011**, *415*, 34–52.

(11) Wong, A. D.; DeWit, M. A.; Gillies, E. R. Amplified Release through the Stimulus Triggered Degradation of Self-Immolative Oligomers, Dendrimers, and Linear Polymers. *Adv. Drug. Deliv. Rev.* **2012**, *64*, 1031–1045.

(12) Esser-Kahn, A. P.; Odom, S. A.; Sottos, N. R.; White, S. R.; Moore, J. S. Triggered Release from Polymer Capsules. *Macromolecules* **2011**, *44*, 5539–5553.

(13) Wang, H. C.; Zhang, Y.; Possanza, C. M.; Zimmerman, S. C.; Cheng, J.; Moore, J. S.; Harris, K.; Katz, J. S. Trigger Chemistries for Better Industrial Formulations. *ACS Appl. Mater. Interfaces* **2015**, *7*, 6369–6382.

(14) Siepmann, J.; Siepmann, F. Mathematical Modeling of Drug Delivery. *Int. J. Pharm.*

2008, *364*, 328–343.

(15) Sato, K.; Yoshida, K.; Takahashi, S.; Anzai, J. ichi. PH- and Sugar-Sensitive Layer-by-Layer Films and Microcapsules for Drug Delivery. *Adv. Drug Deliv. Rev.* **2011**, *63*, 809–821.

(16) Baginska, M.; Blaiszik, B. J.; Merriman, R. J.; Sottos, N. R.; Moore, J. S.; White, S. R. Autonomic Shutdown of Lithium-Ion Batteries Using Thermoresponsive Microspheres. *Adv. Energy Mater.* **2012**, *2*, 583–590.

(17) Baginska, M.; Blaiszik, B. J.; Odom, S. A.; Caruso, M. M.; Sottos, N. R.; White, S. R. Experimental Mechanics on Emerging Energy Systems and Materials. *Proc. 2010 Annu. Conf. Exp. Appl. Mech.* **2011**, *5*, 17–23.

(18) Longstreet, A. R.; McQuade, D. T. Organic Reaction Systems: Using Microcapsules and Microreactors to Perform Chemical Synthesis. *Acc. Chem. Res.* **2013**, *46*, 327–338.

(19) Yang, H.; Fu, L.; Wei, L.; Liang, J.; Binks, B. P. Compartmentalization of Incompatible Reagents within Pickering Emulsion Droplets for One-Pot Cascade Reactions. *J. Am. Chem. Soc.* **2015**, *137*, 1362–1371.

(20) Zhang, M.; Ettelaie, R.; Yan, T.; Zhang, S.; Cheng, F.; Binks, B. P.; Yang, H. Ionic Liquid Droplet Micro-Reactor for Catalysis Reactions Not at Equilibrium. *J. Am. Chem. Soc.* **2017**, *139*, 17387–17396.

(21) Vrbka, L.; Vondrásek, J.; Jagoda-Cwiklik, B.; Vácha, R.; Jungwirth, P. Quantification and Rationalization of the Higher Affinity of Sodium over Potassium to Protein Surfaces. *Proc. Natl. Acad. Sci.* **2006**, *103*, 15440–15444.

(22) Blaiszik, B. J.; Kramer, S. L. B.; Grady, M. E.; McIlroy, D. A.; Moore, J. S.; Sottos, N. R.; White, S. R. Autonomic Restoration of Electrical Conductivity. *Adv. Mater.* **2012**, *24*, 398–401.

(23) Odom, S. A.; Tyler, T. P.; Caruso, M. M.; Ritchey, J. A.; Schulmerich, M. V; Robinson, S. J.; Bhargava, R.; Sottos, N. R.; White, S. R.; Hersam, M. C.; Moore, J. S. Autonomic Restoration of Electrical Conductivity Using Polymer-Stabilized Carbon Nanotube and Graphene Microcapsules. *Appl. Phys. Lett.* **2012**, *101*, 043106–043111.

(24) Kang, S.; Jones, A. R.; Moore, J. S.; White, S. R.; Sottos, N. R. Microencapsulated Carbon Black Suspensions for Restoration of Electrical Conductivity. *Adv. Funct. Mater.* **2014**, *24*, 2947–2956.

(25) Li, W.; Matthews, C. C.; Yang, K.; Odarczenko, M. T.; White, S. R.; Sottos, N. R. Autonomous Indication of Mechanical Damage in Polymeric Coatings. *Adv. Mater.* **2016**, *28*, 2189–2194.

(26) Robb, M. J.; Li, W.; Gergely, R. C. R.; Matthews, C. C.; White, S. R.; Sottos, N. R.; Moore, J. S. A Robust Damage-Reporting Strategy for Polymeric Materials Enabled by Aggregation-Induced Emission. *ACS Cent. Sci.* **2016**, *2*, 598–603.

(27) Odom, S. A.; Jackson, A. C.; Prokup, A. M.; Chayanupatkul, S.; Sottos, N. R.; White, S. R.; Moore, J. S. Visual Indication of Mechanical Damage Using Core-Shell Microcapsules. *ACS Appl. Mater. Interfaces* **2011**, *3*, 4547–4551.

(28) Zhang, L.; Cai, L. H.; Lienemann, P. S.; Rossow, T.; Polenz, I.; Vallmajo-Martin, Q.; Ehrbar, M.; Na, H.; Mooney, D. J.; Weitz, D. A. One-Step Microfluidic Fabrication of Polyelectrolyte Microcapsules in Aqueous Conditions for Protein Release. *Angew. Chemie - Int. Ed.* **2016**, *55*, 13470–13474.

(29) Kang, S.; Baginska, M.; White, S. R.; Sottos, N. R. Core-Shell Polymeric Microcapsules with Superior Thermal and Solvent Stability. *ACS Appl. Mater. Interfaces* **2015**, *7*, 10952–10956.

(30) Ma, Y.; Dong, W.-F.; Hempenius, M. a.; Möhwald, H.; Vancso, G. J. Redox-Controlled Molecular Permeability of Composite-Wall Microcapsules. *Nat. Mater.* **2006**, *5*, 724–729.

(31) Shchukln, D. G.; Ustinovich, E. A.; Sukhorukov, G. B.; Möhwald, H.; Sviridov, D. V. Metallized Polyelectrolyte Microcapsules. *Adv. Mater.* **2005**, *17*, 468–472.

(32) Cui, J.; Fan, D.; Hao, J. Magnetic {Mo72Fe30}-Embedded Hybrid Nanocapsules. *J. Colloid Interface Sci.* **2009**, *330*, 488–492.

(33) Arshady, R. Microspheres and Microcapsules, a Survey of Manufacturing Techniques. Part II : Coacervation. *Polym. Eng. Sci.* **1990**, *30*, 905–914.

(34) Li, W.-I.; Anderson, K. W.; Deluca, P. P. Kinetic and Thermodynamic Modeling of the Formation of Polymeric Microspheres Using Solvent Extraction/evaporation Method. *J. Control. Release* **1995**, *37*, 187–198.

(35) Pekarek, K. J.; Jacob, J. S.; Mathiowitz, E. Double-Walled Polymer Microspheres for Controlled Drug Release. *Nature* **1994**, *367*, 258–260.

(36) Dowding, P. J.; Atkin, R.; Vincent, B.; Bouillot, P. Oil Core-Polymer Shell Microcapsules Prepared by Internal Phase Separation from Emulsion Droplets. I. Characterization and Release Rates for Microcapsules with Polystyrene Shells. *Langmuir* **2004**, *20*, 11374–11379.

(37) Fundueanu, G.; Constantin, M.; Esposito, E.; Cortesi, R.; Nastruzzi, C.; Menegatti, E. Cellulose Acetate Butyrate Microcapsules Containing Dextran Ion-Exchange Resins as Self-Propelled Drug Release System. *Biomaterials* **2005**, *26*, 4337–4347.

(38) Zhao, Y.; Fickert, J.; Landfester, K.; Crespy, D. Encapsulation of Self-Healing Agents in Polymer Nanocapsules. *Small* **2012**, *8*, 2954–2958.

(39) Datta, S. S.; Abbaspourrad, A.; Amstad, E.; Fan, J.; Kim, S. H.; Romanowsky, M.; Shum, H. C.; Sun, B.; Utada, A. S.; Windbergs, M.; Zhou, S.; Weitz, D. A. 25th Anniversary Article: Double Emulsion Templated Solid Microcapsules: Mechanics and Controlled Release. *Adv. Mater.* **2014**, *26*, 2205–2218.

(40) Abbaspourrad, A.; Duncanson, W. J.; Lebedeva, N.; Kim, S. H.; Zhushma, A. P.; Datta, S.

S.; Dayton, P. A.; Sheiko, S. S.; Rubinstein, M.; Weitz, D. A. Microfluidic Fabrication of Stable Gas-Filled Microcapsules for Acoustic Contrast Enhancement. *Langmuir* **2013**, *29*, 12352–12357.

(41) Choi, C. H.; Lee, H.; Abbaspourrad, A.; Kim, J. H.; Fan, J.; Caggioni, M.; Wesner, C.; Zhu, T.; Weitz, D. A. Triple Emulsion Drops with An Ultrathin Water Layer: High Encapsulation Efficiency and Enhanced Cargo Retention in Microcapsules. *Adv. Mater.* **2016**, *28*, 3340–3344.

(42) Lee, H.; Choi, C. H.; Abbaspourrad, A.; Wesner, C.; Caggioni, M.; Zhu, T.; Nawar, S.; Weitz, D. A. Fluorocarbon Oil Reinforced Triple Emulsion Drops. *Adv. Mater.* **2016**, *28*, 8425–8430.

(43) Chu, L. Y.; Utada, A. S.; Shah, R. K.; Kim, J. W.; Weitz, D. A. Controllable Monodisperse Multiple Emulsions. *Angew. Chemie - Int. Ed.* **2007**, *46*, 8970–8974.

(44) Broaders, K. E.; Pastine, S. J.; Grandhe, S.; Frechet, J. M. Acid-Degradable Solid-Walled Microcapsules for pH-Responsive Burst-Release Drug Delivery. *Chem. Commun.* **2011**, *47*, 665–667.

(45) Paramonov, S. E.; Bachelder, E. M.; Beaudette, T. T.; Standley, S. M.; Lee, C. C.; Dashe, J.; Fréchet, J. M. J. Fully Acid-Degradable Biocompatible Polyacetal Microparticles for Drug Delivery. *Bioconjug. Chem.* **2008**, *19*, 911–919.

(46) Liu, B.; Thayumanavan, S. Substituent Effects on the pH Sensitivity of Acetals and Ketals and Their Correlation with Encapsulation Stability in Polymeric Nanogels. *J. Am. Chem. Soc.* **2017**, *139*, 2306–2317.

(47) Johnston, A. P.; Such, G. K.; Caruso, F. Triggering Release of Encapsulated Cargo. *Angew. Chemie - Int. Ed.* **2010**, *49*, 2664–2666.

(48) Okahata, Y.; Lim, H. J. Functional Capsule Membranes. Signal-Receptive Permeability Control of NaCl from a Large Nylon Capsule Coated with Phospholipid Bilayers. *J. Am. Chem. Soc.* **1984**, *106*, 4696–4700.

(49) Okahata, Y. Lipid Bilayer-Corked Capsule Membranes. Reversible, Signal-Receptive Permeation Control. *Acc. Chem. Res.* **1986**, *19*, 57–63.

(50) Liu, Z.; Liu, L.; Ju, X.-J.; Xie, R.; Zhang, B.; Chu, L.-Y. K+-Recognition Capsules with Squirting Release Mechanisms. *Chem. Commun.* **2011**, *47*, 12283–12285.

(51) Hartley, G. S. The Cis-Form of Azobenzene. *Nature* **1937**, *140*, 281–281.

(52) Yi, Q.; Sukhorukov, G. B. UV-Induced Disruption of Microcapsules with Azobenzene Groups. *Soft Matter* **2014**, *10*, 1384–1391.

(53) Pastine, S. J.; Okawa, D.; Zettl, A.; Frechet, J. M. J. Chemicals On Demand with Phototriggerable Microcapsules. *J. Am. Chem. Soc.* **2009**, *131*, 13586–13587.

(54) Yavuz, M. S.; Cheng, Y.; Chen, J.; Cobley, C. M.; Zhang, Q.; Rycenga, M.; Xie, J.; Kim,

C.; Andrea G. Schwartz, L. V. W.; Xia, Y. Gold Nanocages Covered by Smart Polymers for Controlled Release with near-Infrared Light. *Nat. Mater.* **2009**, *8*, 935–939.

(55) Gorin, D. A.; Shchukin, D. G.; Mikhailov, A. I.; Köhler, K.; Sergeev, S. A.; Portnov, S. A.; Taranov, I. V.; Kislov, V. V.; Sukhorukov, G. B. Effect of Microwave Radiation on Polymer Microcapsules Containing Inorganic Nanoparticles. *Tech. Phys. Lett.* **2006**, *32*, 70–72.

(56) Wang, Y.; Caruso, F. Template Synthesis of Stimuli-Responsive Nanoporous Polymer-Based Spheres via Sequential Assembly. *Chem. Mater.* **2006**, *18*, 4089–4100.

(57) Du, Q.; Ma, T.; Fu, C.; Liu, T.; Huang, Z.; Ren, J.; Shao, H.; Xu, K.; Tang, F.; Meng, X. Encapsulating Ionic Liquid and Fe3O4 Nanoparticles in Gelatin Microcapsules as Microwave Susceptible Agent for MR Imaging-Guided Tumor Thermotherapy. *ACS Appl. Mater. Interfaces* **2015**, *7*, 13612–13619.

(58) Lewis, G. G.; Robbins, J. S.; Phillips, S. T. A Prototype Point-of-Use Assay for Measuring Heavy Metal Contamination in Water Using Time as a Quantitative Readout. *Chem. Commun.* **2014**, *50*, 5352–5354.

(59) Mohapatra, H.; Phillips, S. T. Using Smell to Triage Samples in Point-of-Care Assays. *Angew. Chemie - Int. Ed.* **2012**, *51*, 11145–11148.

(60) Coulembier, O.; Knoll, A.; Pires, D.; Gotsmann, B.; Duerig, U.; Frommer, J.; Miller, R. D.; Dubois, P.; Hedrick, J. L. Probe-Based Nanolithography: Self-Amplified Depolymerization Media for Dry Lithography. *Macromolecules* **2010**, *43*, 572–574.

(61) DiLauro, A. M.; Abbaspourrad, A.; Weitz, D. A.; Phillips, S. T. Stimuli-Responsive Core-Shell Microcapsules with Tunable Rates of Release by Using a Depolymerizable Poly(phthalaldehyde) Membrane. *Macromolecules* **2013**, *46*, 3309–3313.

(62) Kim, H.; Mohapatra, H.; Phillips, S. T. Rapid, On-Command Debonding of Stimuli-Responsive Cross-Linked Adhesives by Continuous, Sequential Quinone Methide Elimination Reactions. *Angew. Chemie - Int. Ed.* **2015**, *54*, 13063–13067.

(63) Park, C. W.; Kang, S. K.; Hernandez, H. L.; Kaitz, J. A.; Wie, D. S.; Shin, J.; Lee, O. P.; Sottos, N. R.; Moore, J. S.; Rogers, J. A.; White, S. R. Thermally Triggered Degradation of Transient Electronic Devices. *Adv. Mater.* **2015**, *27*, 3783–3788.

(64) Lopez Hernandez, H.; Kang, S. K.; Lee, O. P.; Hwang, S. W.; Kaitz, J. A.; Inci, B.; Park, C. W.; Chung, S. J.; Sottos, N. R.; Moore, J. S.; Rogers, J. A.; White, S. R.; Hernandez, H. L.; Kang, S. K.; Lee, O. P.; Hwang, S. W.; Kaitz, J. A.; Inci, B.; Park, C. W.; Chung, S. J.; Sottos, N. R.; Moore, J. S.; Rogers, J. A.; White, S. R. Triggered Transience of Metastable Poly(phthalaldehyde) for Transient Electronics. *Adv. Mater.* **2014**, *26*, 7637–7642.

(65) Phillips, S. T.; Dilauro, A. M. Continuous Head-to-Tail Depolymerization: An Emerging Concept for Imparting Amplified Responses to Stimuli-Responsive Materials. *ACS Macro Lett.* **2014**, *3*, 298–304.

(66) Sagi, A.; Weinstain, R.; Karton, N.; Shabat, D. Self-Immolative Polymers. *J. Am. Chem.*

Soc. **2008**, *130*, 5434–5435.

(67) Esser-Kahn, A. P.; Sottos, N. R.; White, S. R.; Moore, J. S. Programmable Microcapsules from Self-Immolative Polymers. *J. Am. Chem. Soc.* **2010**, *132*, 10266–10268.

(68) Dewit, M. A.; Gillies, E. R. A Cascade Biodegradable Polymer Based on Alternating Cyclization and Elimination Reactions. *J. Am. Chem. Soc.* **2009**, *131*, 18327–18334.

(69) Chen, E. K. Y.; McBride, R. A.; Gillies, E. R. Self-Immolative Polymers Containing Rapidly Cyclizing Spacers: Toward Rapid Depolymerization Rates. *Macromolecules* **2012**, *45*, 7364–7374.

(70) Dewit, M. A.; Beaton, A.; Gillies, E. R. A Reduction Sensitive Cascade Biodegradable Linear Polymer. *J. Polym. Sci., Part A Polym. Chem.* **2010**, *48*, 3977–3985.

(71) McBride, R. A.; Gillies, E. R. Kinetics of Self-Immolative Degradation in a Linear Polymeric System: Demonstrating the Effect of Chain Length. *Macromolecules* **2013**, *46*, 5157–5166.

(72) Green, O.; Gnaim, S.; Blau, R.; Eldar-Boock, A.; Satchi-Fainaro, R.; Shabat, D. Near-Infrared Dioxetane Luminophores with Direct Chemiluminescence Emission Mode. *J. Am. Chem. Soc.* **2017**, *139*, 13243–13248.

(73) Shabat, D.; Hananya, N. A Glowing Trajectory between Bio- and Chemi-Luminescence: From Luciferin-Based Probes to Triggerable Dioxetanes. *Angew. Chemie - Int. Ed.* **2017**, *56*, 2–12.

(74) Gnaim, S.; Shabat, D. Self-Immolative Chemiluminescence Polymers: Innate Assimilation of Chemiexcitation in a Domino-like Depolymerization. *J. Am. Chem. Soc.* **2017**, *139*, 10002–10008.

(75) Olah, M. G.; Robbins, J. S.; Baker, M. S.; Phillips, S. T. End-Capped Poly(benzyl Ethers): Acid and Base Stable Polymers That Depolymerize Rapidly from Head-to-Tail in Response to Specific Applied Signals. *Macromolecules* **2013**, *46*, 5924–5928.

(76) Yeung, K.; Kim, H.; Mohapatra, H.; Phillips, S. T. Surface-Accessible Detection Units in Self-Immolative Polymers Enable Translation of Selective Molecular Detection Events into Amplified Responses in Macroscopic, Solid-State Plastics. *J. Am. Chem. Soc.* **2015**, *137*, 5324–5327.

(77) Aso, C.; Tagami, S. Polymerization of Aromatic Aldehydes. III. The Cyclopolymerization of Phthalaldehyde and the Structure of the Polymer. *Macromolecules* **1969**, *3*, 414–419.

(78) Aso, C.; Tagami, S.; Kunitake, T. Polymerization of Aromatic Aldehydes. II. Cationic Cyclopolymerization of Phthalaldehyde. *J. Polym. Sci., Part A Polym. Chem.* **1969**, *7*, 497–511.

(79) Dainton, F. S.; Ivin, K. J. Reversibility of the Propagation Reaction in Polymerization Processes and Its Manifestation in the Phenomenon of a "Ceiling Temperature." *Nature* **1948**, *162*, 705–707.

(80) DiLauro, A. M.; Robbins, J. S.; Phillips, S. T. Reproducible and Scalable Synthesis of End-Cap-Functionalized Depolymerizable Poly(phthalaldehydes). *Macromolecules* **2013**, *46*, 2963–2968.

(81) Kaitz, J. A.; Diesendruck, C. E.; Moore, J. S. End Group Characterization of Poly(phthalaldehyde): Surprising Discovery of a Reversible, Cationic Macrocyclization Mechanism. *J. Am. Chem. Soc.* **2013**, *135*, 12755–12761.

(82) Belloncle, B.; Burel, F.; Oulyadi, H.; Bunel, C. Study of the in Vitro Degradation of Poly(ethyl Glyoxylate). *Polym. Degrad. Stab.* **2008**, *93*, 1151–1157.

(83) Fan, B.; Trant, J. F.; Wong, A. D.; Gillies, E. R. Polyglyoxylates: A Versatile Class of Triggerable Self-Immolative Polymers from Readily Accessible Monomers. *J. Am. Chem. Soc.* **2014**, *136*, 10116–10123.

(84) Fan, B.; Trant, J. F.; Gillies, E. R. End-Capping Strategies for Triggering End-to-End Depolymerization of Polyglyoxylates. *Macromolecules* **2016**, *49*, 9309–9319.

(85) Kaitz, J. A.; Moore, J. S. Copolymerization of O -Phthalaldehyde and Ethyl Glyoxylate: Cyclic Macromolecules with Alternating Sequence and Tunable Thermal Properties. *Macromolecules* **2014**, *47*, 5509–5513.

CHAPTER 2 : LOW-CEILING-TEMPERATURE POLYMER MICROCAPSULES WITH HYDROPHOBIC PAYLOADS *VIA* RAPID SOLVENT EVAPORATION

2.1 INTRODUCTION

Microcapsule-based self-healing composite materials have been used to restore mechanical, optical, and electrical properties to damaged materials.[1–7] Mechanical damage triggers the release of microcapsule's payloads into the damage zone, initiating the healing process. The release of payloads on-demand via non-mechanical triggering events remains an active area of development in self-healing materials.[8–10] In Chapter 1, we discussed a promising approach for developing stimuli-responsive microcapsules with a kinetically stabilized low-ceiling-temperature polymer. This class of polymers undergoes cascade depolymerization when end-capping groups are removed and/or the polymer backbones are cleaved by environmental triggers. The polymers rapidly lose mechanical integrity once triggered and provide a convenient means for the on-demand delivery of payloads. Choices for the low-ceiling-temperature polymers are plentiful and include polyphthalaldehydes,[11–13]polyglyoxylates,[13,14] and poly(olefin sulfones).[15–18] However, using these low-ceiling-temperature polymers as the microcapsule's shell walls is often challenging, due to strict requirements on the compatibility of the shell walls and payload materials, while maintaining shell wall stability under encapsulation conditions.

In previous studies, fabrication of microcapsules using low-ceiling-temperature polymers has relied on a water-in-oil-in-water (W/O/W) double emulsion template generated using a flow-focusing microfluidic device. Fluoride-responsive microcapsules with silyl ether-capped linear poly(phthalaldehyde) as the shell wall were fabricated using this approach.[19] Acid-triggered

microcapsules have also been demonstrated using poly(o-(α-methyl)vinylbenzaldehyde) as the shell wall.[20] Beyond these few examples, an alternative, scalable method for the encapsulation of hydrophobic payloads in low-ceiling-temperature polymers is an important target for on-demand, environmentally triggered microcapsule release.

Solvent evaporation is a promising route to fabricate polymer microcapsules with hydrophobic payloads for controlled release.[21–31] Typically, an oil-in-water (O/W) single emulsion template is generated by agitation, followed by solvent evaporation to form microcapsules. The oil phase is a ternary system, containing a polymer, a volatile solvent (*vs*) and a non-volatile non-solvent (*nvns*). The polymer is soluble in the *vs* and immiscible with the *nvns*. Before emulsification, the mixing ratios of the three components are adjusted to form a homogeneous solution. After emulsification, the *vs* is removed by evaporation, leaving the polymer as the shell wall and the *nvns* as the payload. As predicted by canonical spreading coefficient theory,[32] a core-shell microcapsule morphology is thermodynamically favored only when the interfacial tensions (γ) between polymer (p), core (o) and surfactant (w) satisfy relations 2.1-2.3:

$$\gamma_{wp} - (\gamma_{ow} + \gamma_{op}) < 0, \qquad 2.1$$

$$\gamma_{op} - (\gamma_{wo} + \gamma_{wp}) < 0, \qquad 2.2$$

$$\gamma_{ow} - (\gamma_{po} + \gamma_{pw}) > 0. \qquad 2.3$$

As such, the combinations of polymer, core and surfactant are limited and the solvent evaporation method has mostly been applied in the formation of microcapsules from poly(methyl methacrylate),[24,33] polystyrene,[21] poly(lactide)[25] and cellulose.[34] In this Chapter, a microencapsulation procedure using rapid solvent evaporation was developed to prepare

microcapsules with hydrophobic core materials and a low-ceiling-temperature polymer shell wall, cyclic poly(phthalaldehyde) (cPPA).[12] Core-shell microcapsules has been fabricated *via* kinetic trapping mechanism as a result of rapid solvent removal, whereas an acorn-shaped microcapsule morphology was obtained under slow solvent evaporation (Figure 2.1). Tuning the polymer-to-core weight ratios and polymer concentrations in the oil phase, we identified the boundary conditions to kinetically trap the core-shell structure. This method was used to encapsulate a variety of hydrophobic payloads including a corrosion inhibitor jojoba oil (JJB),[26,33] mineral oil (MO), and the organotin catalyst dibutyltin dilaurate (DBTL). We also examined another low-ceiling-temperature polymer, poly(vinyl *tert*-butyl carbonate sulfone) (PV*t*BCS),[17] as an alternative shell wall material for the fabrication of stimuli-responsive microcapsules.

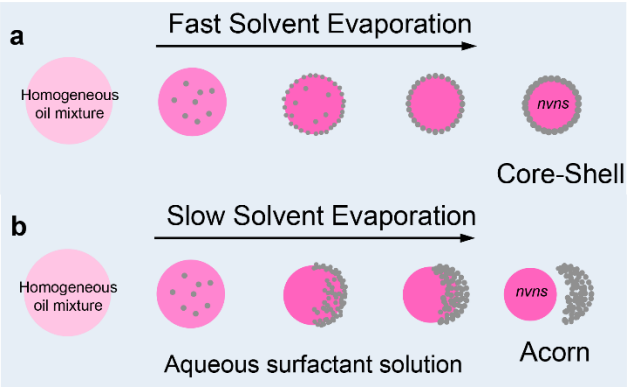

Figure 2.1. Schematic illustration of the effect of solvent evaporation rate on microcapsule's formation. Pink circles represent the O/W emulsion droplets; gray dots represent cPPA polymer precipitated in the emulsion droplets. (a) Core-shell microcapsules were formed under rapid solvent evaporation as cPPA migrated to the O/W interface. (b) Acorn-shaped morphologies were formed under slow evaporation as cPPA migrated to one side of the O/W droplets, leaving the polymer shell walls partially enclosing the cores (payload). After rinsing the microcapsules, the payloads and polymers were separated, resulting in hemispherical morphologies.

2.2 KINETICALLY TRAPPED CORE-SHELL CPPA MICROCAPSULES *VIA* RAPID SOLVENT EVAPORATION

2.2.1 Polymer Synthesis

Core-shell microcapsules were successfully prepared through the generation of an O/W emulsion followed by rapid solvent evaporation. Two low-ceiling-temperature polymers, cPPA and PV*t*BCS were used as the shell wall materials, separately. cPPA was synthesized by cationic polymerization using boron trifluoride etherate ($BF_3{\cdot}OEt_2$) as an initiator (M_n=55 kDa, PDI=1.6, Table 2.1).[12] PV*t*BCS was synthesized by free radical polymerization using *tert*-butyl hydroperoxide (*t*-BuOOH) as an initiator (M_n=19 kDa, PDI=3.2, Table 2.2).[17]

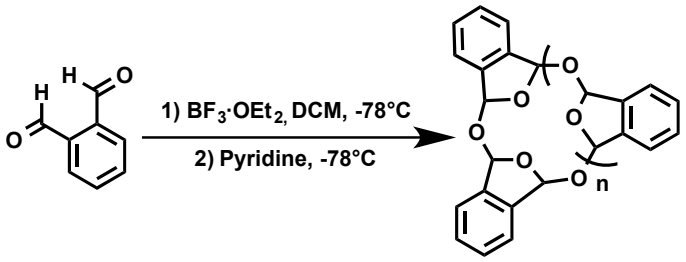

Table 2.1. Characterization of cPPA

Polymer	Yield(%)	M_n (kDa)	PDI
cPPA	78	55	1.6

cPPA was synthesized following literature procedures with slight modification.[12] Generally, 6 g purified monomer, *o*-phthalaldehyde (*o*-PA), was weighed into a Schlenk flask, and the solid was vacuumed and purged under N_2 three times before dissolving in anhydrous dichloromethane (DCM). The solution was cooled to -78 °C and $BF_3{\cdot}OEt_2$ was added dropwise. The solution was stirred for 40 min, then 0.2 mL pyridine was added, and the solution was left

stirring for another 2 h. The obtained polymer solution was then poured into cold methanol and the polymer was precipitated as a white powder. The polymer was further purified by re-dissolving in DCM and re-precipitating in cooled methanol twice. The polymer was dried under high vacuum for 24 h and then stored at -20 °C. Characterization of the polymer was consistent with the previously reported literature.

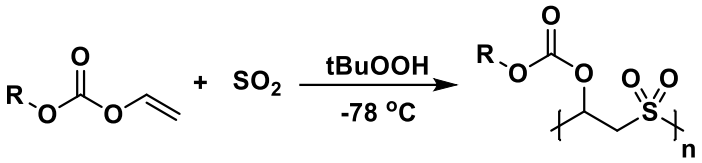

Table 2.2. Characterization of PVtBCS

Polymer	Yield(%)	M_n (kDa)	PDI
PV*t*BCS	79	19	3.2

The vinyl butyl carbonate monomers and PV*t*BCS were synthesized following the previously reported literature.[17] In brief, the polymerizations were as follows: a three-neck round-bottom flask was fitted with a cold-finger, a stir bar, a gas inlet adapter, and a rubber septum. The carbonate monomer (1 g) was added to the flask which was cooled in an acetone/dry ice bath. Sulfur dioxide (SO_2, 40 equiv.) was condensed in a three neck graduated cylinder and subsequently transferred to the three-neck flask *via* the cold finger. The solution was equilibrated at -78 °C for 5 min and then *t*-BuOOH (2.5 mol %) was added. The polymerization was allowed to proceed for 3 h. The polymer was drawn from the reaction mixture and transferred into cold methanol. After the methanol was decanted, the solid polymer was dissolved in chloroform and re-precipitated in cold methanol. The PV*t*BCS was dried for 3 h under high vacuum and freeze dried for 6 h to

prevent loss of molecular weight at room temperature. The polymers were then stored at -20 °C. Characterization of the polymers was consistent with the previously reported literature.[2]

2.2.2 Encapsulation Parameters and Microcapsule's Morphology

Before emulsification, a homogeneous mixture (oil) of cPPA, JJB, and DCM was prepared with the guidance of a ternary phase diagram at 25 °C (Figure 2.2). The phase boundary (green) demarcates solutions that are homogeneous (below) and biphasic (above). Before emulsification, the mass ratio of $m_{cPPA}/m_{JJB}/m_{DCM}$ in the oil mixture must be in the homogeneous regime to achieve a core-shell structure. Immediately after emulsification, DCM was removed rapidly under reduced pressure or slowly under ambient pressure in order to form the microcapsule's shell wall. Various $m_{cPPA}/m_{JJB}/m_{DCM}$ ratios and corresponding microcapsule's morphologies were examined in this chapter and listed in Table 2.3 and Table 2.4.

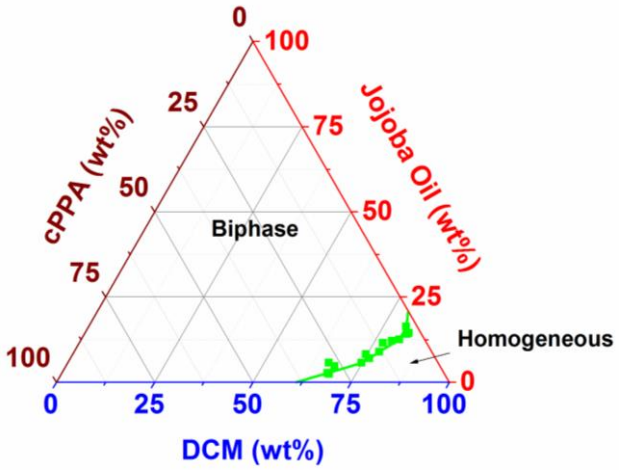

Figure 2.2. cPPA-JJB-DCM ternary phase diagram at 25 °C. The green squares denote cloud points for different compositions of cPPA, JJB and DCM. Green line was drawn to guide the visualization. Below the green line is the homogeneous regime; above the green line is the biphasic regime.

Table 2.3. Summary of Encapsulation Parameters Used in Microfluidic Emulsification

Entry	$m_{cPPA}/m_{JJB}/m_{DCM}$	m_{cPPA}/m_{JJB}	$m_{cPPA}/m_{oil\ phase}$[a]	Evap. [b]	Morphology	ξ (%)[e]
M1	1.33/1/13.26	1.33	0.085	Vac	Core-shell	107.6
M2	1.33/1/17.52	1.33	0.067	Vac	Core-shell	113.5
M3	1.33/1.33/13.26	1.00	0.084	Vac	Core-shell	109.4
M4	1/1/13.26	1.00	0.066	Vac	Core-shell	89.4
M5	0.66/0.66/13.26	1.00	0.045	Vac	Core-shell	105.6
M6	0.33/0.33/13.26	1.00	0.024	Vac	Core-shell [c]	-
M7	0.13/0.13/13.26	1.00	0.010	Vac	Core-shell [c]	-
M8	1/1.14/13.26	0.88	0.065	Vac	Acorn	-
M9	1/2.27/13.26	0.44	0.060	Vac	Fail [d]	-
M10	1/5.77/13.26	0.17	0.050	Vac	Fail [d]	-
M11	1/1.33/13.26	0.75	0.064	Vac	Acorn	30.1
M12	1/1/13.26	1.00	0.066	S. P.	Acorn	12.4

[a] $m_{oil\ phase}=m_{cPPA}+m_{JJB}+m_{DCM}$

[b] Vac represents rapid solvent evaporation under reduced pressure for 1 h; S. P. represents slow solvent evaporation under ambient pressure for 24 h (rotation rate < 30 rpm)

[c] These microcapsules exhibit microcracks on the shell wall surface

[d] No capsules were obtained

[e] Loading efficiency. Loading efficiency was calculated by comparing the experimental core loading to the theoretical core loading (detailed in 2.6.1.)

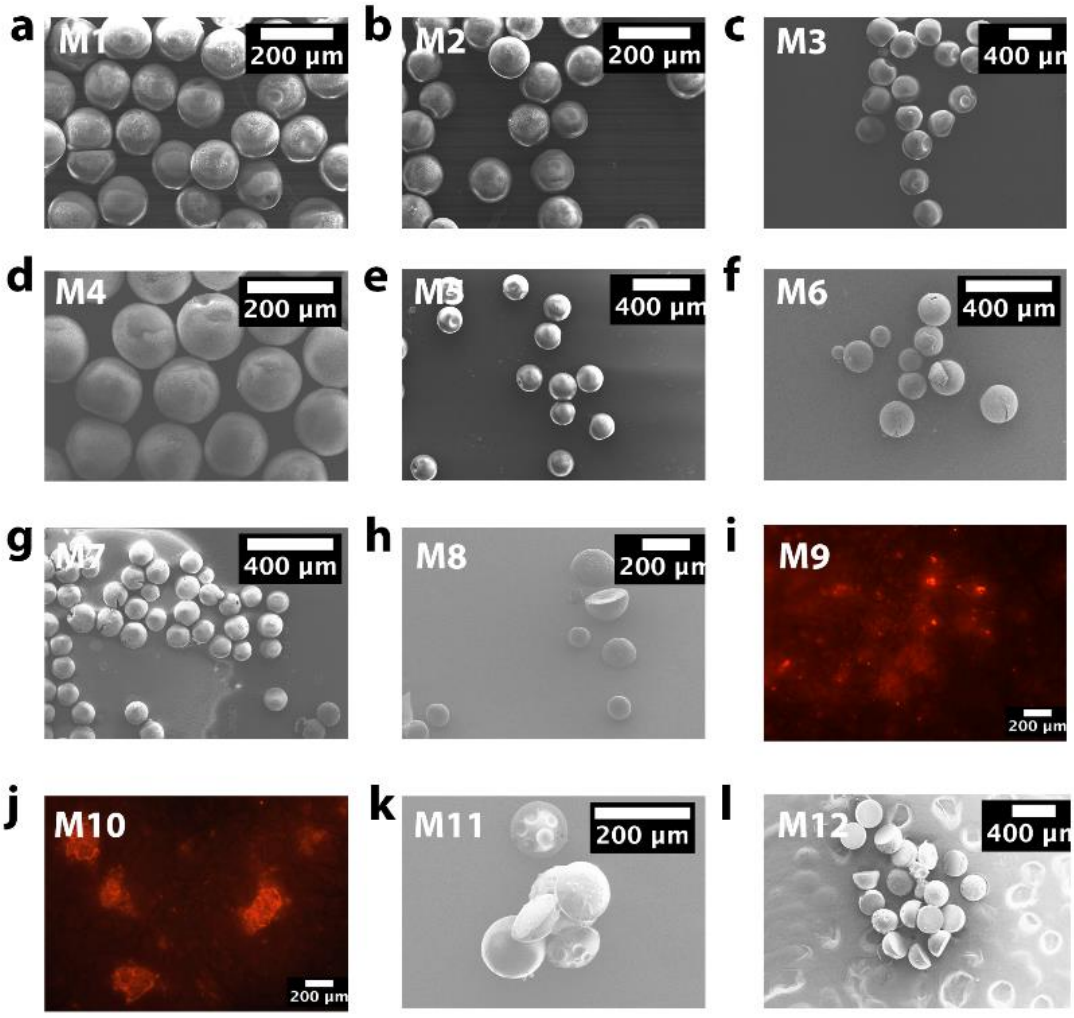

Figure 2.3. SEM and fluorescence microscopy images of encapsulation products. (a)-(h) and (k)-(l) are SEM images of encapsulation products using composition ratios of entries M1-M8 and M11-12 in Table 2.3. (i), (j) are fluorescence microscopy images of encapsulation products using composition ratios of entries M9 and M10, where no capsules were recovered from filter paper.

Table 2.4. Summary of Encapsulation Parameters Used in Bulk Emulsification

Entry	$m_{cPPA}/m_{JJB}/m_{DCM}$	m_{cPPA}/m_{JJB}	$m_{cPPA}/m_{oil\ phase}$[a]	Evap.[b]	Morphology	ξ (%)[c]
B1	1/0.75/13.26	1.33	0.067	Vac	Core-shell	89.0
B2	0.66/0.5/13.26	1.32	0.046	Vac	Core-shell	81.9
B3	0.33/0.25/13.26	1.32	0.024	Vac	Core-shell	90.0
B4	0.13/0.1/13.26	1.30	0.010	Vac	Acorn	-
B5	1/1/13.26	1.00	0.066	Vac	Core-shell	73.6
B6	0.66/0.66/13.26	1.00	0.045	Vac	Core-shell	92.6
B7	0.33/0.33/13.26	1.00	0.024	Vac	Acorn	-
B8	0.13/0.13/13.26	1.00	0.010	Vac	Acorn	-
B9	1/1.33/13.26	0.75	0.064	Vac	Acorn	25.2
B10	0.66/0.88/13.26	0.75	0.045	Vac	Acorn	34.5
B11	1/1/13.26	1.00	0.066	S. P.	Acorn	27.2

[a] $m_{oil\ phase}=m_{cPPA}+m_{JJB}+m_{DCM}$

[b] Vac represents rapid solvent evaporation under reduced pressure for 1 h; S. P. represents slow solvent evaporation under ambient pressure for 24 h (rotation rate < 30 rpm)

[c] Loading efficiency was calculated by comparing the experimental core loading to the theoretical core loading (detailed in 2.6.1.)

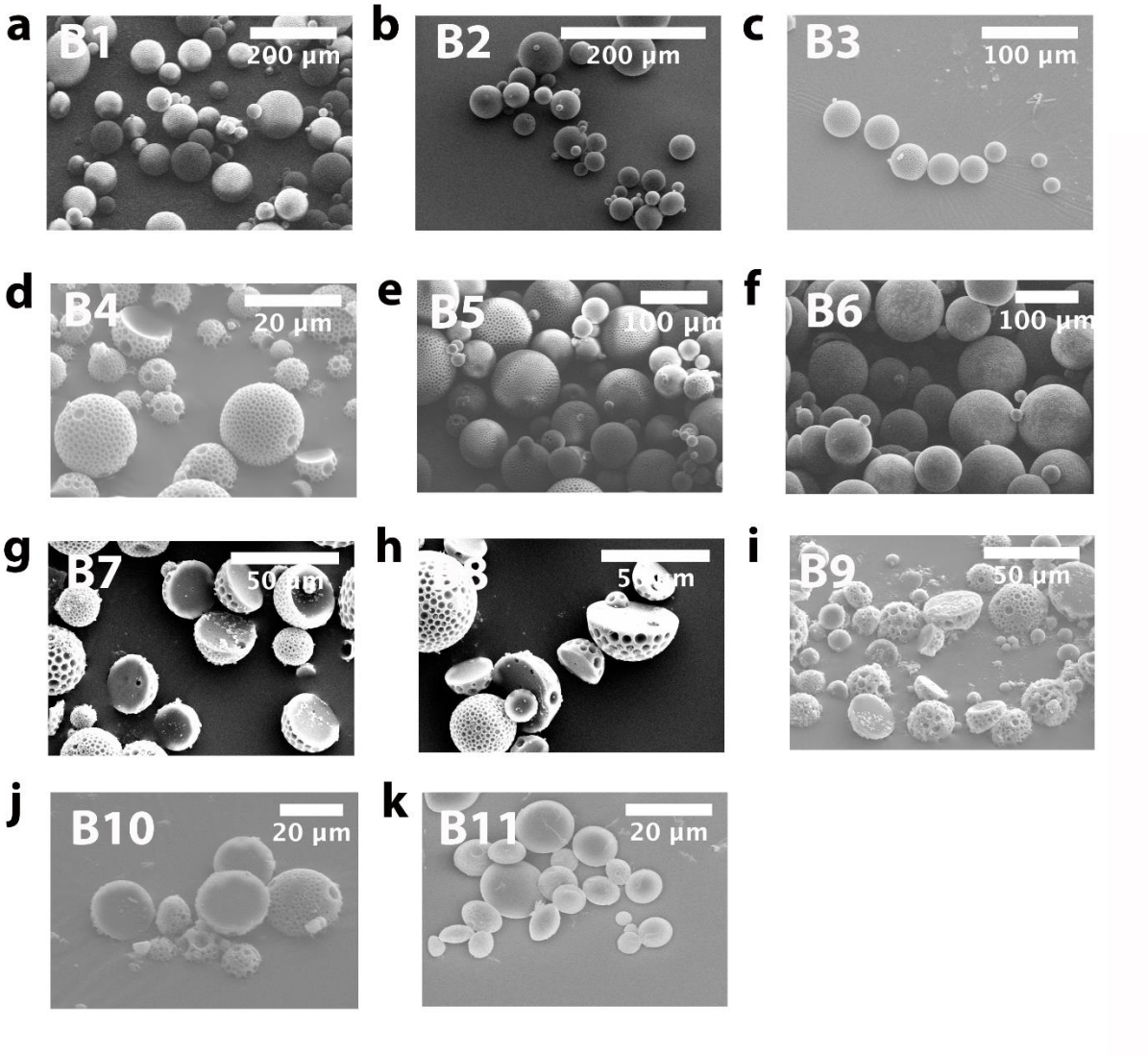

Figure 2.4. SEM images of cPPA microcapsules fabricated from bulk emulsification. Preparation ratios were following entries B1-B11 listed in Table 2.4.

2.2.3 Effect of Solvent Evaporation Rate on Microcapsule's Morphology

Both microfluidic and bulk emulsification methods were employed to substantiate our hypothesis of the effect of solvent evaporation rate on microcapsule's morphology. For most

studies, we used cPPA as the shell wall polymer, JJB as core materials (*nvns*), and DCM as *vs* ($m_{cPPA}/m_{JJB}/m_{DCM}$ = 1/1/13.26). An oil soluble fluorescence dye, Nile red, was added to organic phase to assist visualization and release profile measurements. We found that the core-shell structure was favored when DCM was removed rapidly. To illustrate the effect of solvent evaporation rate, microcapsule's morphology was monitored by microscopy during solvent evaporation (Figure 2.5). Immediately after microfluidic emulsification, mono-disperse droplets were obtained (Figure 2.5a). After evaporation under reduced pressure for 30 min, sphere-shaped intermediate morphologies were observed (Figure 2.5b). The diameter was reduced in the transition from the droplets (416.3 ± 3.0 μm) to the microcapsules (268.0 ± 4.7 μm), indicating the loss of DCM (Figure 2.6). After another 30 min evaporation, the final products were filtrated, cleaned and dried. SEM images revealed that the products were mono-dispersed, sphere-shaped, core-shell microcapsules (Figure 2.3d). In contrast, when the emulsion was allowed to evaporate under ambient pressure for 30 min, acorn-shaped morphologies were observed (Figure 2.5c). The final products were found to possess a hemispherical structure (Figure 2.3l). The O/W droplet morphology evolution under slow solvent evaporation is illustrated schematically in Figure 2.1b. Partially enclosed structures developed as the polymer phase migrated to one side of the droplet. Filtering and rinsing the acorn-shaped structures resulted in the removal of the JJB core and the formation of hemi-spherical polymer particles (Figure 2.3l).

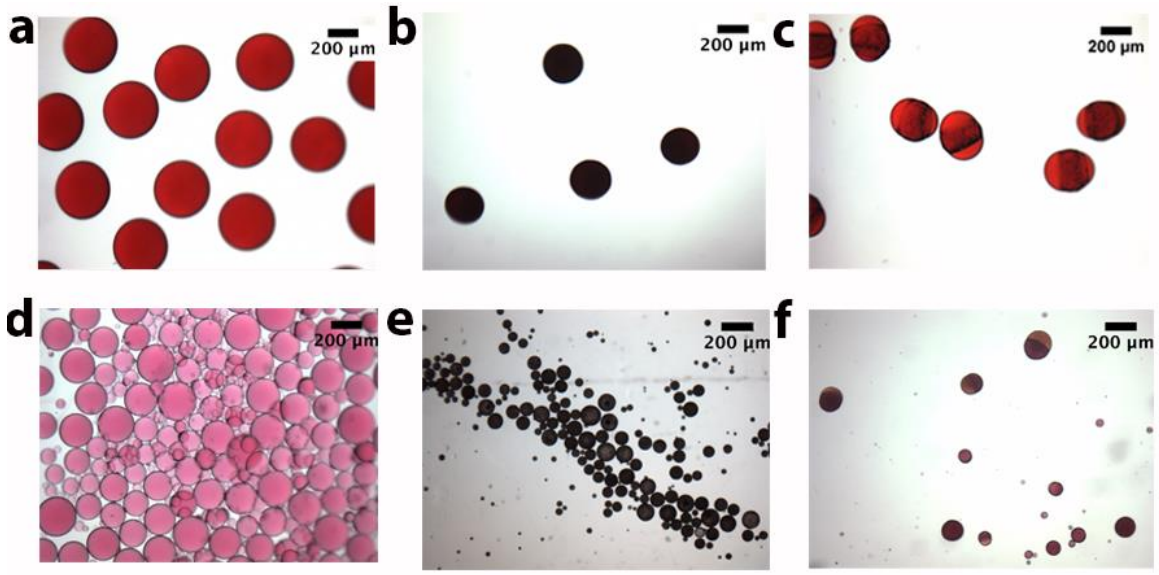

Figure 2.5. Optical microscopy images of O/W droplets during solvent evaporation. O/W droplets collected immediately after (a) microfluidic emulsification and (d) bulk emulsification; Sphere-shaped intermediate morphologies after 30 min evaporation at reduced pressure (fast evaporation) obtained from (b) microfluidic emulsification and (e) bulk emulsification; Acorn-shaped morphologies after 30 min evaporation at ambient pressure (slow evaporation) obtained from (c) microfluidic emulsification and (f) bulk emulsification.

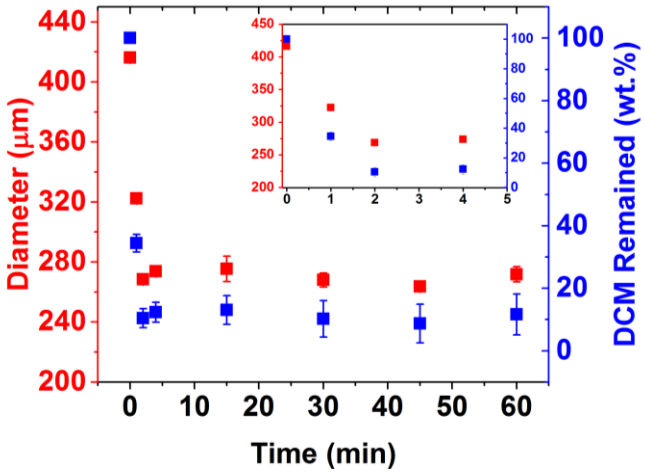

Figure 2.6. Changes in O/W droplet diameters as a function of time during DCM evaporation (red). The DCM remained (blue) is calculated based on the volume changes of the droplets and the densities of cPPA, JJB, and DCM. Note: The volume changes are assumed to be only attributed from DCM evaporation. Density: cPPA 0.790 g/mL, JJB 0.868 g/mL, and DCM 1.326 g/mL.

In order to validate the critical role of solvent evaporation rate on the formation of core-shell microcapsules, we performed parallel experiments with bulk emulsification. The O/W emulsion was generated by mechanical agitation (Figure 2.5d), followed by rapid or slow solvent evaporation. Similar to the microfluidics results, under rapid evaporation, a spherical structure was formed and a core-shell morphology was obtained (Figure 2.5e, Figure 2.4e,). When the evaporation rate was reduced, acorn-shaped morphologies were observed and final products were hemispherical (Figure 2.5f, Figure 2.4k).

Using rapid solvent evaporation to obtain core-shell structured microcapsules is contradictory to previous studies by Dowding *et al.* where slow solvent evaporation yielded better shell wall structures.[21] Their observations were explained by the canonical spreading coefficient theory developed by Torza and Mason.[32] This theory suggests that obtaining a core-shell structure after the *vs* evaporates requires the interfacial tension (γ) of any two phases in polymer (*p*), core (*o*) and surfactant (*w*) to satisfy the above mentioned relations 2.1-2.3. Under these relations, the core-shell structure is in a thermodynamic equilibrium state and a slower solvent evaporation rate allows enough time for polymers to uniformly migrate onto the O/W interface,[35,36] minimizing kinetic factors and forming a spherical core-shell structure with better barrier properties as shown by Dowding *et al.* In the present work, however, the acorn-shaped morphologies obtained under slow evaporation indicated that the spreading of *p* phase over *o* phase resulted in partial enclosure due to the thermodynamic driving forces; apparently the core-shell structure is a non-equilibrium state. By increasing the evaporation rate, the core-shell structure is kinetically trapped, overcoming the thermodynamic tendency to form acorn shaped morphologies.[28,29]

2.2.4 Microcapsule Diameter and Shell Wall Thickness

Using the microfluidics approach, we were able to precisely tune the microcapsule's diameters (D) from 149.3±7.5 μm to 244.1±5.7 μm by adjusting the flow rate ratios of the water and oil phases (Q_w/Q_o) from 120 to 10 (Figure 2.7), while maintaining $m_{cPPA}/m_{JJB}/m_{DCM}$ = 1/1/13.26. A linear relationship was found between the logarithm values of D and Q_w/Q_o.

The shell wall thickness was measured by imaging manually ruptured cPPA microcapsules. SEM images revealed that the shell wall thickness varied from 12.4±1.9 μm to 18.7±4.1 μm (Figure 2.8). The shell wall thickness was approximately 10% of the microcapsule's diameter (Table 2.5, column 4).

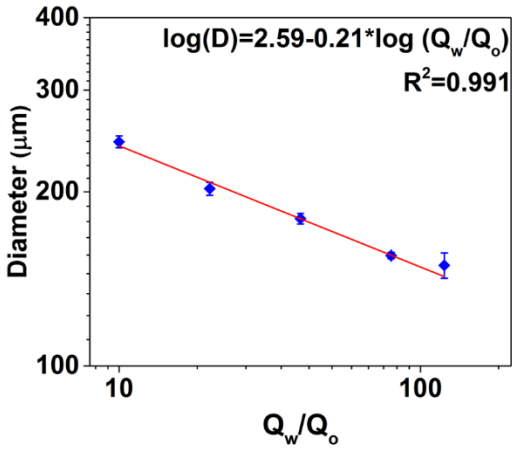

*Figure 2.7. Effect of water to oil flow rate ratios(Q_w/Q_o) on microcapsule's diameter. A linear relationship (red line) log(D)=2.59-0.21*log(Q_w/Q_o) (R^2=0.991) was observed between the logarithmic values of diameters (D) and Q_w/Q_o.*

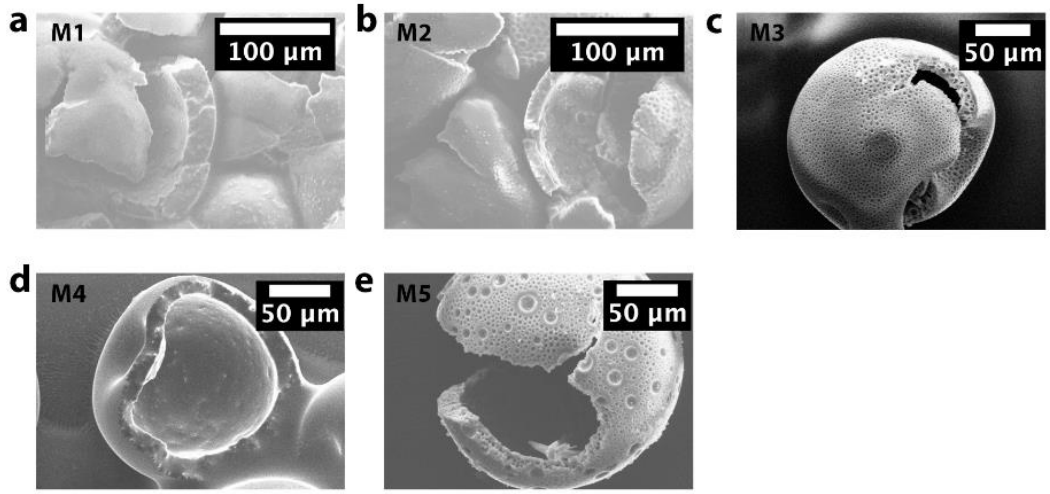

Figure 2.8. SEM images of crushed cPPA microcapsules prepared by microfluidics method showing shell wall thickness for (a) entry M1, (b) entry M2, (c) entry M3, (d) entry M4, and (e) entry M5 listed in Table 2.3.

Table 2.5. Summary of Microcapsule's Diameters and Shell Wall Thickness

Entry	Diameter (µm)	Shell Wall Thickness (µm)	Thickness/Diameter
M1	139.7±5.8	18.7±4.1	0.133
M2	119.9±4.7	12.4±1.9	0.103
M3	186.3±8.9	15.7±1.6	0.084
M4	168.2±16.6	13.7±1.7	0.081
M5	183.7±5.8	16.0±1.5	0.087

In bulk emulsification, microcapsules showed a polydisperse size distributions (Figure 2.9). When the agitation rate was maintained at 400 rpm and the oil phase composition was $m_{cPPA}/m_{JJB}/m_{DCM}$ = 1/1/13.26, the diameter ranged from 10-120 µm. Representative shell wall images are shown in Figure 2.10. Due to the polydispersity of the microcapsules, the ratio of the shell wall thickness to the microcapsule's diameters could not be estimated.

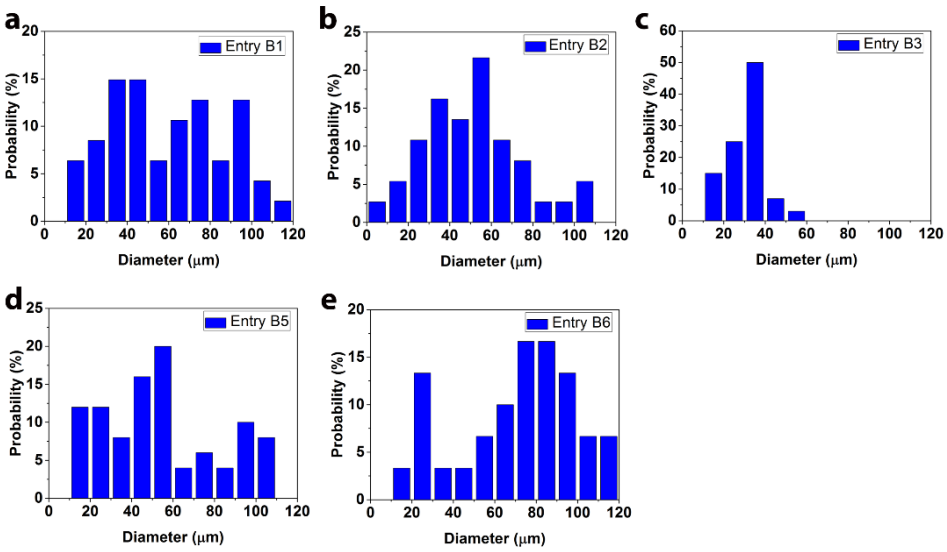

Figure 2.9. Size distributions of microcapsules prepared by bulk emulsification in (a) entry B1, (b) entry B2, (c) entry B3, (d) entry B5, and (e) entry B6 listed in Table 2.4.

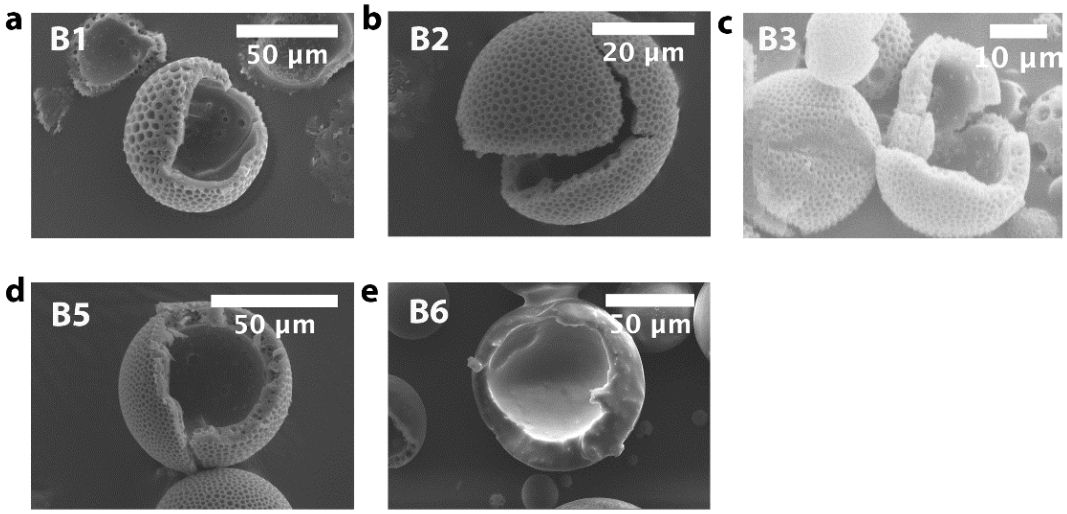

Figure 2.10. SEM images of crushed cPPA microcapsules prepared by bulk emulsification showing shell wall thickness in (a) entry B1, (b) entry B2, (c) entry B3, (d) entry B5, and (e) entry B6 listed in Table 2.4.

2.2.5 Core Materials Loading

Successful loading of the target payload (JJB) by the rapid solvent evaporation procedure was qualitatively examined by fluorescence microscopy (FM) after compressing few microcapsules between two glass slides. As shown in Figure 2.11b and Figure 2.11d, fluorescent liquid (Nile red in JJB) was released upon rupture of the microcapsules. Thermogravimetric analysis (TGA) was performed to quantify the loading of JJB in microcapsules (Figure 2.11e). Thermal profiles of cPPA microcapsules exhibited distinct mass loss at ca. 150 °C and at ca. 300 °C, attributed to the thermal decomposition of cPPA and evaporation of core JJB oil, respectively. Microcapsules fabricated using microfluidics contained approximately 44.7 wt% JJB (blue, solid line, loading efficiency ξ = 89.4%) and microcapsules from bulk emulsification contained 36.8 wt% JJB (blue, dashed line, loading efficiency ξ = 73.6%)). In contrast, the thermal profiles of the acorn-shaped microcapsules obtained from the slow solvent evaporation revealed that less than 20 wt% JJB was encapsulated in both microfluidic (Figure 2.16, entry M12, ξ = 12.4%) and bulk emulsification methods (Figure 2.17, entry B11, ξ = 27.2%).

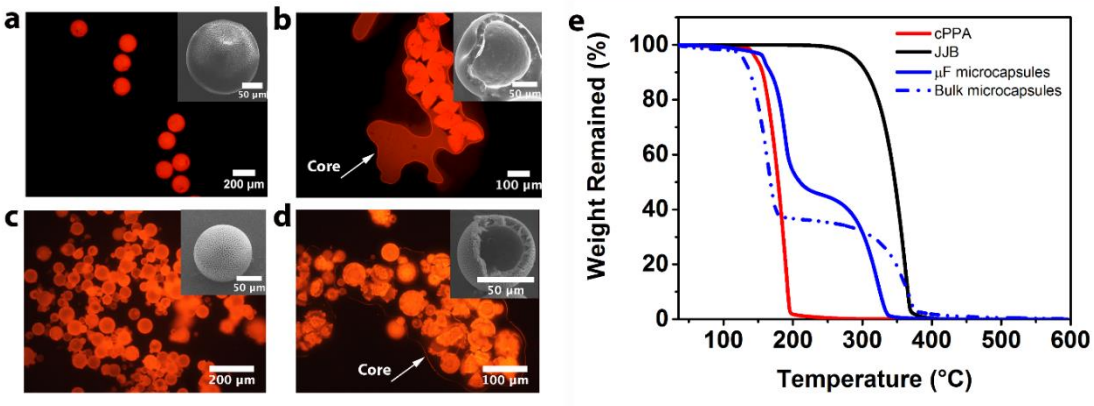

Figure 2.11. Microscopy images and thermal profiles of the cPPA core-shell microcapsules (prepared by $m_{cPPA}/m_{JJB}/m_{DCM}$=1/1/13.26, in microfluidic and bulk emulsifications followed by rapid solvent evaporation). Microcapsules fabricated from microfluidic emulsification (a) before

Figure 2.11. (cont.) crushing and (b) after crushing, showing the release of core material JJB (arrow); Insets are SEM images of intact and ruptured microcapsules showing exterior and cross-sectional shell wall morphologies; Microcapsules fabricated from bulk emulsification (a) before crushing and (d) after crushing, showing the release of core material JJB (arrow); Insets are SEM images of intact and ruptured microcapsules showing exterior and cross-sectional shell wall morphologies; (e) Thermal analysis of microcapsules fabricated with microfluidic emulsification (solid blue, L_{JJB}=44.7 wt%, ξ = 89.4%) and bulk emulsification (dashed blue, L_{JJB}=36.8 wt%, ξ = 73.6%). Thermal analysis of cPPA (red) and JJB (black) were plotted to assist the quantification of individual component loading in the microcapsules.

2.3 EFFECT OF MATERIALS COMPOSITIONS ON MICROCAPSULE'S MORPHOLOGY AND LOADING

To determine the criteria for obtaining core-shell microcapsules under rapid solvent evaporation, we investigated the boundary conditions for cPPA-JJB-DCM compositions at which the kinetic trapping effect overcomes thermodynamic driving forces. cPPA-JJB-DCM ternary system with varied compositions were tested and the encapsulation products were examined by SEM and FM. We summarized the microcapsule's morphologies with respect to the corresponding cPPA-JJB-DCM compositions in the ternary phase diagram shown in Figure 2.12.

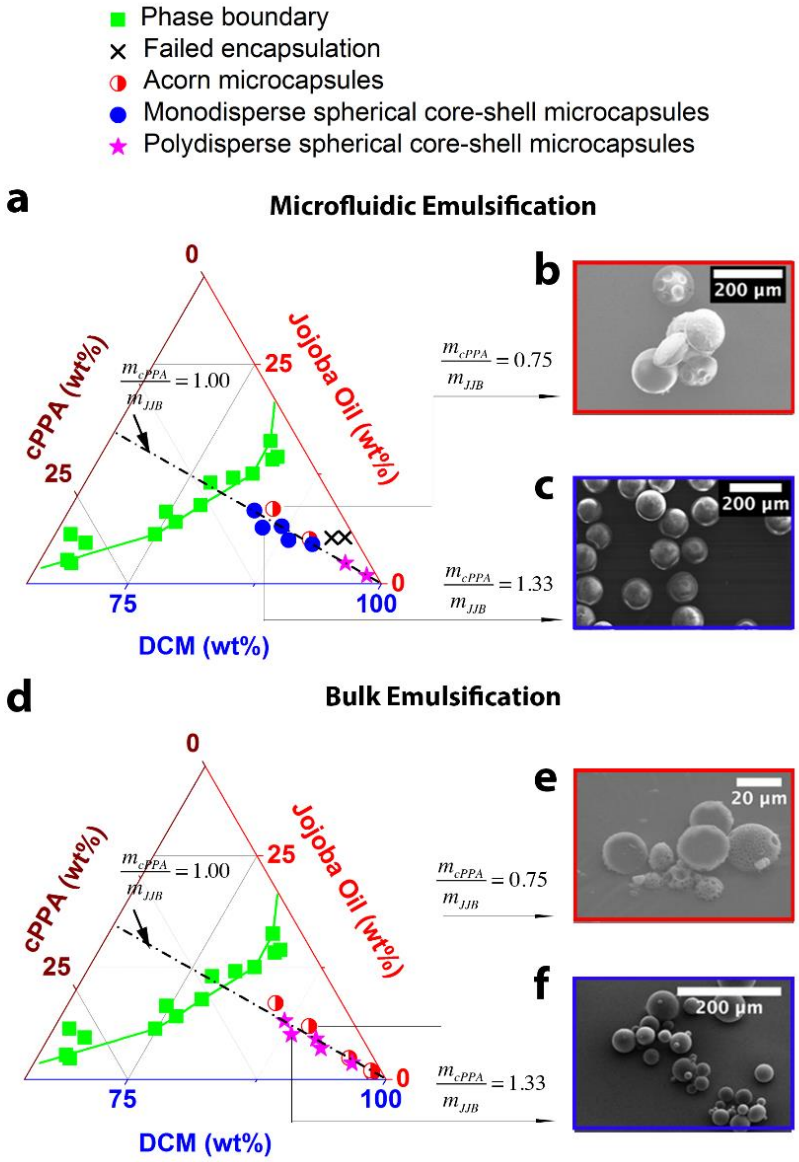

Figure 2.12. Effect of cPPA-JJB-DCM compositions on microcapsule's morphologies prepared by microfluidic and bulk emulsifications followed by rapid solvent evaporation. The cPPA-JJB-DCM phase boundary (▪) is replotted from Figure 2.2. The resulting morphologies of encapsulations over a range of chemical compositions are denoted on the ternary phase diagram for microfluidic emulsification (a-c) and bulk emulsification (d-f). (b) and (e) are SEM images for m_{cPPA}/m_{JJB} =0.75, which resulted in acorn-shaped microcapsules. (c) and (f) are SEM images for m_{cPPA}/m_{JJB} =1.33, which resulted in core-shell microcapsules. Note: the black dashed line is the mid-line of the phase diagram triangle, and the composition located on the mid-line has m_{cPPA}/m_{JJB} value of 1.00.

2.3.1 Effect of Polymer-to-Core Mass Ratios on Microcapsule's Morphology

The effect of polymer-to-core mass ratios (m_{cPPA}/m_{JJB}) was investigated for a range of values from 1.33 to 0.17 (Table 2.3, Figure 2.3). When $1.00 \leq m_{cPPA}/m_{JJB} \leq 1.33$, the encapsulation produced spherical core-shell microcapsules (entries M1-M7). When the m_{cPPA}/m_{JJB} was 0.88 and 0.75, acorn shaped microcapsules were obtained (Table 2.3, entry M8, M11). Further reduction of the m_{cPPA}/m_{JJB} ratio to 0.44 and 0.17, yielded no microcapsules after evaporation (Table 2.3, entry M9, M10). Representative SEM images are shown for acorn and core-shell microcapsules (Figures Figure 2.12b and Figure 2.12c). These results indicate that $m_{cPPA}/m_{JJB} \geq 1$ is required for obtaining the core-shell structure.

2.3.2 Effect of Polymer Concentrations on Microcapsule's Morphology

We also investigated the effect of polymer weight concentration in the oil phase ($m_{cPPA}/m_{oil\ phase}$) on microcapsule's morphology. The $m_{cPPA}/m_{oil\ phase}$ ratio was adjusted from 0.010 to 0.084, while maintaining the m_{cPPA}/m_{JJB} value at 1.00 (Table 2.3, entries M3-M7, Figure 2.3). When $0.045 \leq m_{cPPA}/m_{oil\ phase} \leq 0.084$, monodisperse spherical microcapsules were produced (Table 2.3, entries M3-M5). When $m_{cPPA}/m_{oil\ phase}$ was lowered to 0.024 and 0.010 (Table 2.3, entries M6-M7), the encapsulation products were polydisperse spherical microcapsules. SEM images also revealed that when $m_{cPPA}/m_{oil\ phase}$ was lower than 0.024, the shell walls exhibited micro-cracks (Figure 2.3f-g). Therefore, $m_{cPPA}/m_{oil\ phase} \geq 0.045$ is another requirement to obtain a core-shell structure.

2.3.3 Effect of Encapsulation Parameters on Microcapsule's Morphology in Bulk Emulsification Method

To confirm these boundary conditions discussed in 2.3.1 and 2.3.2, we performed bulk emulsification experiments with varied cPPA-JJB-DCM compositions (Table 2.4, Figure 2.4, Figure 2.12d-f). In good agreement with the microfluidic experiments, the composition requirements for kinetically trapping the core-shell structures were $m_{cPPA}/m_{JJB} \geq 1$ and $m_{cPPA}/m_{oil\ phase} \geq 0.045$ (Figure 2.12d-f, Table 2.4, Figure 2.4).

2.3.4 Effect of Encapsulation Parameters on Microcapsule's Core Loading

The loading of JJB in microcapsules with varied $m_{cPPA}/m_{JJB}/m_{DCM}$ ratios was examined by TGA (Figure 2.13). At m_{cPPA}/m_{JJB} =1.33, approximately 48.7 wt% and 35.3 wt% JJB oil loading was obtained by microfluidic and bulk emulsification methods, respectively. At m_{cPPA}/m_{JJB} =0.75, approximately 17.2 wt% and 14.4 wt% JJB oil loading was obtained by microfluidic and bulk emulsification methods, respectively. Generally, a core-shell morphology led to a higher payload (JJB) content than an acorn-shaped structure.

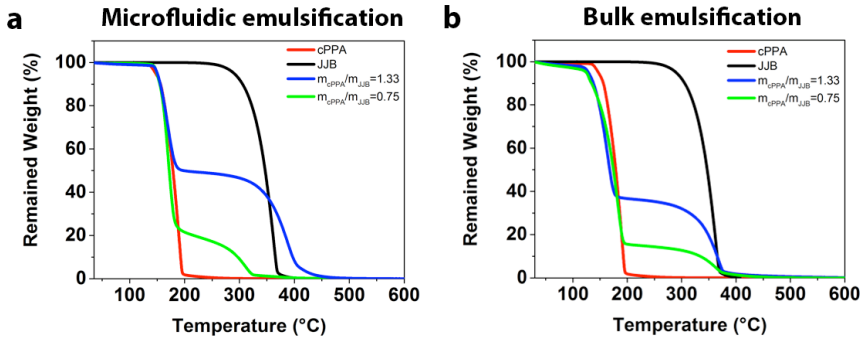

Figure 2.13. Thermal analysis of microcapsules prepared by different m_{cPPA}/m_{JJB} ratios in microfluidic and bulk emulsifications followed by rapid solvent evaporation. (a) Microcapsules prepared by microfluidic emulsification with m_{cPPA}/m_{JJB} =1.33 (blue, core-shell morphology, L_{JJB}=48.7 wt%) and m_{cPPA}/m_{JJB} =0.75 (green, acorn-shaped morphology, L_{JJB}=17.2 wt%). (b) Microcapsules prepared by bulk emulsification with m_{cPPA}/m_{JJB} =1.33 (blue, core-shell

Figure 2.13. (cont.) morphology, L_{JJB}=35.3 wt%) and m_{cPPA}/m_{JJB} =0.75 (green, acorn-shaped morphology, L_{JJB}=14.4 wt%). Thermal analysis of cPPA (red) and JJB (black) were plotted to assist the quantification of individual component loading in the microcapsules.

2.4 ACID TRIGGERED PAYLOAD RELEASE PROFILES FROM CPPA MICROCAPSULES

cPPA is known as an acid-responsive polymer.[35,36] Here, we evaluated the release profiles of cPPA microcapsules under acidic conditions (Figure 2.14). Since the release kinetics can vary with the dimension of microcapsules and shell wall thickness, we only tested microcapsules fabricated by microfluidic emulsification with the composition of $m_{cPPA}/m_{JJB}/m_{DCM}$=1/1/13.26, which has moderate diameter (168.2±16.6 μm) and shell wall thickness (13.7±1.7 μm) (Table 2.3, Table 2.5, entry M4). For release analysis, we selected heptane as the suspension medium. Heptane is a non-solvent for cPPA and its hydrophobicity will not inhibit JJB oil release. The release of the JJB oil core was measured by monitoring the fluorescent intensity (Nile red) of the microcapsules as a function of time. The release of encapsulated JJB oil in pure heptane at different concentrations of trifluoroacetic acid (TFA) was plotted in Figure 2.14. In pure heptane, less than 5% release of JJB was observed after 48 h, indicating the microcapsules are stable under neutral conditions. As the concentration of acid in heptane increased, the core material (JJB) was released at a faster rate, indicating faster depolymerization of the cPPA shell wall. The core release from cPPA microcapsules was modeled by fitting the results to an empirical logarithmic dose response equation,[37]

$$R = \frac{R_0 - R_f}{1+(t/t_{1/2})^n} + R_f \qquad 2.4$$

where R_0 is the initial release value, R_f is the final release value, $t_{1/2}$ is the release half-life and n is the order exponent. Fitting parameters are summarized in Table 2.6. The exponent n of this logarithmic fit is found to be ca. 3. A smaller half-life value indicates a faster payload release rate.

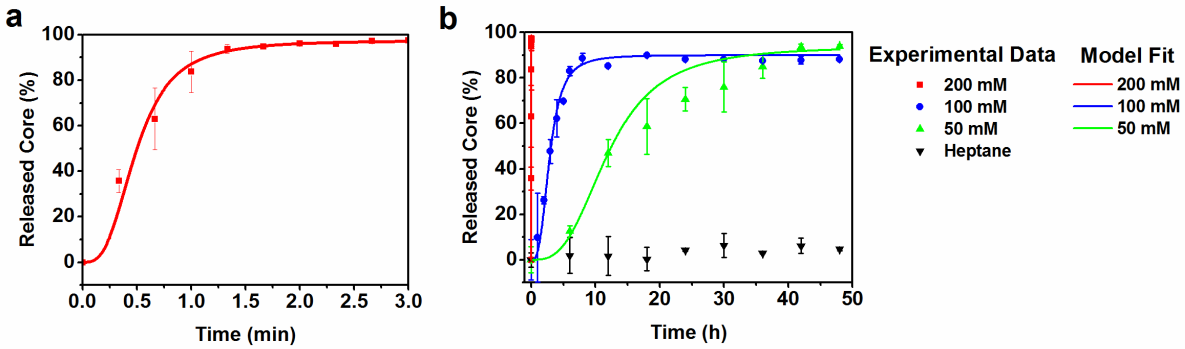

Figure 2.14. Microcapsule's release profiles over 48 h. (a) Release profile in response to 200 mM TFA in heptane. (b) Release profiles in response to 200 mM TFA (red), 100 mM TFA (blue), and 50 mM TFA (green) in heptane and pure heptane (black). Data plots were fitted with an empirical logarithmic function. Error bars represent standard deviation from three experiments.

Table 2.6. Release Profile Model Parameters

TFA concentration (mM)	R_0	R_f	n	$t_{1/2}$ (h)
50	0	93.9	3	12.0
100	0	90.0	3	2.9
200	0	97.4	3	0.008

2.5 GENERALITY OF THE RAPID SOLVENT EVAPORATION METHOD TO ALTERNATIVE CORE AND SHELL WALL MATERIALS

2.5.1 Encapsulation of Alternative Core Materials in cPPA Microcapsules

To illustrate the generality of this encapsulation procedure, we encapsulated other hydrophobic core materials using microfluidic emulsification and rapid solvent evaporation.

Following one of the compositions satisfying the kinetic trapping conditions, $m_{cPPA}/m_{JJB}/m_{DCM}$ = 1/1/13.26, we replaced JJB with mineral oil (MO) or a liquid tin catalyst dibutyltin dilaurate (DBTL). The spherical, core-shell structure was confirmed by SEM images as shown in Figure 2.15. For these hydrophobic payloads, the loading efficiency is hard to estimate due to the lack of distinct two-stage weight loss as observed in cPPA/JJB microcapsules.

2.5.2 Microcapsules with Alternative Shell Wall Materials

To further test the generality of this procedure, we also successfully encapsulated JJB in a poly(olefin sulfone) shell wall. We selected PV*t*BCS as an alternative shell wall material due to its responsiveness to thermal stimuli (decomposition onset temperature is 91 °C).[17] Using the condition, $m_{PVtBCS}/m_{JJB}/m_{CHCl3}$=1/0.75/14.92, we obtained polydisperse core-shell microcapsules with PV*t*BCS shell wall *via* microfluidic emulsification and rapid solvent evaporation procedure (Figure 2.15). The loading of the core materials was about ~51.5 wt%. By comparing to the feed ratio of core materials, we estimated the loading efficiency to be ~120%. We attributed this number to slow degradation of shell wall materials PV*t*BCS during the encapsulation procedure.[17]

Table 2.7. Summary of Encapsulation Parameters

Polymer (g)	Core (g)	Solvent (g)	Encap.	Evap.	Morphology
cPPA 0.1	DBTL 0.1	DCM 1.326	Microfluidics	Vac	Core-shell
cPPA 0.1	MO 0.1	DCM 1.326	Microfluidics	Vac	Core-shell
PV*t*BCS 0.1	JJB 0.075	$CHCl_3$ 1.492	Microfluidics	Vac	Core-shell

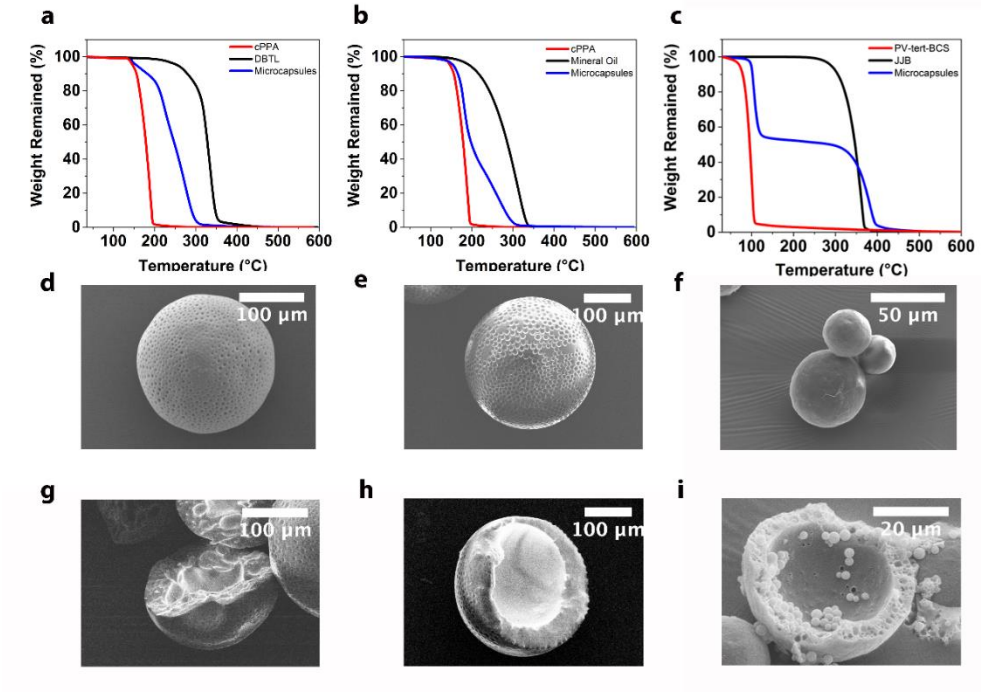

Figure 2.15. Thermal analysis and SEM images of cPPA microcapsules with different core materials or different shell walls as listed in Table 2.7. TGA profiles of (a) cPPA-DBTL microcapsules, (b) cPPA-MO microcapsules, and (c) PVtBCS-JJB microcapsules. SEM images of (d) intact cPPA-DBTL microcapsules, (e) intact cPPA-MO microcapsules, and (f) PVtBCS-JJB microcapsules; SEM images of broken (g) cPPA-DBTL microcapsules, (h) cPPA-MO microcapsules,3 and (i) PVtBCS-JJB microcapsules showing the shell wall thickness and core-shell structure.

2.6 EXPERIMENTAL DETAILS

2.6.1 Materials and Instrumentations

Unless otherwise noted, all starting materials were obtained from Sigma Aldrich and used as received. The monomer *o*-PA (98%, Alfa-Aesar) was purified by hot filtration followed by a single recrystallization according to a literature procedure.[12] *t*-BuOOH was purchased from Sigma Aldrich as a 5-6 M solution in decane and was assumed to be 5.5 M for all calculations. SO_2 (anhydrous, 99.98%) was purchased from Airgas in lecture bottles. DCM was obtained from an anhydrous solvent delivery system equipped with activated alumina columns. All glassware was oven dried prior to use. The synthesis of cPPA and synthesis of the poly(olefin sulfone)s followed previous literature procedures with minor modifications.[12,17] The polymer structure was confirmed on ^{1}H NMR spectra using a Varian 500 MHz spectrometer.

Analytical gel permeation chromatograph (GPC) analyses were performed with a Waters1515 Isocratic HPLC pump, a Waters (2998) Photodiode Array Detector, a Waters (2414) Refractive Index Detector, a Waters (2707) 96-well autosampler, and a series of 4 Waters HR Styragel columns (7.8 x 300mm, HR1, HR3, HR4, and HR5) in THF at 30 °C. The GPC was calibrated using monodisperse polystyrene standards.

The thermal properties of microcapsules were characterized on a TA Instrument Q50 TGA and a Mettler Toledo TGA851^e. Dynamic TGA experiments were performed by heating samples from 25 to 650 °C at a rate of 10 °C/ min. A purge gas of N_2 at 60 mL/min was used for all experiments.

The loading efficiency is calculated by comparing the actual JJB core loading (L_{JJB}) in microcapsules with the theoretical JJB core loading (L_{JJB}^{th}) in the microcapsules.

$$Loading\ efficiency\ (\xi) = \frac{L_{JJB}}{L_{JJB}^{th}} \times 100\% \qquad 2.5$$

The L_{JJB} was determined by the remained wt% from TGA profiles at 250 °C. And the theoretical L_{JJB}^{th} is calculated from,

$$L_{JJB}^{th} = \frac{m_{JJB}}{m_{JJB} + m_{cPPA}} \times 100\% \qquad 2.6$$

where m_{JJB} and m_{cPPA} are the initial mass of JJB and cPPA used for microcapsule's preparation.

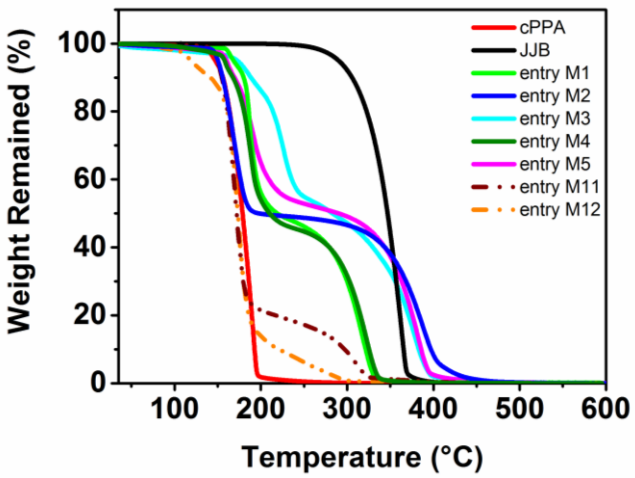

Figure 2.16. TGA profiles of cPPA microcapsules fabricated from microfluidic emulsification. Preparation ratios were following entries M1-M12 in Table 2.3. TGA profiles of entries M6-M10 in Table 2.3. M6-M8 were not collected due to low yield.

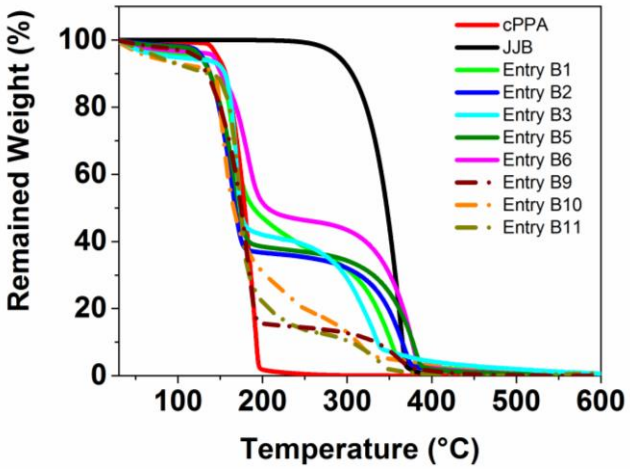

Figure 2.17. TGA profiles of cPPA microcapsules fabricated from bulk emulsification. Preparation ratios were following entries B1-B11 in Table 2.4. TGA profiles of entries B4, B7 and B8 in Table 2.4 were not collected due to low yield.

The distribution coefficient of Nile red in the shell wall cPPA and the core materials JJB oil is determined by a fluorospectrometer (HORIBA Scientific, FluoroMax-4). To quantify the Nile red concentration, the mass of microcapsules (bulk emulsification, $m_{cPPA}/m_{JJB}/m_{DCM}$ = 1/1/13.26) were accurately measured. The microcapsules were crushed between two glass slides, rinsed repeatedly with heptane to dissolve the released core materials from the mechanically

crushed microcapsules. The broken shell wall was then centrifuged, collected and dried before dissolving in DCM. Fluorescence intensities of the core Nile red/heptane solution and shell wall Nile red/DCM solution were measured by the fluorospectrometer. The concentration of Nile red in the core or shell wall was determined from the Nile red calibration curve (Figure 2.18) in the corresponding solvent. The distribution coefficient (m/m) of Nile red in JJB/cPPA was calculated as 0.557 ± 0.050 based on three parallel experiments.

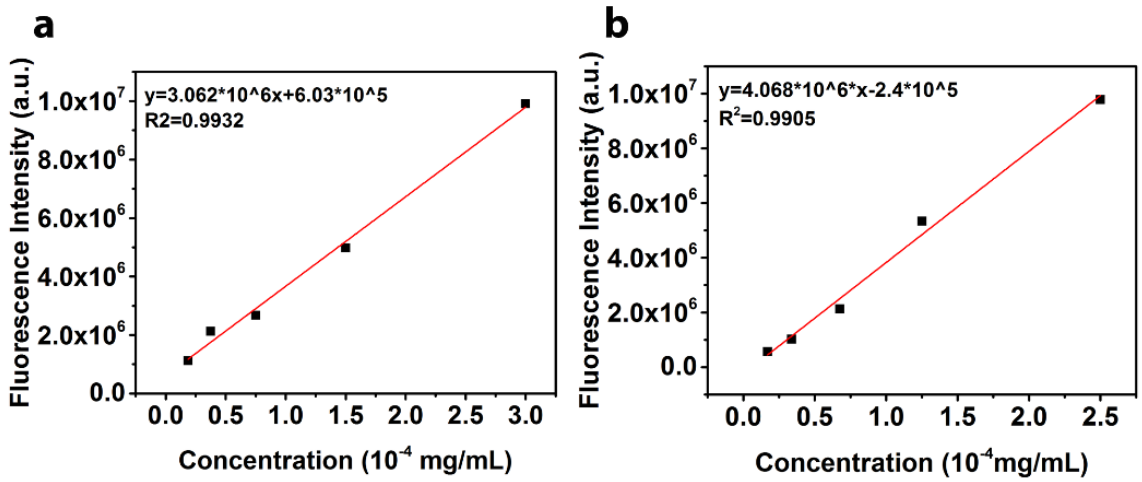

Figure 2.18. Nile red calibration curve in (a) DCM and (b) heptane.

Visualization of microcapsule's morphology and triggering experiments was performed on a Leica DMR optical microscope (fluorescence mode). Scanning electron microscopy (SEM) was performed using a Hitachi S-4700. Before SEM imaging, samples were sputter-coated with Au/Pd to eliminate surface charging effects. Image J software was used to measure the diameter of microcapsules.

The density of polymer was measured by gas pycnometer (Quantachrome Instrument Ultrapyc 1200e) using pulse mode.

The ternary phase diagram for cPPA, DCM (*vs*), and JJB (*nvns*) was determined by mixing accurate amounts of the three components in a 7-mL glass vial.[21,27] The total mass of the mixed solution with the glass vial and stir bar was recorded. Then, the solvent was evaporated while stirring at 25 °C until the solution became cloudy. The total mass was reweighed immediately and mass difference was attributed to the evaporation of DCM only. Weight fractions of cPPA, JJB, and DCM at the phase boundary were then determined. Fourteen samples were prepared with different mass compositions to complete the phase diagram.

2.6.2 Microcapsules Prepared by Microfluidic Emulsification

cPPA microcapsules were fabricated using a flow-focusing microfluidic device to prepare emulsions, followed by solvent evaporation. This technique enables controlled formation of emulsion droplets with approximately identical geometry,[38,39] which is quite useful for thorough characterization of microcapsule's properties. Microfluidic devices were composed of two tapered cylindrical glass capillaries inserted into the opposing ends of a square glass capillary (Figure 2.19). A homogeneous mixture of various compositions of cPPA, JJB, and DCM was injected into the left cylindrical capillary. Nile red was added in the oil phase to facilitate visualization and release profile measurements. A 2.5 wt% aqueous solution of the emulsifier poly(vinyl alchohol) (PVA, M_w=89,000-98,000, 99% hydrolyzed) was injected into the region between the right capillary and square capillary. O/W droplets formed as the two flows merged at the orifice of the collection tube. The generated droplets were collected in a round bottom flask filled with 1 wt% PVA solution. Immediately after collection, flasks were connected to a rotary evaporator to remove DCM at reduced pressure for 1 h (rapid evaporation). For slower evaporation, the emulsion was stirred (<30 rpm) at ambient conditions until evaporation was complete (ca. 24 h).

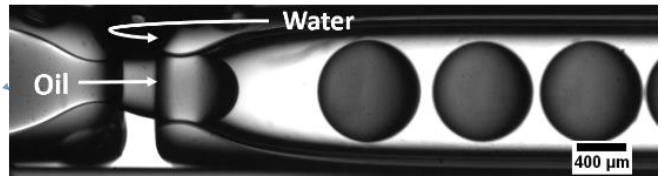

Figure 2.19. A optical microscopy image of O/W droplets generated by a microfluidic device. Device and image courtesy: Dr. Mostafa Yourdkhani.

To monitor DCM evaporation, aliquots of the emulsion were taken at periodic time intervals and imaged by fluorescence microscopy (FM) to observe variations in microcapsule's morphologies and diameters. A total of 15-20 droplets were imaged at each time point. Assuming the volume loss in the droplets was only due to DCM evaporation, and knowing the initial weight percentage and density of DCM, JJB, and cPPA, we calculated the residual DCM based on the reduction in microcapsule's diameter (Figure 2.6).

After evaporation, microcapsules were collected by vacuum filtration and washed with 500 mL deionized water to remove residual surfactant followed by another wash with 50 mL of heptane to remove residual organics. Microcapsules were subsequently dried at room temperature for 24 h to complete the drying process.

2.6.3 Microcapsules Prepared by Bulk Emulsification

cPPA microcapsules were fabricated by bulk emulsification followed by solvent evaporation. A homogeneous mixture of various compositions of cPPA, JJB, and DCM was prepared. The mixture was added dropwise into a 1 wt% PVA solution under 400 rpm agitation. The container was capped and the O/W emulsion was stirred for another 10 min. The emulsion was then poured into 100 mL of 1 wt% PVA solution in a round bottom flask, and the solvent

DCM was removed by rotary evaporation for 1 h at reduced pressure or following slow evaporation procedure as used in microfluidics method. The resulting microcapsules were cleaned and dried by the same procedure used in microfluidic method.

2.6.4 Release Profile Measurements

The release profiles of microcapsules were obtained based on the change of Nile red fluorescence intensities inside the microcapsules, following a previous literature procedure with minor modifications.[20] A sample of 10-20 microcapsules was placed in a 96-well plate. Heptane, a non-solvent for the shell wall polymer cPPA, was used as a medium to prepare TFA solutions. It should be noted that heptane may have a plasticizing effect on cPPA polymers. The TFA-heptane solution was added to samples of cPPA microcapsules. The well plate was then sealed to prevent solution evaporation. Fluorescence microscopy images were captured at designated time intervals over a period of 48 h. For each sample, all imaging parameters, such as exposure time, color contrast, and color balance were held constant during data collection. To determine the release profile, Image J was used to measure the mean gray value of the microcapsules. The change of mean gray values represents the remaining core percentage by normalization. For each concentration, at least three samples were prepared and imaged.

2.7 REFERENCES

Notes: This chapter is a collaborative work with Dr. Mostafa Yourdkhani and Dr. Catherine M. Possanza Casey. S.T. authored the text, performed cPPA synthesis, prepared and characterized microcapsules (TGA, SEM, release profiles, fluorescence microscopy), and analyzed results. Dr. Mostafa Yourdkhani developed the microfluidic devices, authored related text and worked with S.T. in microcapsule's preparation and results analysis. Dr. Catherine M. Possanza Casey synthesized PV*t*BCS and authored related text. This chapter has previously been published in the following reference: **Tang, S.**; Yourdkhani, M.; Possanza Casey, C. M.; Sottos, N. R.; White, S. R.; Moore, J. S., "Low-Ceiling-Temperature Polymer Microcapsules with Hydrophobic Payloads via Rapid Emulsion-Solvent Evaporation", *ACS Appl. Mater. Interfaces* **2017**, *9*, 20115-20123. **DOI:** 10.1021/acsami.7b05266. They are reproduced/adapted with permission. Copyright © 2017 American Chemical Society.

(1) White, S. R.; Sottos, N. R.; Geubelle, P. H.; Moore, J. S.; Kessler, M. R.; Sriram, S. R.; Brown, E. N.; Viswanathan, S. Autonomic Healing of Polymer Composites. *Nature* **2001**, *409*, 794–797.

(2) Jackson, A. C.; Bartelt, J. A.; Braun, P. V. Transparent Self-Healing Polymers Based on Encapsulated Plasticizers in a Thermoplastic Matrix. *Adv. Funct. Mater.* **2011**, *21*, 4705–4711.

(3) Blaiszik, B. J.; Kramer, S. L. B.; Grady, M. E.; McIlroy, D. A.; Moore, J. S.; Sottos, N. R.; White, S. R. Autonomic Restoration of Electrical Conductivity. *Adv. Mater.* **2012**, *24*, 398–401.

(4) Odom, S. A.; Tyler, T. P.; Caruso, M. M.; Ritchey, J. A.; Schulmerich, M. V; Robinson, S. J.; Bhargava, R.; Sottos, N. R.; White, S. R.; Hersam, M. C.; Moore, J. S. Autonomic Restoration of Electrical Conductivity Using Polymer-Stabilized Carbon Nanotube and Graphene Microcapsules. *Appl. Phys. Lett.* **2012**, *101*, 043106–043111.

(5) Yuan, Y. C.; Rong, M. Z.; Zhang, M. Q.; Chen, J.; Yang, G. C.; Li, X. M. Self-Healing Polymeric Materials Using Epoxy / Mercaptan as the Healant. *Macromolecules* **2008**, *41*, 5197–5202.

(6) Huang, M.; Yang, J. Facile Microencapsulation of HDI for Self-Healing Anticorrosion Coatings. *J. Mater. Chem.* **2011**, *21*, 11123–11130.

(7) Zhao, Y.; Fickert, J.; Landfester, K.; Crespy, D. Encapsulation of Self-Healing Agents in Polymer Nanocapsules. *Small* **2012**, *8*, 2954–2958.

(8) Esser-Kahn, A. P.; Odom, S. A.; Sottos, N. R.; White, S. R.; Moore, J. S. Triggered Release from Polymer Capsules. *Macromolecules* **2011**, *44*, 5539–5553.

(9) Johnston, A. P.; Such, G. K.; Caruso, F. Triggering Release of Encapsulated Cargo. *Angew. Chemie - Int. Ed.* **2010**, *49*, 2664–2666.

(10) Wang, H. C.; Zhang, Y.; Possanza, C. M.; Zimmerman, S. C.; Cheng, J.; Moore, J. S.;

Harris, K.; Katz, J. S. Trigger Chemistries for Better Industrial Formulations. *ACS Appl. Mater. Interfaces* **2015**, *7*, 6369–6382.

(11) DiLauro, A. M.; Robbins, J. S.; Phillips, S. T. Reproducible and Scalable Synthesis of End-Cap-Functionalized Depolymerizable Poly(phthalaldehydes). *Macromolecules* **2013**, *46*, 2963–2968.

(12) Kaitz, J. A.; Diesendruck, C. E.; Moore, J. S. End Group Characterization of Poly(phthalaldehyde): Surprising Discovery of a Reversible, Cationic Macrocyclization Mechanism. *J. Am. Chem. Soc.* **2013**, *135*, 12755–12761.

(13) Fan, B.; Trant, J. F.; Wong, A. D.; Gillies, E. R. Polyglyoxylates: A Versatile Class of Triggerable Self-Immolative Polymers from Readily Accessible Monomers. *J. Am. Chem. Soc.* **2014**, *136*, 10116–10123.

(14) Fan, B.; Trant, J. F.; Gillies, E. R. End-Capping Strategies for Triggering End-to-End Depolymerization of Polyglyoxylates. *Macromolecules* **2016**, *49*, 9309–9319.

(15) Lobez, J. M.; Swager, T. M. Disassembly of Elastomers: Poly(olefin sulfone)−Silicones with Switchable Mechanical Properties. *Macromolecules* **2010**, *43*, 10422–10426.

(16) Lobez, J. M.; Swager, T. M. Radiation Detection: Resistivity Responses in Functional Poly(olefin Sulfone)/carbon Nanotube Composites. *Angew. Chemie - Int. Ed.* **2010**, *49*, 95–98.

(17) Lee, O. P.; Lopez Hernandez, H.; Moore, J. S. Tunable Thermal Degradation of Poly(vinyl Butyl Carbonate Sulfone)s via Side-Chain Branching. *ACS Macro Lett.* **2015**, *4*, 665–668.

(18) Possanza Casey, C. M.; Moore, J. S. Base-Triggered Degradation of Poly(vinyl Ester Sulfone)s with Tunable Sensitivity. *ACS Macro Lett.* **2016**, *5*, 1257–1260.

(19) DiLauro, A. M.; Abbaspourrad, A.; Weitz, D. A.; Phillips, S. T. Stimuli-Responsive Core-Shell Microcapsules with Tunable Rates of Release by Using a Depolymerizable Poly(phthalaldehyde) Membrane. *Macromolecules* **2013**, *46*, 3309–3313.

(20) Grolman, J. M.; Inci, B.; Moore, J. S. pH-Dependent Switchable Permeability from Core–Shell Microcapsules. *ACS Macro Lett.* **2015**, *4*, 441–445.

(21) Dowding, P. J.; Atkin, R.; Vincent, B.; Bouillot, P. Oil Core-Polymer Shell Microcapsules Prepared by Internal Phase Separation from Emulsion Droplets. I. Characterization and Release Rates for Microcapsules with Polystyrene Shells. *Langmuir* **2004**, *20*, 11374–11379.

(22) Andersson Trojer, M.; Nordstierna, L.; Bergek, J.; Blanck, H.; Holmberg, K.; Nydén, M. Use of Microcapsules as Controlled Release Devices for Coatings. *Adv. Colloid Interface Sci.* **2015**, *222*, 18–43.

(23) Yow, H. N.; Routh, A. F. Formation of Liquid Core-Polymer Shell Microcapsules. *Soft Matter* **2006**, *2*, 940–949.

(24) Tasker, A. L.; Hitchcock, J. P.; He, L.; Baxter, E. A.; Biggs, S.; Cayre, O. J. The Effect of Surfactant Chain Length on the Morphology of Poly(methyl Methacrylate) Microcapsules for Fragrance Oil Encapsulation. *J. Colloid Interface Sci.* **2016**, *484*, 10–16.

(25) Yin, W.; Yates, M. Z. Encapsulation and Sustained Release from Biodegradable Microcapsules Made by Emulsification/freeze Drying and Spray/freeze Drying. *J. Colloid Interface Sci.* **2009**, *336*, 155–161.

(26) Persico, P.; Carfagna, C.; Danicher, L.; Frere, Y. Polyamide Microcapsules Containing Jojoba Oil Prepared by Interfacial Polymerization. *J Microencapsul.* **2005**, *22*, 471–486.

(27) Loxley, A.; Vincent, B. Preparation of Poly(methylmethacrylate) Microcapsules with Liquid Cores. *J. Colloid Interface Sci.* **1998**, *208*, 49–62.

(28) Pekarek, K. J.; Jacob, J. S.; Mathiowitz, E. Double-Walled Polymer Microspheres for Controlled Drug Release. *Nature* **1994**, *367*, 258–260.

(29) Berkland, C.; Pollauf, E.; Pack, D. W.; Kim, K. Uniform Double-Walled Polymer Microspheres of Controllable Shell Thickness. *J. Control. Release* **2004**, *96*, 101–111.

(30) Andersson Trojer, M.; Nordstierna, L.; Nordin, M.; Nydén, M.; Holmberg, K. Encapsulation of Actives for Sustained Release. *Phys. Chem. Chem. Phys.* **2013**, *15*, 17727–17741.

(31) Li, M.; Rouaud, O.; Poncelet, D. Microencapsulation by Solvent Evaporation: State of the Art for Process Engineering Approaches. *Int. J. Pharm.* **2008**, *363*, 26–39.

(32) Torza, S; Mason, S. G. Three Phase Interaction in Shear and Electrical Field. *J. Colloid Interface Sci.* **1970**, *33*, 67–83.

(33) Chetouani, A; Hammoui, B.;Benkaddour, M. Corrosion Inhibition of Iron in Hydrochloric Acid Solution by Jojoba Oil. *Pigm. Resin Technol.* **2004**, *33*, 26–31.

(34) Fundueanu, G.; Constantin, M.; Esposito, E.; Cortesi, R.; Nastruzzi, C.; Menegatti, E. Cellulose Acetate Butyrate Microcapsules Containing Dextran Ion-Exchange Resins as Self-Propelled Drug Release System. *Biomaterials* **2005**, *26*, 4337–4347.

(35) Lopez Hernandez, H.; Kang, S. K.; Lee, O. P.; Hwang, S. W.; Kaitz, J. A.; Inci, B.; Park, C. W.; Chung, S.; Sottos, N. R.; Moore, J. S.; Rogers, J. A.; White, S. R. Triggered Transience of Metastable Poly(phthalaldehyde) for Transient Electronics. *Adv. Mater.* **2014**, *26*, 7637–7642.

(36) Park, C. W.; Kang, S. K.; Hernandez, H. L.; Kaitz, J. A.; Wie, D. S.; Shin, J.; Lee, O. P.; Sottos, N. R.; Moore, J. S.; Rogers, J. A.; White, S. R. Thermally Triggered Degradation of Transient Electronic Devices. *Adv. Mater.* **2015**, *27*, 3783–3788.

(37) Seefeldt, S. S.; Jensen, J. E.; Fuerst, E. P. Log-Logistic Analysis of Herbicide Dose-Response Relationships. *Weed Technol.* **1995**, *9*, 218–227.

(38) Chu, L. Y.; Utada, A. S.; Shah, R. K.; Kim, J. W.; Weitz, D. A. Controllable Monodisperse Multiple Emulsions. *Angew. Chemie - Int. Ed.* **2007**, *46*, 8970–8974.

(39) Shah, R. K.; Kim, J.; Agresti, J. J.; Weitz, D. A.; Chu, L. Fabrication of Monodisperse Thermosensitive Microgels and Gel Capsules in Microfluidic Devices. *Soft Matter* **2008**, *4*, 2303–2309.

CHAPTER 3 : INVESTIGATING ION CO-ACTIVATION EFFECT ON TRANSIENT POLYMER MICROCAPSULES

3.1 INTRODUCTION

Programmable materials that respond to complex input signals instead of individual signals are of interest to achieve CPU like functions. Microcapsules triggered by molecular pairs or regulated by co-activators are significant to design logic-gate materials and autonomous chemical systems with feedback controlled loops (Figure 3.1).[1] For example, feedback controlled reaction cascades can be designed with microcapsules ruptured by a pair of molecules and/or physical signals that discussed in Chapter 1. The ruptured microcapsules may deliver payloads that react with complementary payloads released from other microcapsules for self-healing applications.[2] Alternatively, microcapsules can react with functionalized surface to immobilize the array of microcapsules and print materials *in situ.*[3] Thus, chemical or physical signals are translated and amplified into macroscopic responses of polymer formation. The resulting polymerization increases local viscosity that can further trigger reaction-diffusion induced patterning [4–6] or materials regeneration.[7] In another scenario, the payload is a co-activator that catalyze the shell wall rupture in the presence of a primary trigger. The microcapsule's shell wall is triggered and ruptured by the primary stimuli and the released co-activators further catalyze the shell wall erosion, resulting in autocatalytic payload release. Motivated by the goal of designing advanced logic-gated microcapsules, in Chapter 3, we investigated the ionic effect at the solid/liquid interfaces in cPPA microcapsule's suspensions.

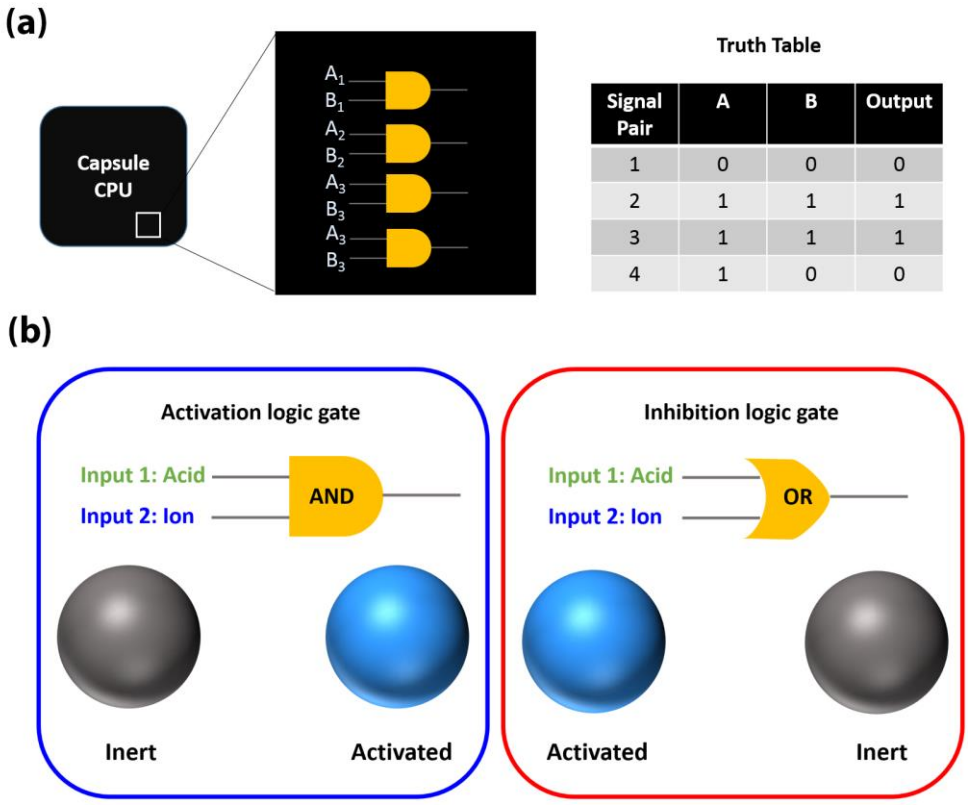

Figure 3.1. Concept scheme of designing a logic gate with microcapsules. (a) A CPU consists of microcapsules arrays, suspensions or microcapsule-based composites. Microcapsules are programmed to respond in the presence of one or multiple pairs of signals. (b) Individual logic gate for activated (blue) and inert (grey) microcapsules. An activated microcapsule releases functional payload driven by shell erosion, triggered by the presence of two stimuli. An inert microcapsule releases encapsulated payload driven by diffusion. The shell wall does not undergo significant erosion without the presence of at least one stimuli.

3.2 ION CO-ACTIVATION EFFECT OF LICL ON CPPA MICROCAPSULE'S SHELL WALL DEPOLYMERIZATION

3.2.1 Depolymerization Products

In Chapter 2, we have developed an encapsulation procedure to produce cPPA microcapsules. The acid triggered cPPA depolymerization generates a cationic intermediate.[8,9] We hypothesize that the addition of ions affects the cPPA depolymerization kinetics *via* ion-

polymer interactions, leading to tunable depolymerization rates modulated by varied acid and ion concentrations.

The ion co-activation effect was demonstrated and confirmed in LiCl by nuclear magnetic resonance (NMR) spectroscopy (Figure 3.2). Unless otherwise noted, the microcapsules used in all depolymerization analysis were prepared by bulk emulsification followed by rapid solvent evaporation procedure (detailed in Chapter 2, 2.6.3) with cPPA (M_n=58 kDa, PDI=1.6) as the shell walls and jojoba oil (JJB) as the core materials. The oil mixture for O/W emulsion has the composition of $m_{cPPA}/m_{JJB}/m_{DCM}$=1/0.75/13.26 and Nile red was added in the oil mixture to assist visualization and payload release measurements. The cPPA microcapsules were suspended in methanol-d_4 (~5 mg/mL) solutions containing trifluoroacetic acid (TFA, 0.01 M), LiCl (0.01 to 1 M) or both. We choose methanol as the medium because the microcapsules disperse and suspend favorably and this solvent has good solubility for salts compared with other organic solvents. In the ^{1}H NMR spectrum of samples suspended in TFA (0.01 M in methanol-d_4) for 24 h, no apparent depolymerization was observed (Figure 3.2, red), because this concentration of TFA was too low to initiate rapid depolymerization at the cPPA microcapsule's interfaces. Also, the spectrum of samples suspended in LiCl (1 M in methanol-d_4) showed no peaks for depolymerization products (Figure 3.2, black). In contrast, cPPA depolymerization was observed in solutions containing both TFA (0.01 M) and LiCl (1 M) based on the highlighted aromatic and acetal peaks. The depolymerization products were *trans* (**1t**) and *cis* (**1c**) isomers of 1,3-dihydro-1,3-dimethoxyisobenzofuran and 1,2-bis(dimethoxymethyl)benzene (**2**). The depolymerization products were consistent with previous report on *o*-PA reacting with methanol and the depolymerization products remained the same in all triggering conditions regardless of adding LiCl (Figure 3.3).[10]

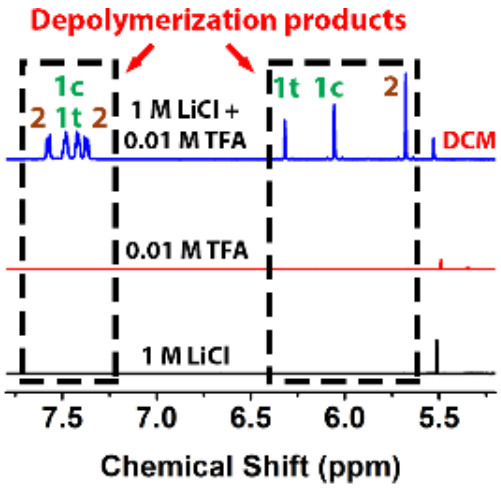

Figure 3.2. ^{1}H NMR spectra of microcapsules suspended in various triggering solutions after 24 h treatment. Microcapsules were suspended in 1 M LiCl (black), 0.01 M TFA (red), and 1 M LiCl + 0.01 M TFA (blue), solvent: methanol-d_4. No depolymerization was observed in 1 M LiCl or 0.01 M TFA. Depolymerization products in 1 M LiCl + 0.01 M TFA mixed solution was shown in Figure 3.3. Note: DCM was residual solvent from the microcapsule's preparation.

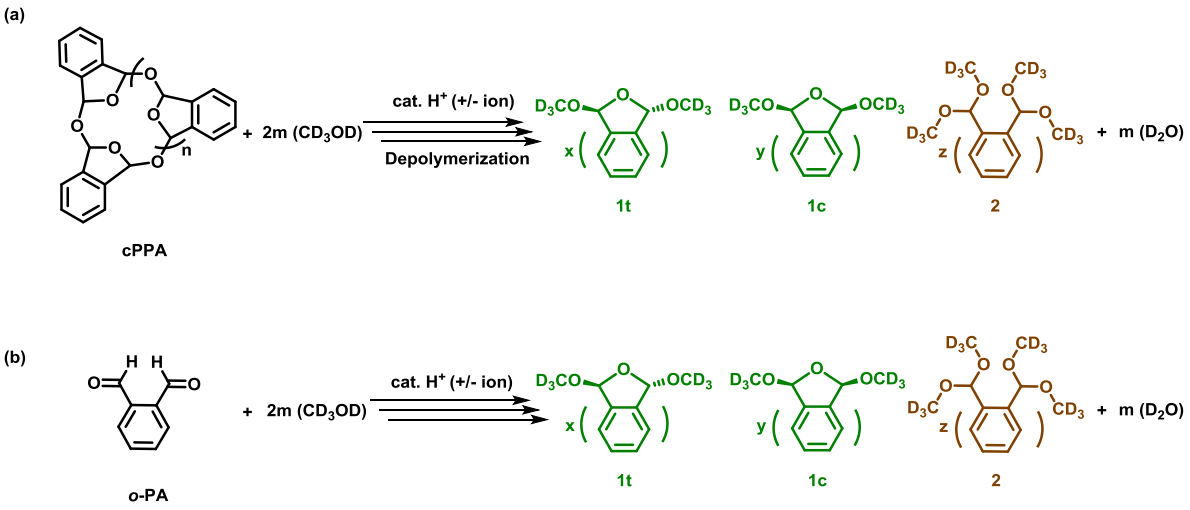

Figure 3.3. Reaction schemes of cPPA depolymerization products in methanol-d_4 and o-PA reacting with methanol-d_4. (a) cPPA depolymerization products in methanol-d_4. (b) o-PA monomers react with methanol-d_4. Depolymerization products remained the same regardless of the depolyerization conditions (+/- ions) used in this chapter. Stoichiometry: $x+y+z=n+2$, $x+y+2z=m$.

3.2.2 Tunable Depolymerization Rates Co-Activated by LiCl

To quantify the depolymerization rates in different triggering solutions, we tracked the depolymerization mol % by NMR over 48 h using ethylene glycol (~5 mg/mL) as an internal standard to produce depolymerization profiles (Figure 3.4). Fitting the depolymerization profiles with an empirical logarithmic function,[11] we extracted the shell wall depolymerization half-life (t_{D50}). In either TFA (0.01 M) or LiCl (1 M) solutions, no depolymerization was observed and no t_{D50} values were obtained (Figure 3.4, red and black traces). t_{D50} in TFA (0.01 M) + LiCl (1 M) mixed solution was 6.0 ± 0.5 h (Figure 3.4, blue trace). This t_{D50} was shorter than that of microcapsules suspended in 0.5 M TFA solution (12.2 ± 0.3 h) (Figure 3.4, pink trace). LiCl did not affect the depolymerization by itself, but led to significant acceleration in the depolymerization rates with acid, showing a co-activation effect.

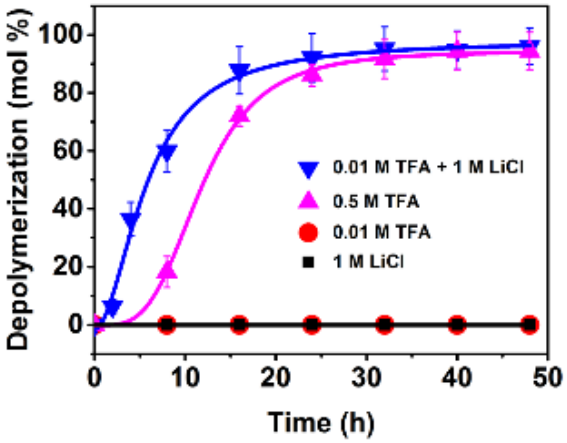

Figure 3.4. LiCl co-activation effect on cPPA depolymerization. Shell wall depolymerization profiles of cPPA microcapsules (M_n=58 kDa, ~5mg/mL) suspended in 1 M LiCl (black), 0.01 M TFA (red), 0.5 M TFA (pink), and 1 M LiCl + 0.01 M TFA (blue), solvent: methanol-d_4. Depolymerization profiles was measured by NMR using ethylene glycol (~5 mg/mL) as an internal standard. Data plots were fitted with an empirical logarithmic function (quantification procedures were detailed in 3.5.4). Error bars represent standard deviation of three experiments.

To further demonstrate the co-activation effect of LiCl and tunable depolymerization rates, we varied the combinations of TFA and LiCl concentrations and plotted the corresponding depolymerization mol % at designated time points in Figure 3.5. At 4 h, the synergistic trigger (TFA + LiCl) resulted in depolymerization mol % ranging from 12 mol % to more than 90 mol %, and apparently, always led to more depolymerization mol % compared with the individual trigger TFA or LiCl of the same concentration. The lowest concentration used was 0.01 M TFA + 0.01 M LiCl. This mixed solution generated 16 mol % depolymerization at 24 h compared with 0 mol % depolymerization in 0.01 M LiCl only or 0.01 M TFA solutions only.

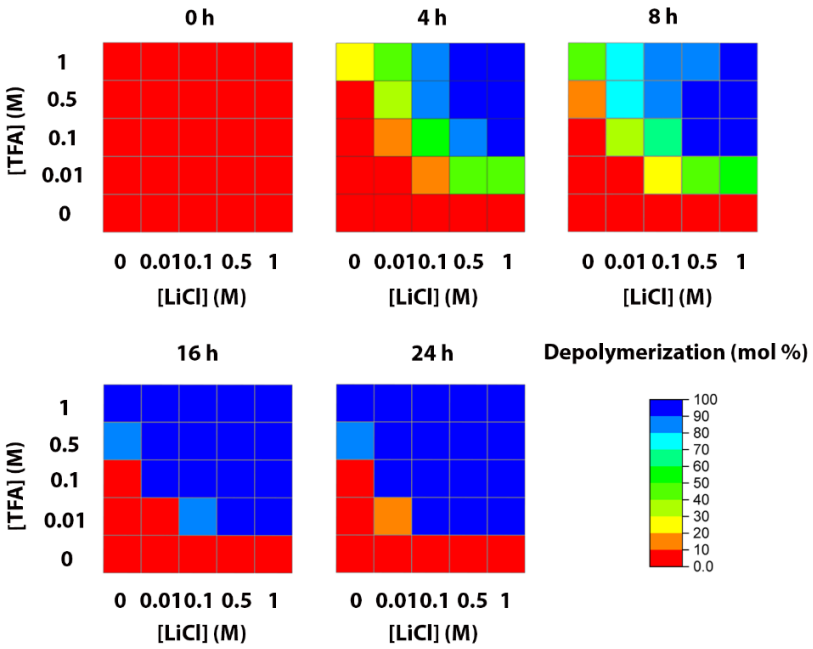

Figure 3.5. Summary of cPPA microcapsule's shell walls (M_n=58 kDa, ~5 mg/mL) depolymerization mol % in varied concentrations of TFA and LiCl at 0, 4, 8, 16, and 24 h, solvent: methanol-d_4. The depolymerization mol % was measured by NMR using ethylene glycol (~5 mg/mL) as an internal standard.

The microcapsule's morphology changes induced by cPPA shell wall depolymerization were confirmed under SEM and optical microscopy (Figure 3.6-Figure 3.8). Microcapsules

suspended in acid-free/salt-free methanol, TFA (0.01 M), or LiCl (0.1-1 M) displayed similar morphologies, identical to the as-synthesized cPPA microcapsule's morphology (Figure 3.14). They all possessed a golf-ball like surface, attributed to the rapid solvent evaporation procedure.[12] In contrast, microcapsules suspended in solutions containing both TFA (0.01 M) and LiCl (0.1-1 M) exhibited shell wall erosion with visible damage (Figure 3.6, Figure 3.7).

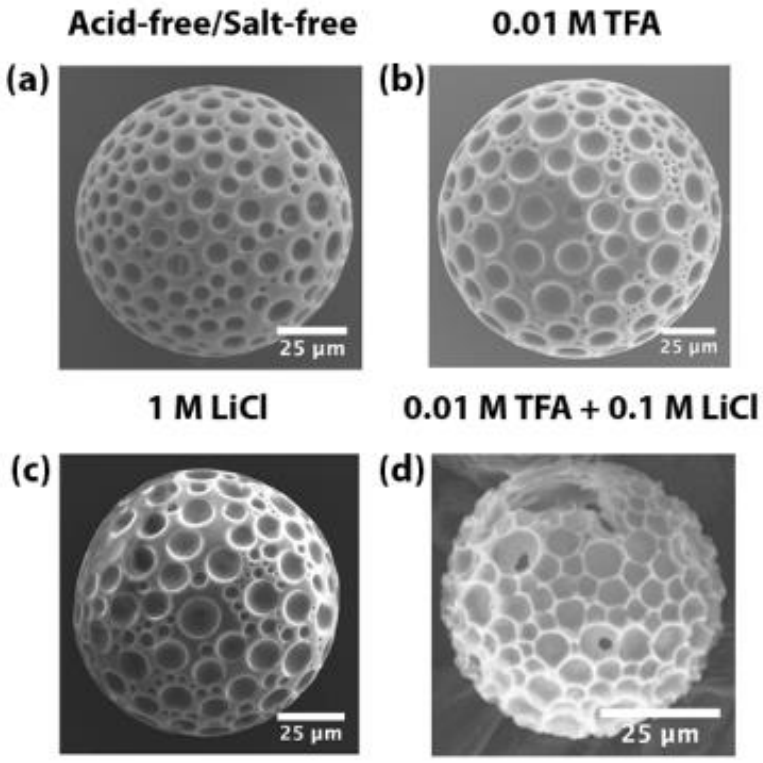

Figure 3.6. SEM images of individual microcapsules suspended in various solutions showing the morphology changes after 24 h treatment. cPPA microcapsules (M_n=58 kDa, ~5 mg/mL) were suspended in (a) methanol (acid-free salt-free), (b) 0.01 M TFA, (c) 1 M LiCl, and (d) 0.01 M TFA + 0.1 M LiCl. After 24 h treatment, the microcapsule's suspensions were filtered and the microcapsules left on the filter paper were imaged. Microcapsules suspended in (a)-(c) solutions showed no depolymerization and identical morphologies, which are similar to as-synthesized microcapsule's morphology (shown in Figure 3.14). The microcapsules suspended in the (d) solution containing both TFA and LiCl showed the most shell wall erosion compared with other samples after 24 h treatment.

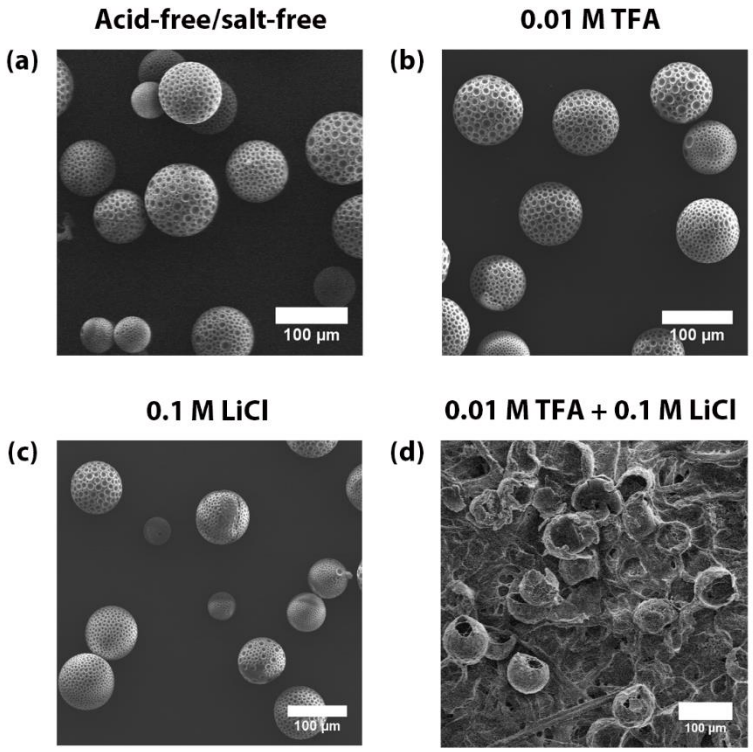

Figure 3.7. SEM images of cPPA microcapsules suspended in various solutions for 24 h. cPPA microcapsules (M_n=58 kDa, ~5 mg/mL) were suspended in (a) methanol (acid-free salt-free), (b) 0.01 M TFA, (c) 0.1 M LiCl, and (d) 0.01 M TFA + 0.1 M LiCl. After 24 h treatment, the microcapsule's suspensions were filtered and the microcapsules left on the filter paper were imaged. Microcapsules suspended in (a)-(c) solutions showed no depolymerization and identical morphologies, which are similar to as-synthesized microcapsule's morphology (shown in Figure 3.14). The microcapsules suspended in the (d) solution containing both TFA and LiCl showed the most shell wall erosion compared with other samples after 24 h treatment.

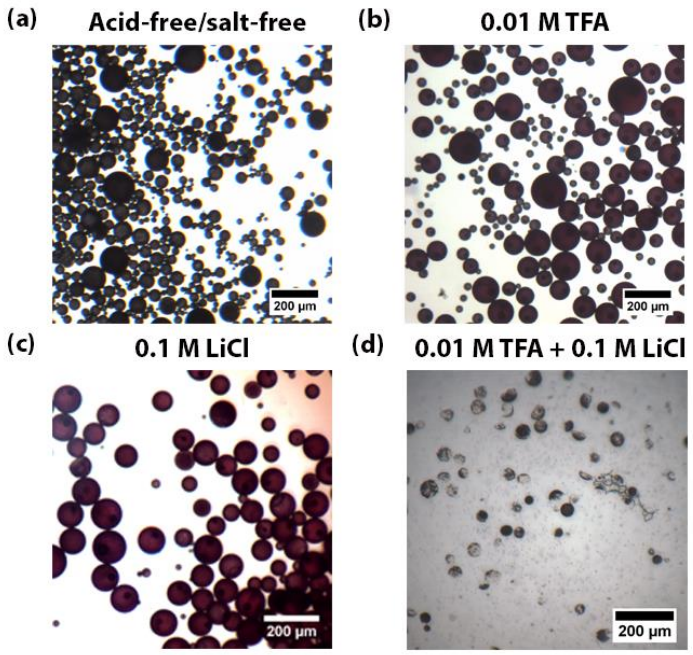

Figure 3.8. In situ optical microscopy images of cPPA microcapsules (M_n=58 kDa, ~5 mg/mL) suspended in different triggering solutions. Microcapsules were suspended in (a) methanol (acid-free salt-free), (b) 0.01 M TFA, (c) 0.1 M LiCl, and (d) 0.01 M TFA + 0.1 M LiCl. After 24 h treatment, the microcapsule's suspensions were imaged under an optical microscope. Microcapsules suspended in (a)-(c) solutions showed no depolymerization and identical morphologies. The microcapsules suspended in (d) solution containing both TFA and LiCl showed the most shell wall erosion compared with other samples after 24 h treatment.

3.3 ION CO-ACTIVATION EFFECT OF LICL IN ALTERNATIVE ACID SOLUTIONS

We further verified the co-activation effect of LiCl in alternative acid solutions: HCl and *p*-toluene sulfonic acid (PTSA) (Figure 3.9, Table 3.1, Figure 3.10). The addition of LiCl (1 M) reduced t_{D50} from >24 h to 5.3 ± 0.5 h for 1 mM HCl (Figure 3.9a) and to 6.9 ± 1.2 h for 1 mM PTSA (Figure 3.9b). Similarly, we analyzed the depolymerization mol % at 4 h in varied concentrations of acids and LiCl (Figure 3.9c-d). A synergistic effect was confirmed in both HCl and PTSA, resulting in accelerated cPPA depolymerization rates dependent on the LiCl and acid concentrations. These results validated that the LiCl co-activation effect was applicable to different acidic solutions. We have also examined microcapsules prepared with a lower

molecular weight of cPPA as the shell wall (M_n=42 kDa, PDI=1.6) in varied concentrations of acids and LiCl (Figure 3.10). Decreasing the molecular weight of cPPA from 58 kDa to 42 kDa, in both HCl and PTSA (at 4 h), the depolymerization maps showed the migration of blue color (≥ 90 mol % depolymerization) to the lower left side of the maps. This indicates that microcapsule's shell walls consisting of cPPA with a lower molecular weight depolymerized faster than those consisting of cPPA with a higher molecular weight.

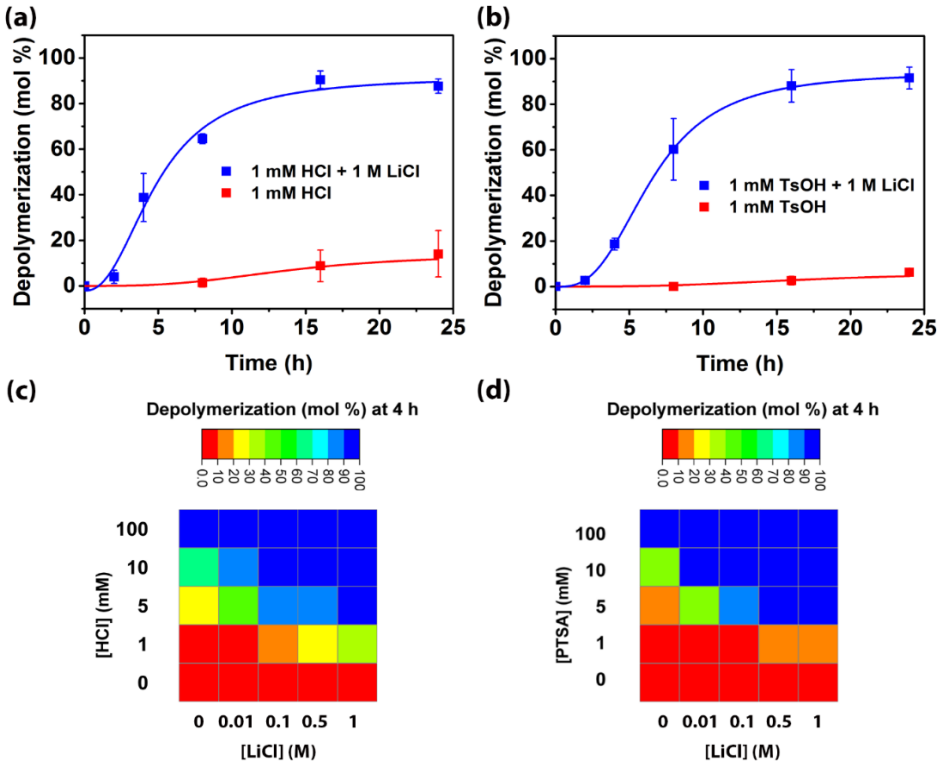

Figure 3.9. Depolymerization profiles of cPPA microcapsules suspended in different triggering solutions over 24 h and summary of depolymerization mol % in varied concentrations of acids and LiCl at 4 h. (a) Shell wall depolymerization profiles of cPPA microcapsules (M_n=58 kDa, ~5 mg/mL) suspended in 1 mM HCl (red) and 1 mM HCl +1 M LiCl (blue) in solvent methanol-d_4. (b) Shell wall depolymerization profiles of cPPA microcapsules (M_n=58 kDa, ~5 mg/mL) suspended in 1 mM PTSA (red) and 1 mM PTSA +1 M LiCl (blue) in solvent methanol-d_4. (c) Depolymerization mol% of cPPA microcapsules suspended in varied concentrations of HCl and LiCl at 4 h. (d) Depolymerization mol% of cPPA microcapsules suspended in varied concentrations of PTSA and LiCl at 4 h. Depolymerization (mol %) was measured by NMR using ethylene glycol (~5 mg/mL) as an internal standard. Data plots were fitted with an empirical

Figure 3.9. (cont.) logarithmic function (quantification procedures were detailed in 3.5.4). Error bars represent standard deviation of three experiments.

Table 3.1. Summary of Depolymerization Half-life in Alternative Acids

Acid Concentration*	pH Meter Value	Apparent pH Value	Depolymerization at 24 h (mol %)	Shell Wall Half-Life (h)
1 mM HCl	-0.147	4	14.1±10.2	>24
1 mM HCl+1 M LiCl	0.174	4	87.6±3.2	5.3 ± 0.5
1 mM TsOH	-0.063	4	6.3±1.6	>24
1 mM TsOH+1 M LiCl	0.059	4	91.5±4.8	6.9 ±1.2

**Solvent: methanol-d_4*

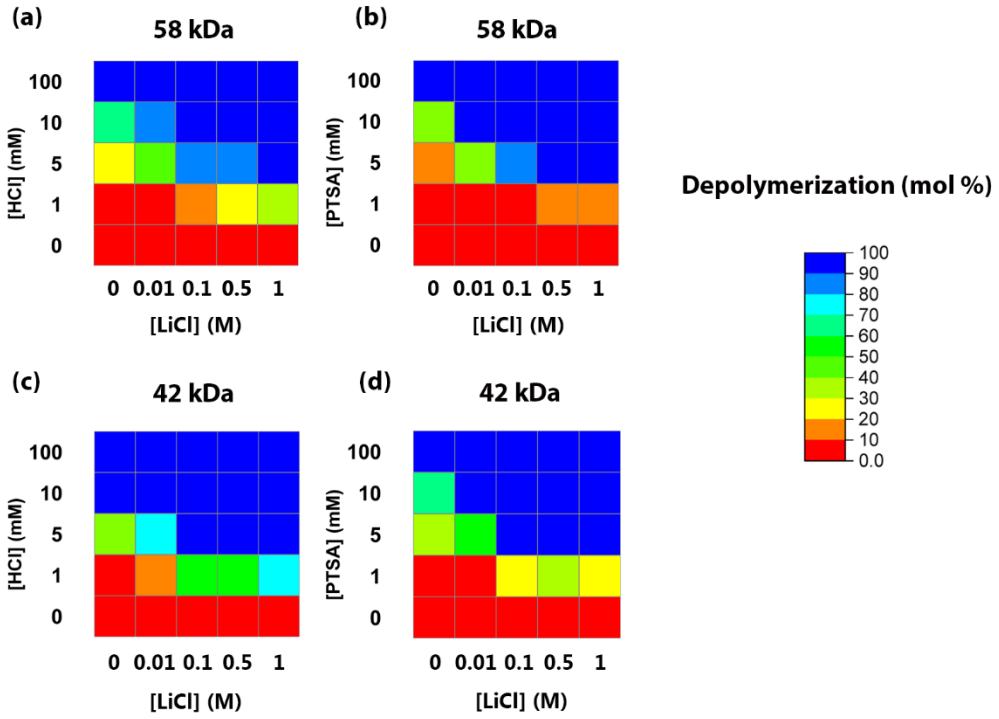

Figure 3.10. Effect of cPPA microcapsule's shell wall molecular weight on depolymerization rates in varied concentrations of acids and LiCl, solvent: methanol-d_4. Summary of depolymerization mol % at 4 h of microcapsules (~5 mg/mL) prepared by (a) 58 kDa cPPA and (c) 42 kDa cPPA in varied concentrations of HCl and LiCl. Summary of depolymerization (mol.

Figure 3.10. (cont.) %) at 4 h in microcapsules prepared by (b) 58 kDa cPPA and (d) 42 kDa cPPA in varied concentrations of PTSA and LiCl. Depolymerization (mol %) was measured by NMR using ethylene glycol (~5 mg/mL) as an internal standard.

3.4 CONTROL EXPERIMENTS TO VALIDATE THE CO-ACTIVATION EFFECT OF LICL

3.4.1 Acid Concentration Determined by Titration

To exclude the possibility that the accelerated depolymerization rates were attributed to generating extra acids from decomposition and/or hydrolysis of the ionic compounds, we performed titration experiments to quantify the acid concentrations in different triggering solutions (Table 3.2). The titration results suggested that compared to solution 1 (0.01 M TFA, salt-free), solution 3 or solution 4 (0.01 M TFA, different concentrations of salts) had approximately the same acid concentration. Therefore, the co-activation effect of LiCl and the accelerated depolymerization rates were not induced by generating extra acids.

Table 3.2. Summary of Titration Results

Solutions	Calculated Acid (mmol/L)	Apparent pH value	Depolymerization at 24 h (mol %)
0.01 M TFA	2.50	3	0
0.03 M TFA	9.38	3	0
0.01 M TFA + 0.1 M LiCl	2.76	3	100.4±4.0
0.01 M TFA+1 M LiCl	2.50	3	89.5±4.8
1 M LiCl	0.05	6	0

**Solvent: methanol-d_4*

3.4.2 Depolymerization Profiles in Different Concentrations of TFA

Acid-triggered cPPA depolymerization profiles was measured by suspending the cPPA microcapsules in different concentrations of TFA/methanol solutions. The depolymerization

profiles were measured by NMR using ethylene glycol (~5 mg/mL) as an internal standard. (Figure 3.11). As expected, in acid triggered depolymerization, an acid concentration-dependent depolymerization rate was observed. Since a higher acid concentration resulted in a lower pH value, the depolymerization was inverse to the pH values of the solutions. Complete depolymerization was achieved in 0.5 M TFA in methanol-d_4 within 48 h (black trace). Compared with co-activated samples in 0.01 M TFA + 1 M LiCl solution in Figure 3.4 (pH = -0.549, t_{D50}=6.0 ± 0.5 h), the depolymerization kinetics in 0.5 M TFA (pH = -0.950, t_{D50}=12.2 ± 0.3 h) was slower despite the solution has a lower pH value. This indicated that the depolymerization kinetics in ion/acid mixed solutions was not pH or acid concentration-dependent. Thus, acid was not the only driving force for cPPA depolymerization, supporting the co-activation effect of LiCl.

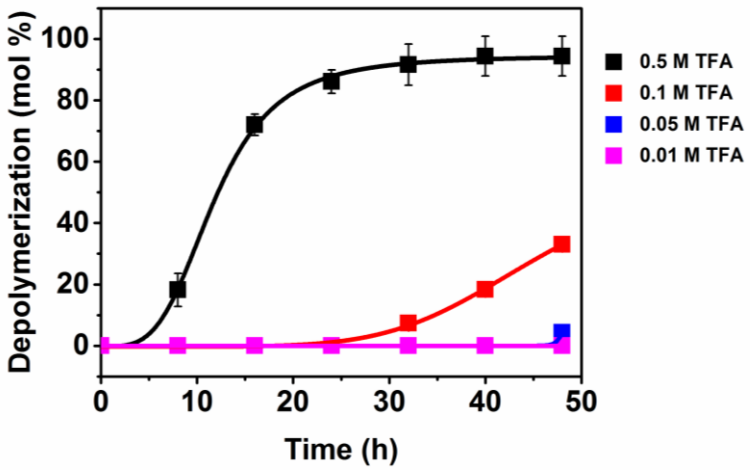

Figure 3.11. Shell wall depolymerization profiles of cPPA microcapsules (M_n=58 kDa, ~5 mg/mL) suspended in various concentrations of TFA/methanol-d_4 solutions measured by NMR using ethylene glycol (~5 mg/mL) as an internal standard: 0.01 M TFA (pink), 0.05 M TFA (blue), 0.1 M TFA (red), and 0.5 M TFA (black). Data plots were fitted with an empirical logarithmic function (quantification procedures were detailed in 3.5.4). Error bars represent standard deviation of three experiments.

Table 3.3. Summary of Depolymerization Half-Life in Different Concentration of TFA

Acid Concentration	pH Value	Apparent pH Value	Depolymerization at 24 h (mol %)	Shell Wall Half-Life (h)
0.5M TFA	-0.950	1	86.1 ± 3.8	12.2 ± 0.3
0.1M TFA	-0.628	2	0	>48
0.05M TFA	-0.472	3	0	>48
0.01M TFA	-0.035	3	0	>48

**Solvent: methanol-d_4*

3.4.3 Effect of Water on Depolymerization Rates

To exclude the possibility that the accelerated depolymerization rates were caused by hygroscopy of salts, we studied the effect of water in the depolymerization kinetics as shown in Figure 3.12. Depolymerization profiles in solutions containing 0.01 M TFA doped with 2 M H_2O (black trace) or 1 M H_2O (blue trace) were compared with depolymerization profiles in 0.01 M TFA. In these depolymerization studies, less than 5 mol % depolymerization was observed after 48 h. This indicated that the adventitious water did not significantly altered the depolymerization rate. Therefore, the co-activation effect was not attributed to the hygroscopy of salts.

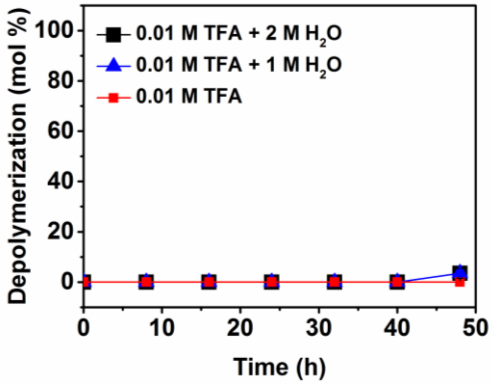

Figure 3.12. Shell wall depolymerization profiles of cPPA microcapsules (M_n=58 kDa, ~5mg/mL) suspended in 0.01 M TFA/methanol-d_4 solutions doped with 2 M H_2O (black), 1 M

Figure 3.12. (cont.) H_2O (blue), and no H_2O. The lines were drawn to facilitate visualization. Error bars represent standard deviation of three experiments and were hidden within the data plots.

3.4.4 Co-Activation Effect in Water

To demonstrate the co-activation effect in aqueous solutions, we performed depolymerization analysis using D_2O as the solvent. Because the microcapsules float in aqueous solutions, we used cPPA film samples in this study and taped the films at the bottom of glass vials for this experiment. The cPPA films were produced by solvent casting using a cPPA/DCM solution (60 mg/mL, M_n = 109 kDa, PDI=1.7). cPPA of a higher molecular weight was used for preparing free standing films, The depolymerizaton mol % in varied concentrations of acids and salt solutions was summarized in Figure 3.13. Similarly, the depolymerization rate was accelerated in the presence of both HCl and LiCl and resulted in more depolymerization mol % than individual HCl or LiCl solutions of the same concentration.

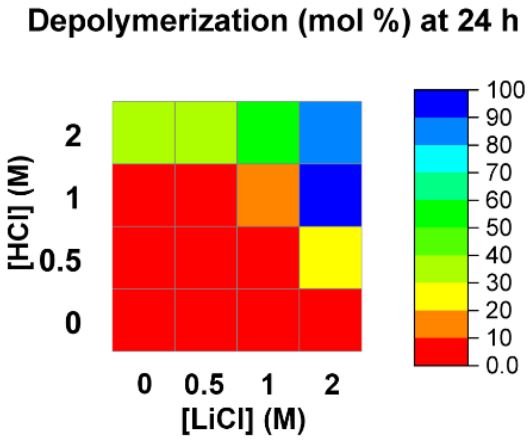

Figure 3.13. Summary of depolymerization mol % at 24 h of cPPA films (M_n=109kDa, PDI=1.7, 3 mg/mL) immersed in varied concentrations of HCl and LiCl in D_2O. Depolymerization mol % was measured by NMR using ethylene glycol (~6 mg/mL) as an internal standard. The

Figure 3.13. (cont.) depolymerization products were cis- and trans- isomers of 1,3-dihydro-1,3-dihydroxyisobenzofuran and o-PA, and the depolymerization products were quantified by integrating the depolymerization products' aromatic peaks against the internal standard's peaks.

3.5 EXPERIMENTAL DETAILS

3.5.1 Materials and Instrumentations

Unless otherwise noted, all chemicals were obtained from Sigma Aldrich and used as received. The monomer *o*-PA (98%, Alfa-Aesar) was purified by hot filtration followed by a single recrystallization according to a literature procedure.[13] DCM was obtained from an anhydrous solvent delivery system equipped with activated alumina columns. All glassware for polymerization was oven dried prior to use. The synthesis of cPPA (M_n=42~109kDa, PDI=1.6~1.7) followed previous literature procedures with minor modifications.[14]

^{1}H NMR spectra were recorded using a Bruker 500 MHz spectrometer with broad-band CryoProbe and automation. Chemical shifts were reported in δ (ppm) relative to the residual solvent peak CHD_2OD-d_4 (3.31 ppm), $CHDCl_2$-d_2 (5.32 ppm) or HDO (4.75 ppm). ^{13}C NMR spectra were measured in methanol-d_4 and chemical shifts were reported in δ (ppm) relative to the signals for the solvent (49.00 ppm). Analytical gel permeation chromatograph (GPC) analyses were performed with a Waters1515 Isocratic HPLC pump, a Waters (2998) Photodiode Array Detector, a Waters (2414) Refractive Index Detector, a Waters (2707) 96-well autosampler, and a series of 4 Waters HR Styragel 3wcolumns (7.8 x 300mm, HR1, HR3, HR4, and HR5) in THF at 30 °C. The GPC was calibrated using monodisperse polystyrene standards. Fluorescence intensities were measured by a HORIBA Fluoromax-4 fluorescence spectrometer. Visualization of microcapsule morphology was performed on a Leica DMR optical microscope (fluorescence mode) and a Hitachi S-4700 scanning electron microscopy (SEM) with a Oxford

Instruments ISIS EDS X-ray Microanalysis System. Before SEM imaging, samples were sputter-coated with Au/Pd for 60 s to eliminate surface charging effects. Titration experiments were performed using 0.05 M potassium hydroxide (KOH) in methanol as the standard solution. pH indicator was bromocresol purple. pH measurements for solutions used a pH meter (Metrohm 827 pH lab) equipped with a H^+ Ion Selective Electrode (ISE). The electrode was calibrated using buffers pH = 4 and pH = 7. Apparent pH values were measured by pH paper. Zeta potential measurements were performed with an Anton Paar Litesizer 500 using cPPA nanoparticles, because the cPPA nanoparticles formed much more stable dispersion in salt/methanol solutions compared with cPPA microcapsules. The cPPA nanoparticles dispersion was left still for 0.5 h before the upper dispersions were collected and injected into a measurement cuvette. For each sample, at least three measurements were run. All data fitting and data normalization in this study was conducted in OriginPro 2016.

3.5.2 cPPA Microcapsule's Preparation and Characterization

cPPA microcapsules were fabricated by bulk emulsification followed by rapid solvent evaporation as described in Chapter 2.[12] In brief, a homogeneous mixture of cPPA (shell wall, M_n=58 kDa or 42 kDa), JJB (core), and DCM ($m_{cPPA}/m_{JJB}/m_{DCM}$=1/0.75/13.26) was prepared. Nile red was added in the solution to aid visualization and release profile measurements. The mixture was added dropwise into a 1 wt % poly (vinyl alcohol) (PVA) solution under 400 rpm agitation. The container was capped and an oil-in-water (O/W) emulsion was stirred for another 10 min. The emulsion was then poured into 100 mL of 1 wt % PVA solution in a 500 mL round bottom flask, immediately followed by rapid solvent evaporation for 1 h at reduced pressure. The resulting microcapsules were filtered and cleaned by washing with 500 mL deionized water and 100 mL heptane. The microcapsules were dried in open air for another 24 h.

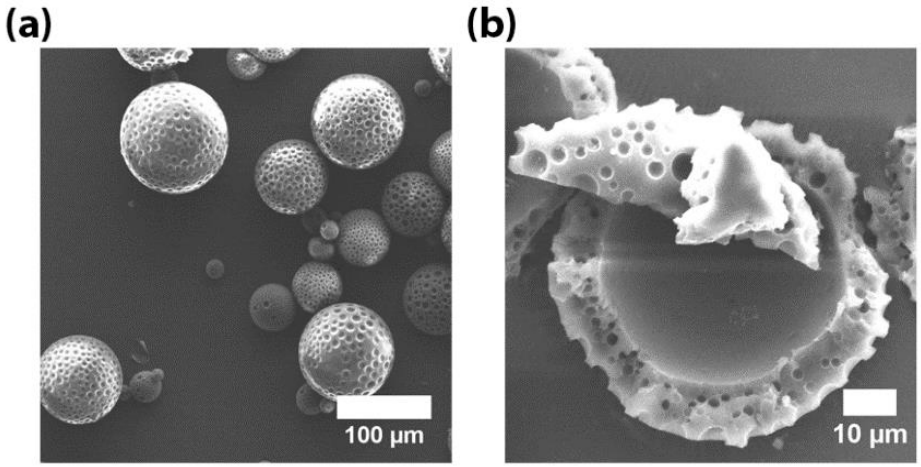

Figure 3.14. SEM images of the as-synthesized cPPA microcapsules (M_n=58 kDa) prepared by bulk emulsification with the composition $m_{cPPA}/m_{JJB}/m_{DCM}$=1/0.75/13.26 and rapid solvent evaporation procedure as detailed in Chapter 2, 2.6.3. (a) Intact microcapsules showed exterior shell wall morphologies with golf-ball like surface. (b) Manually crushed microcapsules showed the cross sectional shell wall morphologies and the approximate shell wall thickness is 10 µm. The cross-sectional image also showed that the surface dimple structures did not penetrate the shell walls.

3.5.3 cPPA Nanoparticle's Preparation and Characterization

cPPA nanoparticles were prepared for zeta potential measurements. cPPA nanoparticles were fabricated by bulk emulsification followed by rapid solvent evaporation procedure. A solution of cPPA in DCM (m_{cPPA}/m_{DCM} = 1/13.26) was prepared as the oil phase. Nile red was added in the oil mixture to aid visualization. The oil mixture was added into a 1 wt % PVA solution. Volume ratio of the organic phase to the aqueous phase (PVA) was 1:5. After mixing, an O/W emulsion was generated by sonication for 10 s (SONICS, Vibra-Cell, VC 505, Ultrasonic Liquid Processor, 500 Watt, 20 kHz, Pulse 5 s, amplitude 35%). Immediately after the emulsification, the emulsion was poured into 100 mL 1 wt % PVA solution in a 500 mL round bottom flask, followed by rapid solvent evaporation for 1 h at reduced pressure. The nanoparticles were cleaned by 5 times of centrifugation and re-dispersion in methanol.

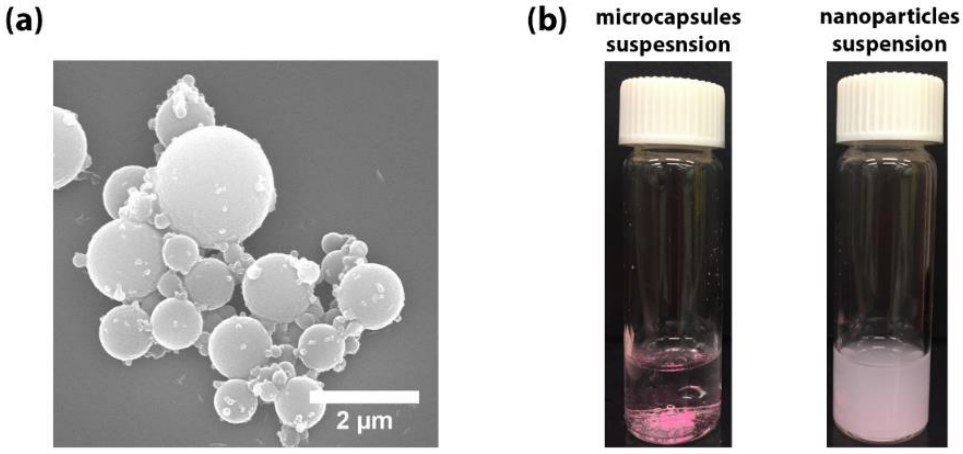

Figure 3.15. SEM images of cPPA nanoparticles and digital images of cPPA microcapsules and nanoparticles suspensions in methanol. (a) cPPA nanoparticle's morphology. (b) cPPA microcapsule (~5 mg/mL) and nanoparticle (~1 mg/mL) suspension in methanol for zeta potential measurements. Nanoparticles formed a stable dispersion in methanol within 30 min, allowing enough time for zeta potential measurements.

3.5.4 General Quantification Methods for Depolymerization Profiles

Depolymerization profiles were measured by NMR used ethylene glycol (~5 mg/mL) as the internal standard because it has high boiling point (197.3 °C) and is miscible with the solvent methanol-d_4. Microcapsules (~5 mg) and ethylene glycol (~5 mg) were accurately weighed into a glass vial and 1 mL methanol-d_4 triggering solutions (only salts, only TFA, salts and TFA) were added to form microcapsule suspensions. The sample vials were kept still and all microcapsules sank to the bottom within 10 min. At designated time, 0.1 mL aliquot (supernatant solution) was collected and diluted with 0.6 mL methanol-d_4 for NMR measurements. At each time point, the molar amount of the depolymerization products in the aliquot, $M^{i}_{monomer}$ (i is the number of collected time points, $i = 0,\ 1,\ 2,\ \ldots$), was determined by integrating the depolymerization products aromatic peaks (7.30-7.60 ppm, 4 H) against the internal standard peaks (3.60-3.65 ppm, 4 H). To obtain microcapsules depolymerization profiles, cumulative depolymerization mol

% was plotted vs. time. The cumulative depolymerization mol % at time *t* (h) was calculated based on the equation below,

$$Depolymerization\ mol\ \% = \frac{M^{i}_{monomer} \times (10 - i) + \sum_{0}^{i-1} M^{i}_{monomer}}{M_{polymer}} \times 100\% \qquad 3.1$$

where $M_{polymer}$ is the molar amount of shell wall cPPA in the cPPA microcapsules. To obtain $M_{polymer}$, we dissolved the cPPA microcapsules and the internal standard ethylene glycol in CD_2Cl_2-d_2. The $M_{polymer}$ is calculated by integrating shell wall cPPA polymer aromatic peaks (7.20-7.80 ppm, 4 H) over the internal standard peaks (3.60-3.70 ppm, 4 H) in the NMR spectra. The depolymerization profiles were fitted by an empirical logarithmic function as shown below,[11]

$$D = \frac{D_0 - D_f}{1 + (\frac{t}{t'_{D_{50}}})^n} + D_f \qquad 3.2$$

where D_0 is the depolymerization mol % at t = 0 h, D_f is the depolymerization mol % at t = 48 h, and n is order exponent. $t'_{D_{50}}$ is the apparent depolymerization half-life, corresponding to where $D = \frac{D_f - D_0}{2}$. When D_f < 100 %, the $t'_{D_{50}}$ does not accurately reflect the actual depolymerization half-life (D = 50). Therefore, we defined and used the actual depolymerization half-life ($t_{D_{50}}$). $t_{D_{50}}$ is the t value corresponds to D = 50. The $t_{D_{50}}$ value is determined from the logarithmic function fitting curves. A smaller $t_{D_{50}}$ value indicates a faster depolymerization rate. The results were reported based on the average of at least three independent experiments.

3.5.5 NMR Spectra

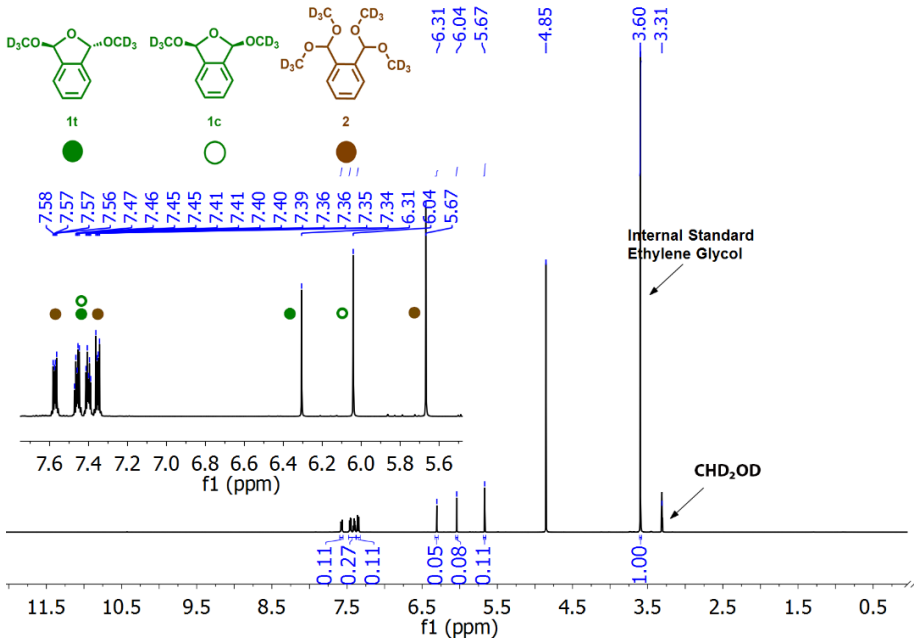

Figure 3.16. ^{1}H NMR spectrum of purified o-PA dissolved in 0.01 M TFA/methanol-d_4.

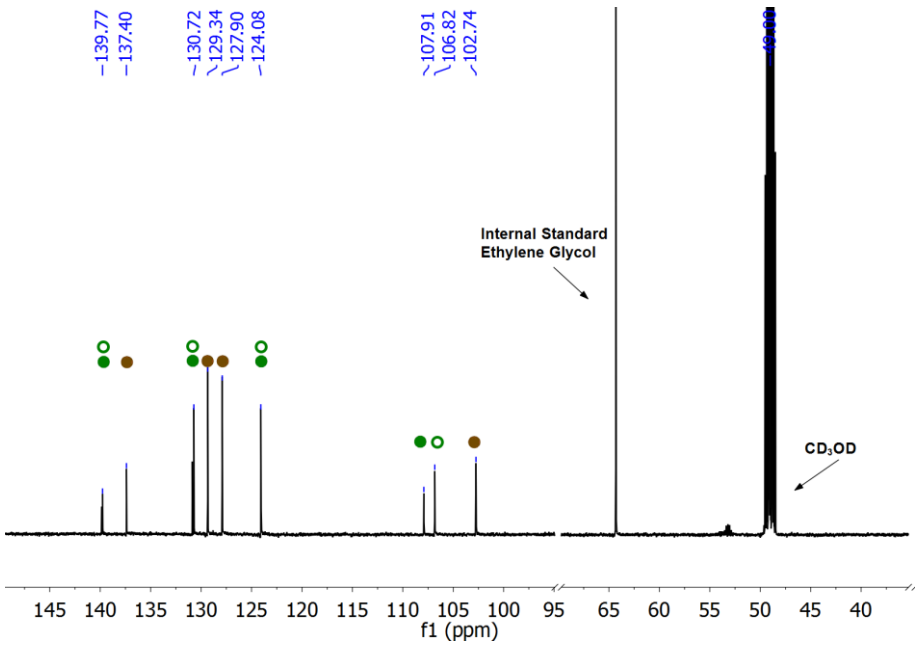

Figure 3.17. ^{13}C NMR spectrum of purified o-PA dissolved in 0.01 M TFA/methanol-d_4.

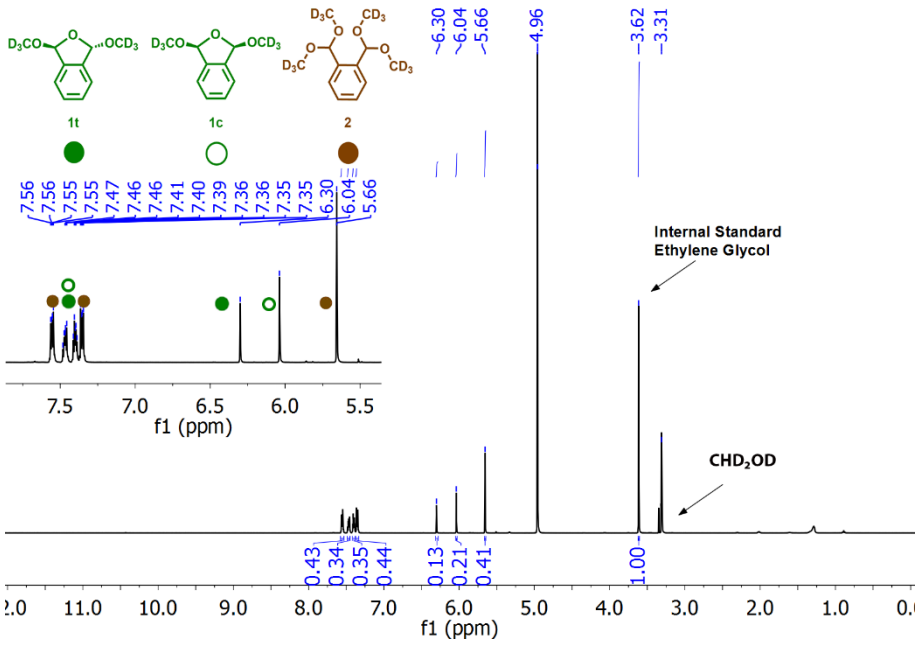

Figure 3.18. Representative ^{1}H NMR spectrum of microcapsules suspended in 1 M LiCl + 0.01 M TFA in methanol-d_4 after 24h.

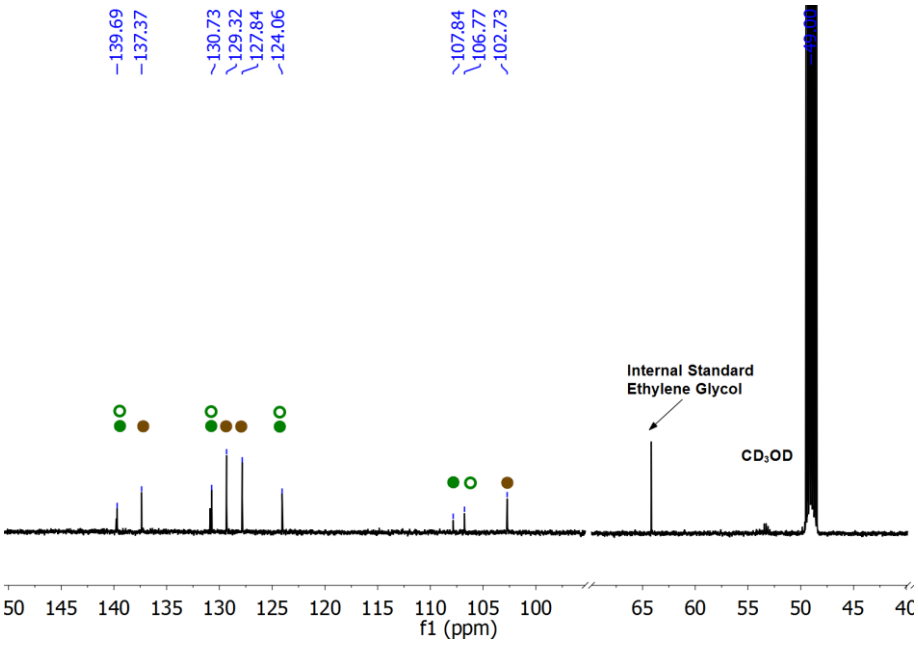

Figure 3.19. Representative ^{13}C NMR spectrum of microcapsules suspended in 1 M LiCl + 0.01 M TFA in methanol-d_4 after 24 h.

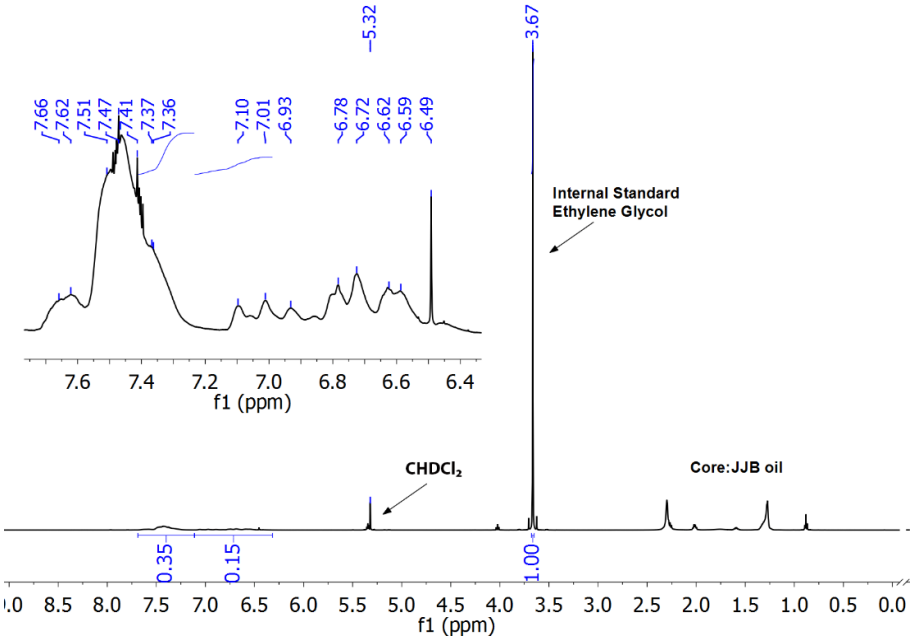

Figure 3.20. Representative ^{1}H NMR spectrum of microcapsules dissolved in CD_2Cl_2 to calculate the molar amount of shell wall cPPA in the microcapsules.

3.6 REFERENCES

Notes: This chapter is a collaborative work with Liuyan Tang, Dr. Xiaocun Lu, and Huiying Liu. S.T. authored the text, performed cPPA synthesis, prepared microcapsules, characterized materials (NMR, SEM, release profiles) and analyzed the results. Liuyan Tang worked with S.T. in NMR, pH, release profiles measurements and titration. Dr. Xiaocun Lu and Huiying Liu worked with S.T. in NMR and results analysis. This chapter has previously been published in the following reference: **Tang, S.**; Tang, L.; Lu, X.; Liu, H.; Moore, J. S., "Programmable Payload Release Triggered by a Specific Ion Co-activation Effect", *J. Am. Chem. Soc.* **2018**, *140*, 94-97. **DOI:** 10.1021/jacs.7b11022. The materials are reproduced/adapted with permission.

(1) Douglas, S. M.; Bachelet, I.; Church, G. M. A Logic-Gated Nanorobot for Targeted Transport of Molecular Payloads. *Science* **2012**, *335*, 831–834.

(2) White, S. R.; Geubelle, P. H. Self-Healing Materials: Get Ready for Repair-and-Go. *Nat. Nanotechnol.* **2010**, *5*, 247–248.

(3) Hutchins, K. M.; Sekerak, N. M.; Moore, J. S. Polymerization Initiated by Particle Contact: A Quiescent State Trigger for Materials Synthesis. *J. Am. Chem. Soc.* **2016**, *138*, 12336–12339.

(4) Grzybowski, B. A.; Huck, W. T. S. The Nanotechnology of Life-Inspired Systems. *Nat. Nanotechnol.* **2016**, *11*, 585–592.

(5) Epstein, I. R.; Xu, B. Reaction–diffusion Processes at the Nano- and Microscales. *Nat. Nanotechnol.* **2016**, *11*, 312–319.

(6) Goehring, N. W.; Grill, S. W. Cell Polarity: Mechanochemical Patterning. *Trends Cell Biol.* **2013**, *23*, 72–80.

(7) White, S. R.; Moore, J. S.; Sottos, N. R.; Krull, B. P.; Santa Cruz, W. A.; Gergely, R. C. R. Restoration of Large Damage Volumes in Polymers. *Science* **2014**, *344*, 620–623.

(8) Tsuda, M.; Hata, M.; Nishida, R.; Oikawa, S. Acid-Catalyzed Degradation Mechanism of Poly(phthalaldehyde): Unzipping Reaction of Chemical Amplification Resist. *J.Polym. Sci., Part A Polym. Chem.* **1997**, *35*, 77–89.

(9) Schwartz, J. M.; Phillips, O.; Engler, A.; Sutlief, A.; Lee, J.; Kohl, P. A. Stable, High-Molecular-Weight Poly(phthalaldehyde). *J. Polym. Sci. Part A Polym. Chem.* **2017**, *55*, 1166–1172.

(10) Mirsadeghil, S.; Rickborn, B. 1-Methoxyisobenzofuran from Base-Induced and Acid-Catalyzed Reactions of 1,3-Dihydro-1,3-Dimethoxyisobenzofura. *J. Org. Chem.* **1987**, *52*, 787–792.

(11) Seefeldt, S. S.; Jensen, J. E.; Fuerst, E. P. Log-Logistic Analysis of Herbicide Dose-Response Relationships. *Weed Technol.* **1995**, *9*, 218–227.

(12) Tang, S.; Yourdkhani, M.; Casey, C. M. P.; Sottos, N. R.; White, S. R.; Moore, J. S. Low-Ceiling-Temperature Polymer Microcapsules with Hydrophobic Payloads via Rapid Emulsion-Solvent Evaporation. *ACS Appl. Mater. Interfaces* **2017**, *9*, 20115–20123.

(13) DiLauro, A. M.; Robbins, J. S.; Phillips, S. T. Reproducible and Scalable Synthesis of End-Cap-Functionalized Depolymerizable Poly(phthalaldehydes). *Macromolecules* **2013**, *46*, 2963–2968.

(14) Kaitz, J. A.; Diesendruck, C. E.; Moore, J. S. End Group Characterization of Poly(phthalaldehyde): Surprising Discovery of a Reversible, Cationic Macrocyclization Mechanism. *J. Am. Chem. Soc.* **2013**, *135*, 12755–12761.

CHAPTER 4 : PROGRAMMABLE PAYLOAD RELEASE TRIGGERED BY A SPECIFIC ION CO-ACTIVATION EFFECT

4.1 INTRODUCTION

In biological systems, homeostasis depends on accurate and autonomous regulation leading to intricate, feedback-controlled reaction networks. Some feedback controlled mechanisms originate from specific ion-biomolecule interactions that regulate enzyme (de)activation,[1] signal transduction,[2–4] and cell volume.[5] For example, Ca^{2+} inhibits lipid recognition by direct binding to the lipid marker phosphatidylinositol 4,5-bisphosphate in plasma membranes, whereas Mg^{2+} exhibits only a modest inhibition.[6] This specific ion-biomolecule interaction is mostly attributed to different ion dehydration energy penalties originally studied by Hofmeister in the 1880s.[7,8] So far, the specific ion effect has been applied to (bio)catalysis,[9] protein aggregation,[10–14] thermoresponsive materials phase transitions,[12,15,16] colloidal systems stability,[17,18] and molecular mechanisms of ion-enzyme binding.[19–22]

In contrast, the specific ion effect has been less commonly employed in synthetic materials but has potential in the design of materials with bio-inspired autonomous regulation. For example, combining a specific ion effect with compartmentalized materials, microcapsules[23] and vascularized composites,[24] may achieve biomimetic functions such as signal transduction and chemical amplification. One strategy involves ion-triggered microcapsules that transduce ion recognition into the release of an encapsulated payload. Microcapsules whose shell walls consist of transient polymers are a promising possibility.[25–27] Typically, the transient polymers undergo chain unzipping depolymerization after removing end groups or cleaving the backbone by

stimuli.[26,28] In Chapter 2, we have shown that the depolymerization of transient polymers leads to the rupture of the cPPA microcapsule's shell wall, releasing the payloads with sigmoidal shaped kinetic profiles.[29] In Chapter 3, we have used LiCl to demonstrate the ion co-activation effect at the solid/liquid interfaces of transient polymer microcapsule's suspensions. This ion co-activation effect transduced ion-polymer interactions to tunable depolymerization rates. In this Chapter, we investigated the ion specificity in the co-activation effect to understand the criteria for cations and anions to control the cPPA depolymerization rates. An established ion library will be beneficial for controlled depolymerization kinetics that allows programmable payload release triggered by specific ions in the solutions. Also, specific ion effects at the interfaces of transient polymer microcapsules are possible design components for feedback controlled reaction cascades. To our knowledge, the specific ion effect on transient polymers has not been addressed in previous studies.

4.2 ION SPECIFICITY IN THE CO-ACTIVATION EFFECT

4.2.1 Depolymerization Rates Modulated by Hofmeister Anions

To demonstrate ion specificity, we investigated the depolymerization profiles for various anions and cations. First, we varied the anions using lithium as the counter cation (0.01 M TFA + 1 M lithium salts) (Figure 4.1). Different anions showed distinct co-activation effects, primarily depending on the solvation behavior of anions. For the kosmotropic anions such as SO_4^{2-}, OAc^-, and F^-, no co-activation effect was observed, evidenced by their lack of depolymerization mol % at 48 h (0 mol %) compared to depolymerization mol % in 0.01 M TFA (salt-free) at 48 h (0 mol %) (Figure 4.1).

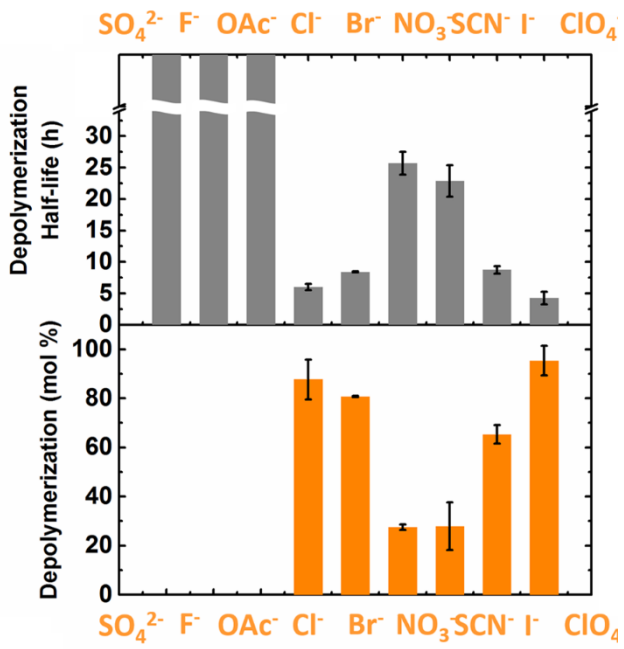

Figure 4.1. Anion co-activation effects on cPPA microcapsule's depolymerization rates. cPPA microcapsules (M_n=58 kDa, ~5 mg/mL) were suspended in methanol-d_4 containing 0.01 M TFA + 1 M lithium salts with different anions. The co-activation effect of each anion species was represented by depolymerization half-life t_{D50} and depolymerization mol % at 16 h. Both values were obtained from depolymerization profiles in different lithium salts/TFA/methanol-d_4 solutions, shown in Figure 4.12 and Figure 4.13. A lower half-life value or a higher depolymerization mol % value indicated a faster depolymerization rate and an increased co-activation effect. The depolymerization half-life t_{D50} of SO_4^{2-}, OAc^-, and F^- were marked in break columns because these values exceeded the measuring scale. Among these examined anions, only chaotropic anions accelerated the depolymerization rates. Note: Li_2SO_4 and LiF saturated solutions were used.

For chaotropic anions, the depolymerization half-life t_{D50} was ClO_4^- (4.2 ± 1.0 h) < Cl^- (6.0 ± 0.5 h) < Br^- (8.4 ± 0.1 h) < I^- (8.8 ± 0.6 h) < SCN^- (22.9 ± 2.5 h) < NO_3^- (25.7 ± 1.8 h), showing distinct co-activation effects. To further validate the anion specificity, an *in situ* ion exchange experiment was designed (Figure 4.2). Microcapsules were first suspended in 0.01 M TFA for 24 h (0 mol % depolymerization), followed by adding 0.05 M LiCl to accelerate the depolymerization from 24 to 42 h. At 42 h, 0.05 M AgOAc was added to exchange Cl^- to OAc^-

by forming AgCl. The removal of the chaotropic anion Cl^- from solutions slowed down the depolymerization from 42 to 72 h. This abrupt change in the co-activation behavior at the borderline from kosmotropic anions to chaotropic anions is an indication of the Hofmeister effect, that originated from the difference in anion solvation behavior (Table 4.1).[12] The desolvation energy penalties of chaotropic anions are much lower than those of kosmotropic anions. Therefore, the interactions between chaotropic anions and cPPA were more energetically favorable to co-activate the depolymerization.[30]

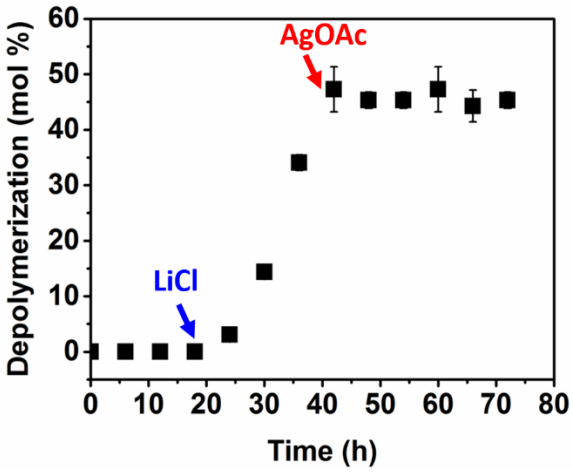

Figure 4.2. In situ depolymerization experiments of cPPA microcapsules (M_n=58 kDa, ~5 mg/mL) suspended in methanol-d_4. From 0 h to 24 h, microcapsules were suspended in 0.01 M TFA, which resulted in 0 mol % depolymerization at 24 h. LiCl was added to the solutions in situ at 24 h to from 0.01 M TFA + 0.05 M LiCl solution and accelerated the depolymerization rates from 24 to 42 h. At 42 h, AgOAc was added to the solutions in situ to form 0.01 M TFA + 0.05 M LiOAc + 0.05 M AgCl solutions, and AgCl precipitated immediately in the solutions. The removal of the chaotropic anion Cl^- from solutions slowed down the depolymerization rates from 42 to 72 h.

Table 4.1.Thermodynamic Data of Hofmeister Anions in the Literature[30]

Anions	ΔG_{hyr} (kJ/mol)	$\Delta G_{tr\ (MeOH)}$ (kJ/mol)
SO_4^{2-}	-1090	31
F^-	-472	16
OAc^-	-373	16
Cl^-	-347	13
Br^-	-321	11
NO_3^-	-306	13
SCN^-	-287	6
I^-	-283	7
ClO_4^-	-214	6

4.2.2 Depolymerization Rates Modulated by Hofmeister Cations

Intrigued by the connection of anion specificity to the Hofmeister series, we further tested the cation effect using chloride (0.01 M TFA + 0.02 M chloride salts) as the counter anion (Figure 4.3). A lower concentration (0.02 M chloride salts) of co-activators were employed to ensure solubility of all chloride salts. Compared with the anion specific studies, the cation specific studies showed modest difference in the co-activation effects: Li^+ (16.7 ± 0.9 h) < Na^+ (16.9 ± 1.3) < NH_4^+ (18.5 ± 0.3 h) < K^+ (21.3 ± 1.2 h) < NMe_4^+ (22.4 ± 0.9 h). This indicates that anions are dominant factors in the co-activation behavior. The dominant role of anions over cations in the SICA effect is likely attributed to the stronger interaction of anions with the polymer/solvent interfaces compared with cations. In general, cations are smaller in size and more solvated compared with anions with similar molar mass, thereby cations are likely to be

depleted from a hydrophobic interface (cPPA shell wall) while anions are more attracted to it (Table 4.2).[10,20,31] Thus, the anion-cPPA interactions are more energetically favored than cation-cPPA interactions. The stronger interactions apparently led to the dominant role of anions in the SICA effect. Cations exhibit a secondary effect that modulates the co-activation inversely to the ion pair strength. A weaker ion pair allows a stronger anions-cPPA interaction and a stronger co-activation effect. More elaboration on this matter is in 4.2.3 and 4.2.4.

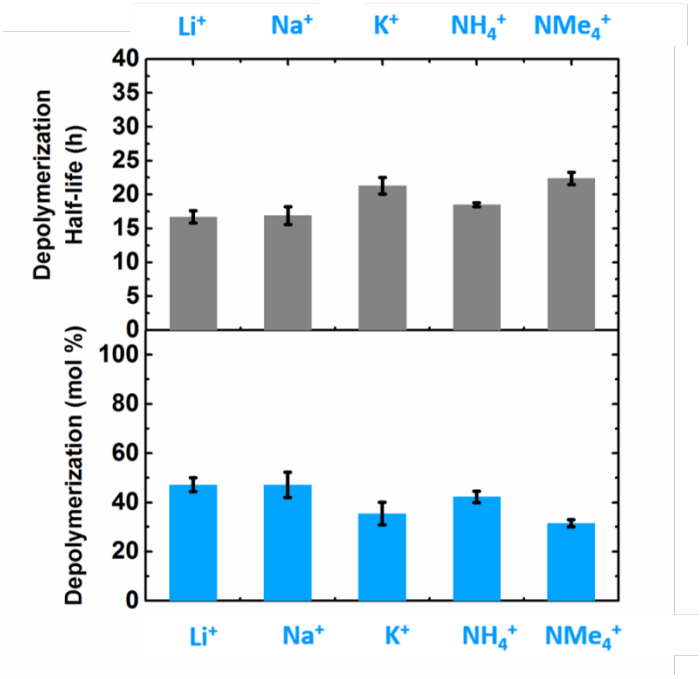

Figure 4.3. Cation co-activation effects on cPPA microcapsule's depolymerization rates. cPPA microcapsules (M_n=58 kDa, 5 mg/mL) were suspended in methanol-d_4 containing 0.01 M TFA + 0.02 M chloride salts with different cations. A low concentration (0.02 M) of co-activators was used to allow solubility of all chloride salts. The co-activation effect of each cation species was represented by depolymerization half-life t_{D50} and depolymerization mol % at 16 h. Both values were obtained from depolymerization profiles in different chloride salts/TFA/methanol-d_4 solutions, shown in Figure 4.14. A lower half-life value or a higher depolymerization mol % value indicated a faster depolymerization rate and an increased co-activation. Cations showed a modulating role in the co-activation and is correlated to the ion pair strength. The ion pair strength was estimated by the Law of Matching Water Affinities as specified in 4.2.3.[22,30,32]

Table 4.2.Thermodynamic Data of Hofmeister Cations in the Literature [30]

Anions	ΔG_{hyr} (kJ/mol)	$\Delta G_{tr\ (MeOH)}$ (kJ/mol)
Li^+	-481	4
Na^+	-375	8
K^+	-304	10
NH_4^+	-292	5
NMe_4^+	-175	6

4.2.3 Ion Pair and the Law of Water Matching Affinities

The Law of Water Matching Affinities (LWMA) are qualitative rules to represent ion pairing strength.[33,34] The affinity of cations and anions depends on the matching of their size and hydration properties. If the cations and anions have similar dimension and hydration properties, the formation of ion pairs are more energetically favorable. For example, LiF are stronger ion pairs compared with LiSCN, because Li^+ and F^- have similar sizes and hydration properties. Since the Hofmeister series are an ordering of cations and anions based on their hydration properties, the LWMA can be combined with the Hofmeister series to compare the ion pair strength as illustrated in Figure 4.4. When both cations and anions are kosmotropes or chaotropes (both on the left side or both on the right side), the hydration properties are similar and form solvent shared ion pairs (if both are kosmostropes) or contact ion pairs (if both are chaotropes) are energetically favorable. Alternatively, if cations are kosmotropes and anions are chaotropes (diagonal directions), *or vice versa*, the ion pairing effect is relatively weaker. Note: because the free energy of transfer (ΔG_{tr}) from water to methanol is small compared to the free energy of

hydration (ΔG_{hyr}) for all ions (Table 4.1, Table 4.2),[30] we assume the solvation behavior of ions in methanol were identical to their hydration behavior.

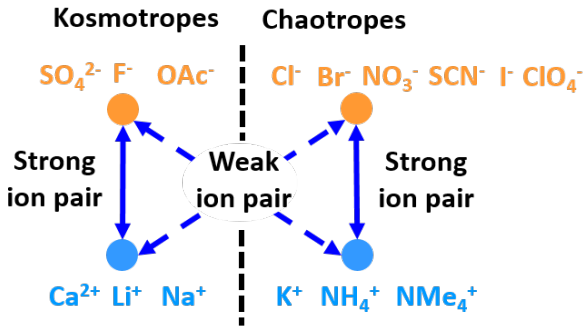

Figure 4.4. Illustration of ion pair strength determined by the combination of LWMA and the Hofmeister series. The cations and anions on the left side are kosmotropes (strongly solvated). The cations and anions on the right side are chaotropes (weakly solvated). When both cations and anions are kosmotropes or chaotropes (both on the left side or both on the right side), their hydration properties are similar and forming solvent shared ion pairs (if both are kosmostropes) or contact ion pairs (if both are chaotropes) are energetically favorable. Alternatively, if cations are kosmotropes and anions are chaotropes (diagonal directions), or vice versa, the ion pairing effect is relatively weaker. Note: because the free energy of transfer (ΔG_{tr}) from water to methanol is small compared to the free energy of hydration (ΔG_{hyr}) for all ions (Table 4.1, Table 4.2),[30] we assume the solvation behavior of ions in methanol were identical to their hydration behavior.

4.2.4 SICA Effect in Alternative Ion Pairs

In anion and cation specificity studies, we have found that anions have determining effect on the co-activation and cations have modest impact on the co-activation (Figure 4.5). To further verify this, we tested various ion pairs with acetate (1 M), sulfate (1 M), nitrate (1 M) and thiocyanate salts (0.1 M) (Figure 4.6, Figure 4.7). We used the cumulative depolymerization mol % at 24 h to reflect the co-activation effect. A higher depolymerization percentage represents a faster depolymerization rate and a stronger co-activation effect.

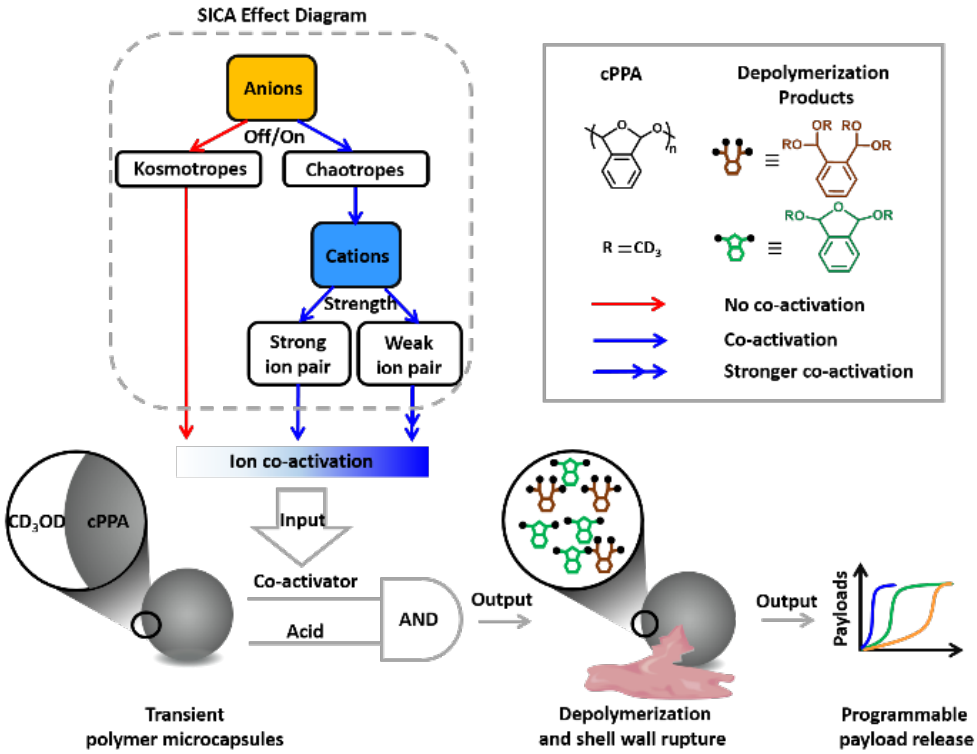

Figure 4.5. The SICA effect at the transient polymer microcapsules interfaces and output reaction cascades.

In all compounds with kosmotropic anions, no co-activation effect was observed (Figure 4.6). This confirmed that anions have a determining effect on the co-activation behavior. Only chaotropic anions switched on the co-activation behavior. In nitrate salts, we observed a V-shaped co-activation effect, owing to weaker ion pairs of $Ca(NO_3)_2$ and NH_4NO_3 compared with KNO_3, based on the LWMA discussion in 4.2.3 (Figure 4.7a). In thiocyanate salts (0.1 M), a descending co-activation effect $Ca^{2+}>Li^{+}>Na^{+}>K^{+}$ was observed, because SCN^{-} forms increasingly stronger ion pair following the order of $Ca^{2+}<Li^{+}<Na^{+}<K^{+}$ (Figure 4.7b). The ion pair strength was estimated by LWMA as illustrated in Figure 4.4 .[22,30] Because the free energy of transfer ($\Delta_{tr}G$) from water to methanol is small compared to the free energy of hydration

($\Delta_{hyr}G$) for all cations,[30] we assume the solvation behaviors of cations in methanol are identical to their hydration behavior.

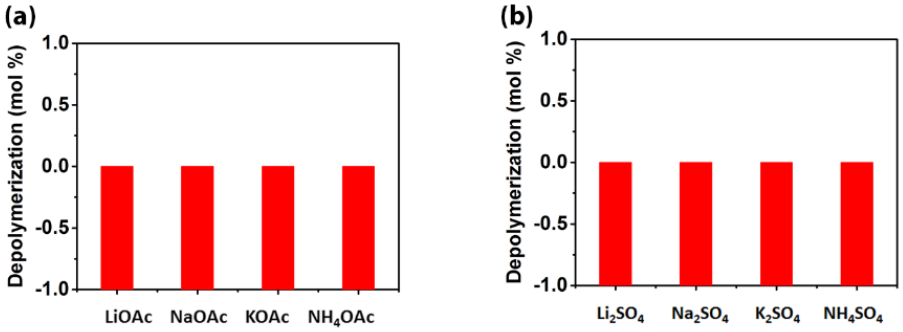

Figure 4.6. Co-activation effects in kosmotropic anion solutions. cPPA microcapsules (M_n=58 kDa, 5 mg/mL) were suspended in methanol-d_4 containing (a) 0.01 M TFA + 1 M acetate salts with different cations, and (b) 0.01 M TFA + saturated sulfate salts with different cations. The co-activation effect for each ion pair was evaluated by the depolymerization mol % at 24 h. A higher depolymerization mol % value indicated a faster depolymerization rate and an increased co-activation. These kosmotropic anions showed no co-activation, because no depolymerization was observed, same as that of microcapsules suspended in salt-free control solutions (0.01 M TFA) for 24 h, which resulted in 0 mol %. The experiments were performed in triplicate and showed 0 mol % depolymerization for all measurement. Note: saturated solutions were used for all sulfate salts due to low solubility of the salts at 1 M concentration.

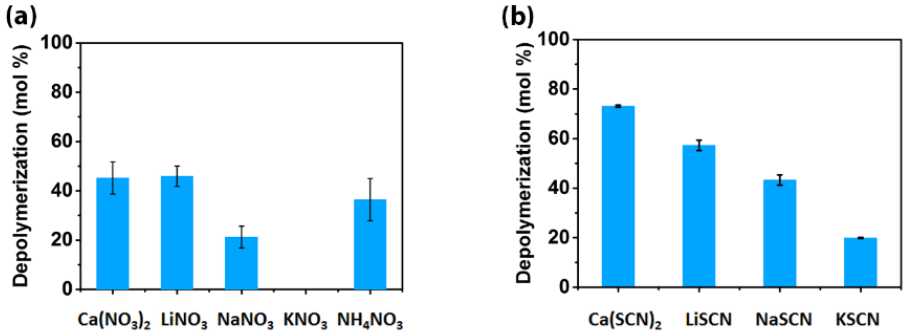

Figure 4.7. Co-activation effects in chaotropic anion solutions. cPPA microcapsules (M_n=58 kDa, 5 mg/mL) were suspended in methanol-d_4 containing (a) 0.01 M TFA + 1 M nitrate salts with different cations, and (b) 0.01 M TFA + 0.1 M thiocyanate salts with different cations. The co-activation effect for each ion pair was evaluated by the depolymerization mol % at 24 h. A higher depolymerization mol % value indicated a faster depolymerization rate and an increased co-activation. The co-activation behavior followed the cation modulating mechanism: the stronger ion-pair yielded a weaker co-activation effect. Error bars represent standard deviation

Figure 4.7. (cont.) of three experiments. Co-activation effects in chaotropic anion solutions. Note: saturated solutions were used for all sulfate salts due to low solubility of the salts at 1 M concentration.

4.3 CONCENTRATION DEPENDENCE IN THE SPECIFIC ION CO-ACTIVATION EFFECT

We further analyzed ion concentration dependence in the SICA effect. In general, we observed a positive concentration-dependent co-activation effect (Figure 4.8). For example, increasing LiCl concentration from 0.1 M to 1 M reduced the t_{D50} from 10.3 ± 1.5 h to 6.0 ± 0.5 h. In LiSCN, however, 0.1 M LiSCN (t_{D50} = 20.6 ± 0.5 h) and 1 M LiSCN (t_{D50} = 22.9 ± 2.5 h) yielded similar depolymerization rate. We speculated this saturation-type concentration effect in LiSCN was attributed to the affinity of the weakly solvated SCN^- to the cPPA interfaces.[11,35] High concentration of SCN^- around the cPPA microcapsules was supported by the significantly more negative zeta potential (-42.6 mV) of 1 M LiSCN compared with that of 1 M LiCl (-2.8 mV). Presumably, the highly charged surface led to electrostatic screening effect, resulting in a saturation-type concentration-dependent co-activation in LiSCN. [11,13]

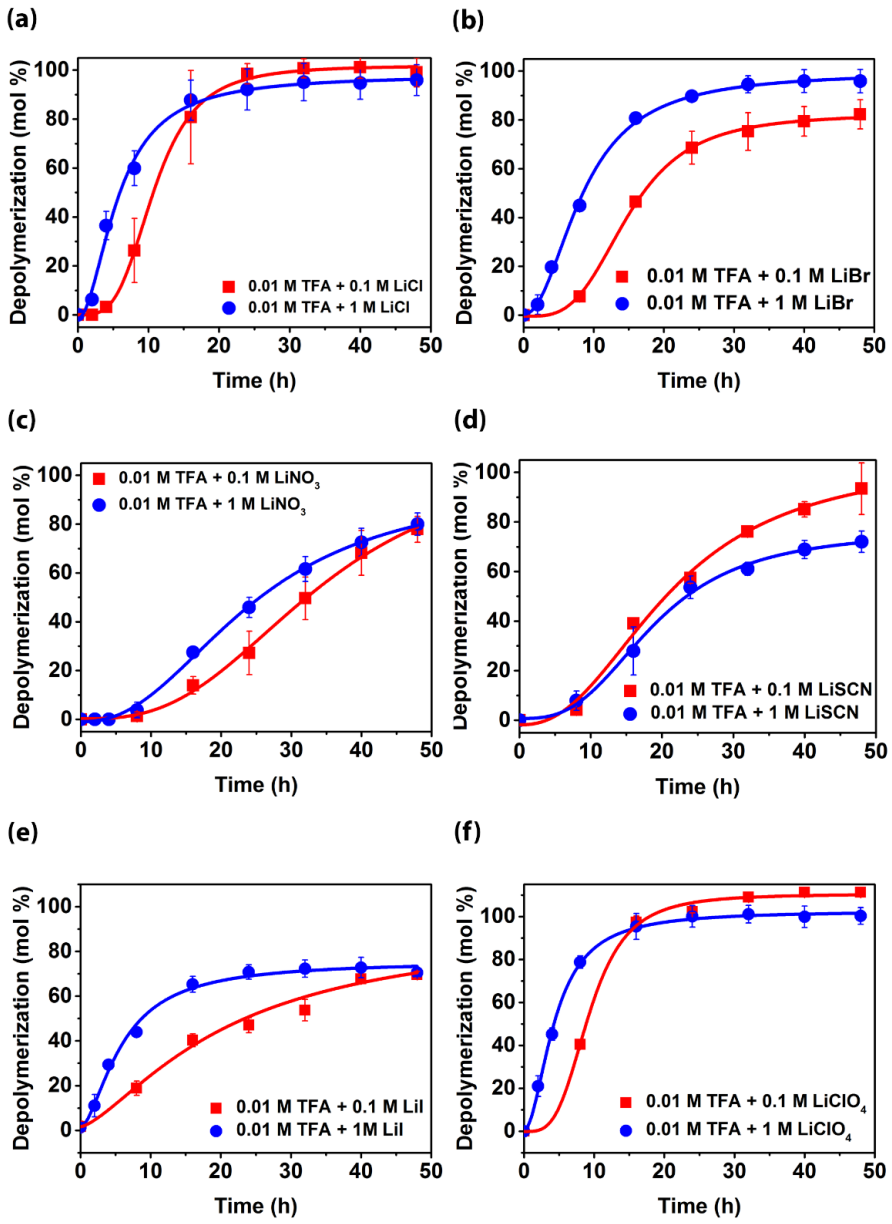

Figure 4.8. Co-activator concentration dependence studies. Shell wall depolymerization profiles of cPPA microcapsules (M_n=58 kDa, ~5 mg/mL) suspended in 0.01 M TFA/methanol-d_4 solutions containing 0.1 M (red) or 1 M (blue) (a) LiCl, (b) LiBr, (c) $LiNO_3$, (d) LiSCN, (e) LiI, and (f) $LiClO_4$. Depolymerization profiles were measured by NMR spectroscopy using ethylene glycol as an internal standard (~5 mg/mL). Data plots were fitted with an empirical logarithmic function (quantification procedures were detailed in 3.5.4). Error bars represent standard deviation of three experiments.

4.4 PAYLOAD RELEASE RATES MODULATED BY THE SPECIFIC ION CO-ACTIVATION EFFECT

The SICA effect resulted in tunable depolymerization rates in the cPPA microcapsule's shell walls. Because the sigmoidal-shaped release profiles were caused by the rupture of the shell walls resulting from the depolymerization, we also expected the SICA effect modulated the payload release rates (Figure 4.9). To measure the payload release profiles, aliquots from microcapsule's suspensions in different ion/acid solutions were collected at designated time. Fluorescence intensities of the diluted aliquot solutions (containing the released Nile red from microcapsules) were measured by a fluorescence spectrometer and normalized to generate the payload release kinetic profiles (4.5.4). The data plots were fitted with an empirical logarithmic function and the payload release half-life (t_{R50}) were abstracted. The t_{R50} correlated with the depolymerization half-life t_{D50}. A shorter shell wall depolymerization half-life yielded a faster payload release rate (Figure 4.9). Therefore, programmable payload release rates was achieved by changing the ionic species in the solutions.

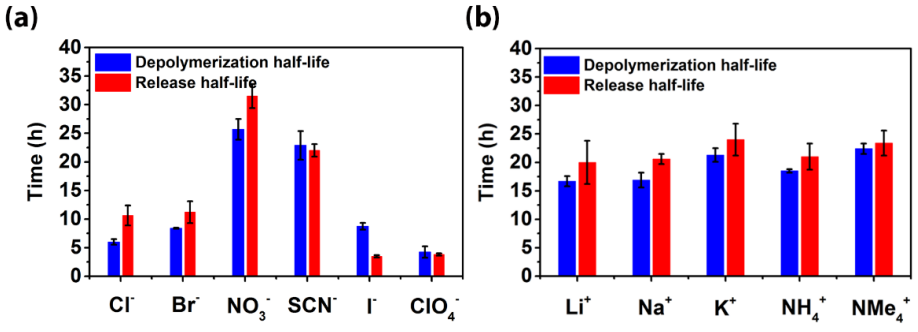

Figure 4.9. Correlation of depolymerization half-life and release half-life. Depolymerization half-life (blue columns) and release half-life (red columns) values of cPPA microcapsules (M_n=58 kDa, ~5 mg/mL) suspended in methanol-d_4 containing (a) 0.01 M TFA + 1 M lithium salts and (b) 0.01 M TFA + 0.02 M chloride salts. The depolymerization half-life and release half-life were abstracted from corresponding depolymerization (Figure 4.13, Figure 4.14) and payload release profiles (Figure 4.15, Figure 4.16).

4.5 EXPERIMENTAL DETAILS

Unless otherwise noted, all chemicals were obtained from Sigma Aldrich and used as received. The monomer *o*-PA (98%, Alfa-Aesar) was purified by hot filtration followed by a single recrystallization according to a literature procedure.[28] DCM was obtained from an anhydrous solvent delivery system equipped with activated alumina columns. All glassware for polymerization was oven dried prior to use. The synthesis of cPPA (M_n=58 kDa, PDI=1.6) followed previous literature procedures with minor modifications.[36] Depolymerization profiles, data fitting, SEM, and pH measurements followed the same procedures and quantification methods used in Chapter 3, 3.5.

4.5.1 Microcapsules Suspended in Salt Solutions

To test the effect of salts (acid-free) on the cPPA depolymerization, the cPPA microcapsules were suspended in LiCl (1 M) and LiSCN (1 M) for two weeks. Morphology studies (Figure 4.10-Figure 4.11) and NMR spectra confirmed no apparent depolymerization after two weeks' treatment, indicating salts are co-activators.

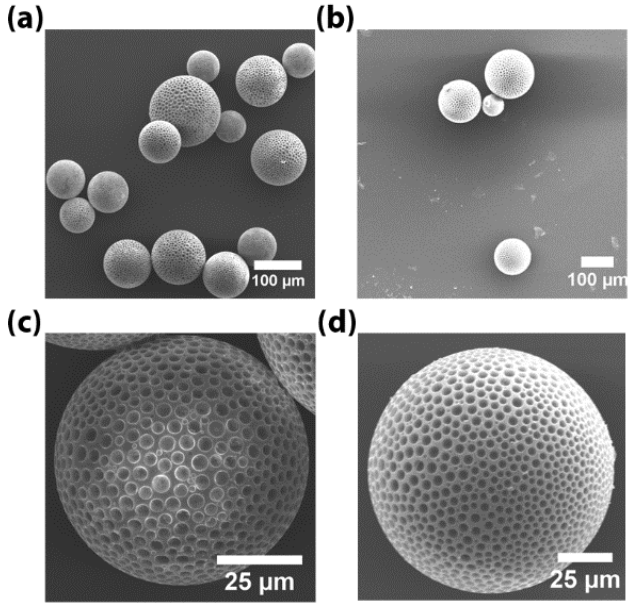

Figure 4.10. SEM images of cPPA microcapsules suspended in acid-free methanol-d_4 solutions containing (a) (c) 1 M LiCl and (b) (d) 1 M LiSCN for two weeks. After two week, the microcapsule's suspensions were filtered and the microcapsules left on the filter paper were imaged. Microcapsules showed identical morphologies without apparent shell wall erosion. Their morphologies are similar to the as-synthesized microcapsule's morphology (shown in Chapter 3, Figure 3.14).

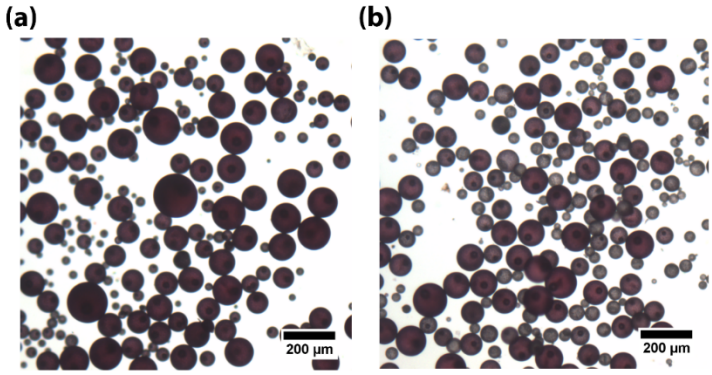

Figure 4.11. In situ optical microscopy images of cPPA microcapsules suspended in acid-free methanol-d_4 solutions containing (a) 1 M LiCl and (b) 1 M LiSCN for two weeks. After two weeks, the microcapsule's suspensions were imaged under an optical microscope. Microcapsules showed no morphology changes in both solutions.

4.5.2 Depolymerization Profiles

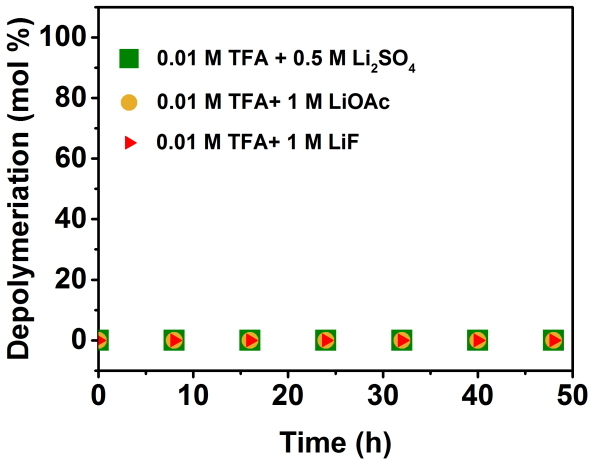

Figure 4.12. Effect of kosmotropic anions on cPPA depolymerization. Shell wall depolymerization profiles of cPPA microcapsules (M_n=58 kDa, ~5 mg/mL) suspended in 0.01 M TFA/methanol-d_4 solutions containing 0.05 M Li_2SO_4 (green), 1 M LiOAc (yellow), or 1 M LiF (red). Depolymerization profiles were measured by NMR spectroscopy using ethylene glycol as an internal standard (5 mg/mL). The data plots were average values of three experiments and error bars were hidden within the plots. Note: saturated lithium sulfate and lithium fluoride solutions were used due to low solubility of salts at designated concentrations.

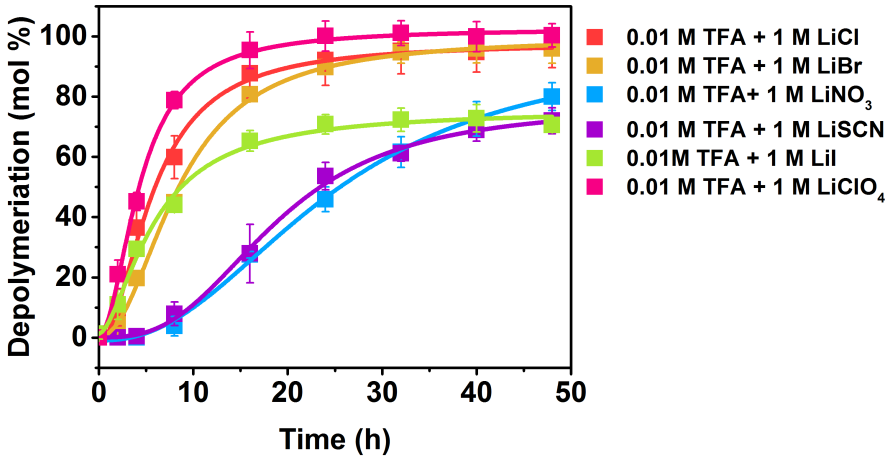

Figure 4.13. Effect of chaotropic anions on cPPA depolymerization. Shell wall depolymerization profiles of cPPA microcapsules (M_n=58 kDa, ~5 mg/mL) suspended in 0.01 M TFA/methanol-d_4 solutions containing 1 M lithium salts with different chaotropic anions. Depolymerization profiles were measured by NMR spectroscopy using ethylene glycol as an internal standard (~5 mg/mL). The data plots were fitted with an empirical logarithmic function. Error bars represent standard deviation of three experiments.

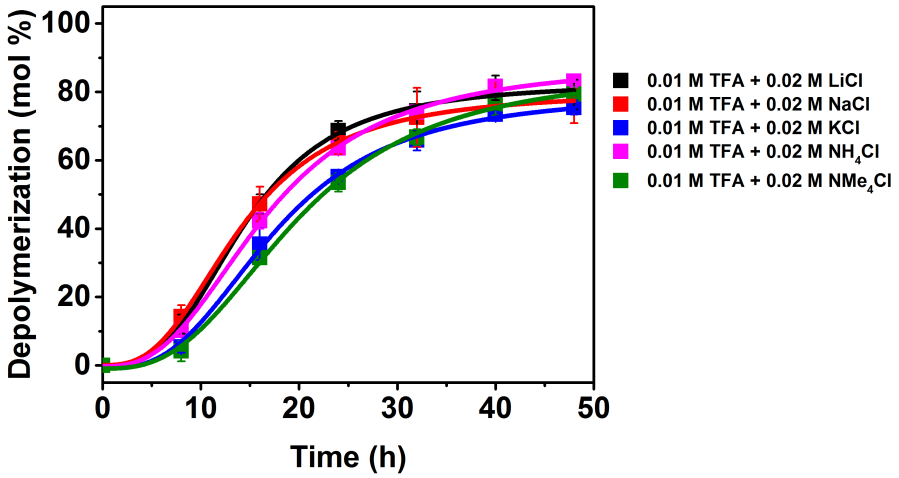

Figure 4.14. Effect of cations on cPPA depolymerization. Shell wall depolymerization profiles of cPPA microcapsules (M_n=58 kDa, ~5 mg/mL) suspended in 0.01 M TFA/methanol-d_4 solutions containing 0.02 M chloride salts with different cations. Depolymerization profiles were measured by NMR spectroscopy using ethylene glycol as an internal standard (~5 mg/mL). The data plots were fitted with an empirical logarithmic function. Error bars represent standard deviation of three experiments.

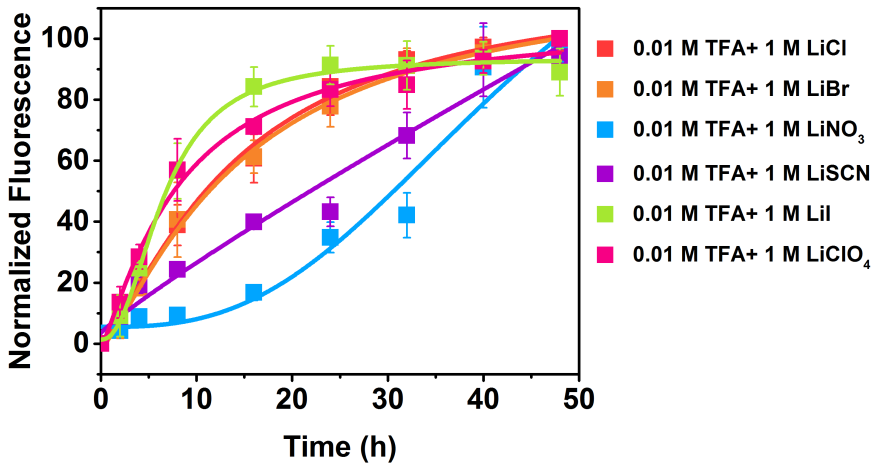

Figure 4.15. Effect of anions on payload release rates. Payload release profiles of cPPA microcapsules (M_n=58 kDa, ~5 mg/mL) suspended in 0.01 M TFA/methanol-d_4 solutions containing 1 M lithium salts with different anions. Release profiles were measured by a fluorescence spectrometer and was quantified by normalization. The data plots were fitted with an empirical logarithmic function. Error bars represent standard deviation of three experiments.

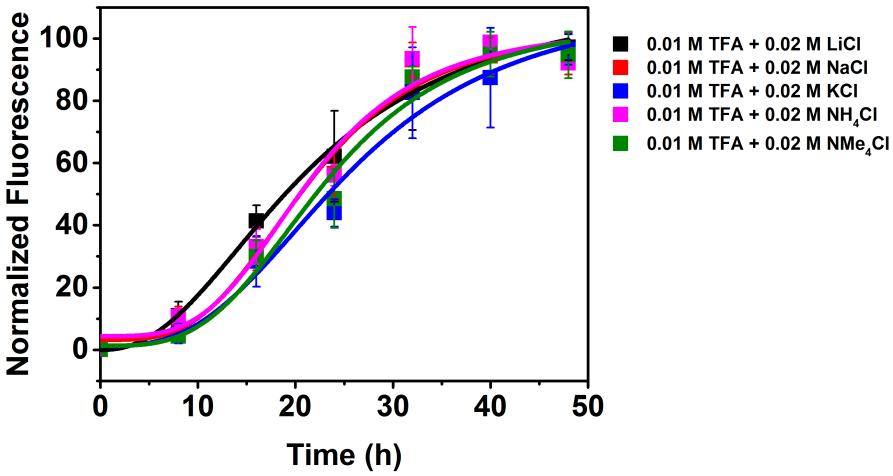

Figure 4.16. Effect of cations on payload release rates. Payload release profiles of cPPA microcapsules (M_n=58 kDa, ~5 mg/mL) suspended in 0.01 M TFA/methanol-d_4 solutions containing 0.02 M chloride salts with different cations. Release profiles were measured by a fluorescence spectrometer and was quantified by normalization. The data plots were fitted with an empirical logarithmic function. Error bars represent standard deviation of three experiments.

Table 4.3. Summary of Depolymerization Half-Life and Release Half-Life

Salts*	pH Meter Value	Apparent pH Value	Depolymerization Half-life (h)	Release Half-life (h)
Salt-free, 0.01 M TFA	-0.035	3	> 48 h	-
1 M LiCl	-0.549	3	6.0 ± 0.5	10.6 ± 1.7
1 M LiBr	-0.662	3	8.4 ± 0.1	11.2 ± 1.9
1 M $LiNO_3$	0.850	3	25.7 ± 1.8	31.5 ± 2.1
1 M LiSCN	1.242	4	22.9 ± 2.5	22.0 ± 1.1
1 M LiI	0.085	3	8.8 ± 0.6	3.8 ± 0.2
1 M $LiClO_4$	-0.748	3	4.2 ± 1.0	3.5 ± 2.2
0.02 M LiCl	-0.233	3	16.7 ± 0.9	20.0 ± 3.8
0.02 M NaCl	-0.266	3	16.9 ± 1.3	20.6 ± 0.9
0.02 M KCl	-0.252	3	21.3 ± 1.2	24.0 ± 2.8
0.02 M NH_4Cl	-0.241	3	18.5 ± 0.3	21.0 ± 2.3
0.02 M NMe_4Cl	-0.236	3	22.4 ± 0.9	23.4 ± 2.2

** Salts solutions were all mixed with 0.01 M TFA. LiSCN solution were prepared with $LiSCN{\cdot}xH_2O$ as received from Sigma Aldrich. The concentration was calculated based on the molar mass of LiSCN.*

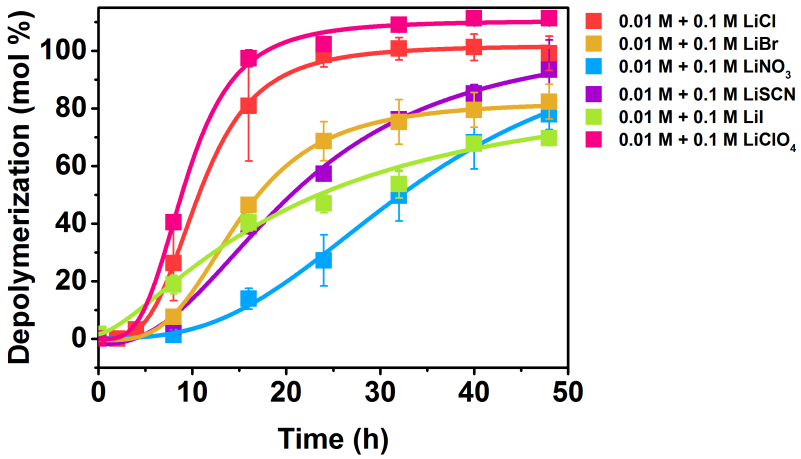

Figure 4.17. Effect of chaotropic anions on cPPA depolymerization. Shell wall depolymerization profiles of cPPA microcapsules (M_n= 58kDa, ~5 mg/mL) suspended in 0.01 M TFA/methanol-d_4 solutions containing 0.1 M lithium salts with different chaotropic anions. Depolymerization profiles were measured by NMR spectroscopy using ethylene glycol as an internal standard (~5 mg/mL). The data plots were fitted with an empirical logarithmic function. Error bars represent standard deviation of three experiments.

Table 4.4. Summary of Depolymerization Half-life in 0.1 M Lithium Salts Solutions

Salts*	Depolymerization at 16 h (mol %)	Depolymerization Half-life (h)
0.1 M LiCl	80.8 ± 19.1	10.3 ± 1.5
0.1 M LiBr	46.5 ± 2.1	17.2 ± 1.0
0.1 M $LiNO_3$	13.9 ± 3.6	32.2 ± 3.9
0.1 M LiSCN	39.0 ± 1.2	20.6 ± 0.5
0.1 M LiI	40.3 ± 2.9	25.3 ± 2.9
0.1 M $LiClO_4$	95.4 ± 6.0	8.8 ± 0.1

** Salts solutions were all mixed with 0.01 M TFA*

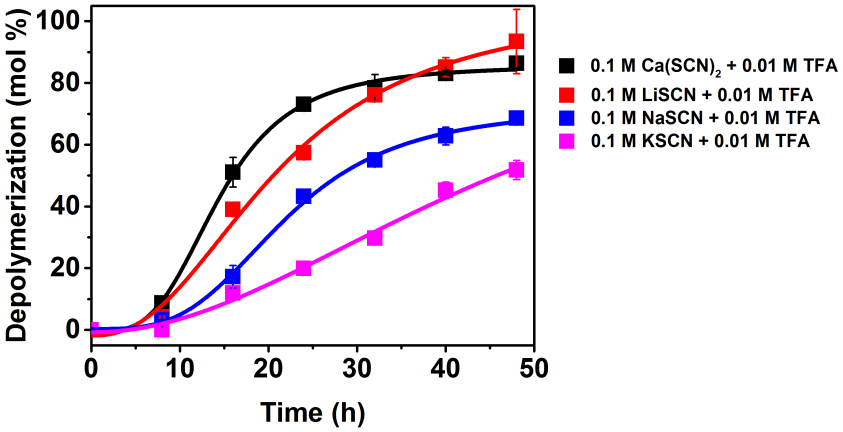

Figure 4.18. Effect of cations on cPPA depolymerization. Shell wall depolymerization profiles of cPPA microcapsules (M_n=58 kDa, ~5 mg/mL) suspended in 0.01 M TFA/methanol-d_4 solutions containing 0.1 M thiocyanate salts with different cations. Depolymerization profiles were measured by NMR spectroscopy using ethylene glycol as an internal standard (~5 mg/mL). The data plots were fitted with an empirical logarithmic function. Error bars represent standard deviation of three experiments.

Table 4.5. Summary of Depolymerization Half-life in 0.1 M Thiocyanate Salts Solutions

Salts*	Depolymerization at 24 h (mol %)	Depolymerization Half-life (h)
0.05 M $Ca(SCN)_2$	73.1 ± 0.5	15.9 ± 0.8
0.1 M LiSCN	57.3 ± 2.1	20.6 ± 0.5
0.1 M NaSCN	43.3 ± 2.0	27.9 ± 1.1
0.1 M KSCN	19.9 ± 0.2	45.6 ± 2.0

** Salts solutions were all mixed with 0.01 M TFA*

4.5.3 NMR Spectra

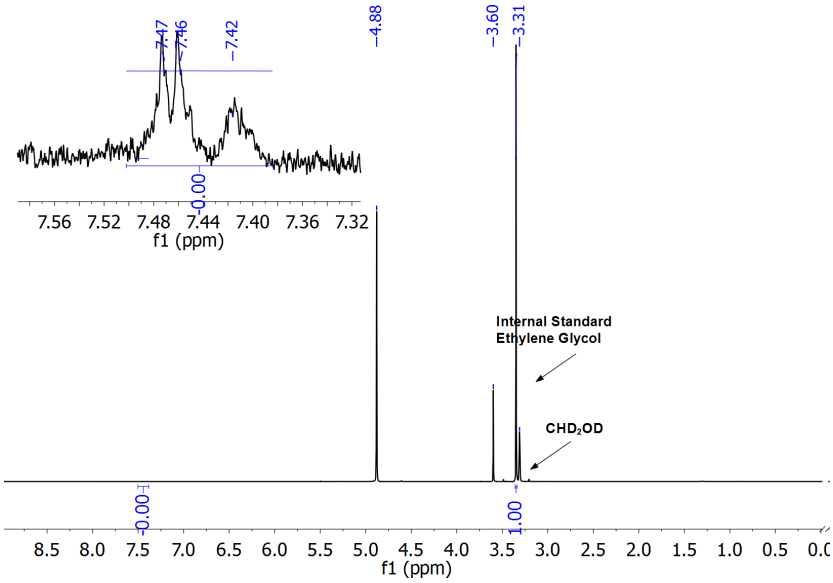

Figure 4.19. ^{1}H NMR spectrum of microcapsules suspended in acid-free 1 M LiCl for 2 weeks. No depolymerization products were observed. Solvent: methanol-d_4.

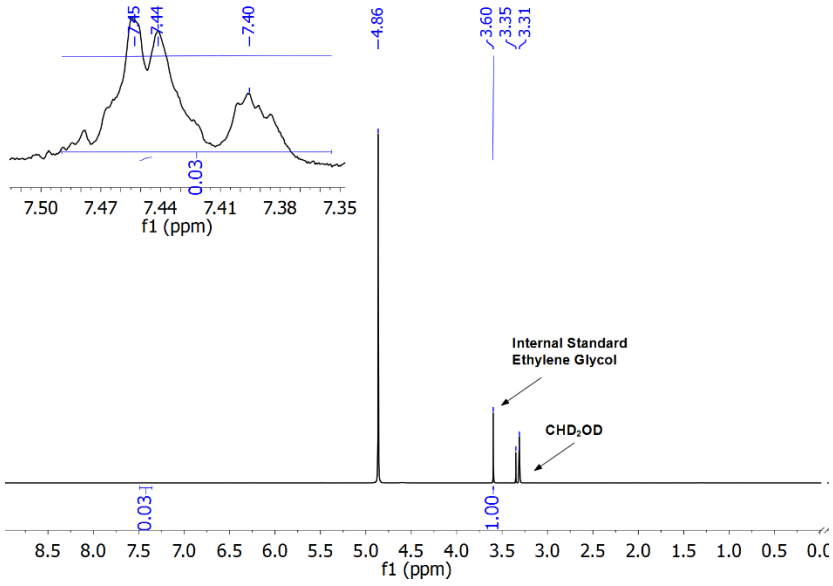

Figure 4.20. ^{1}H NMR spectrum of microcapsules suspended in acid-free 1 M LiSCN for 2 weeks. No depolymerization products were observed. Solvent: methanol-d_4.

4.5.4 Release Profiles Measurements

Nile red was encapsulated in the cPPA microcapsules to facilitate the payloads release profiles measurements. The fluorescence intensities of the collected aliquot supernatant solutions that used in depolymerization profiles were measured for payload release profiles. The release profiles were calculated by the same equation used in depolymerization profiles and normalized to [0, 100]. Release profiles were fitted based on an empirical logarithmic function as shown below,[37]

$$R = \frac{R_0 - R_f}{1 + (\frac{t}{t'_{R_{50}}})^n} + R_f \qquad 4.1$$

where R_0 is release % at t = 0 h, R_f is release % at t = 48 h, and n is order exponent. $t'_{R_{50}}$ is the apparent release half-life, corresponding to where $R = \frac{R_f - R_0}{2}$. Similar to the depolymerization half-life, the actual release half-life $t_{R_{50}}$ was extracted from the fitting curves using R=50. The results were reported based on the average of at least three independent experiments.

4.6 REFERENCES

Notes: This chapter is a collaborative work with Liuyan Tang, Dr. Xiaocun Lu, and Huiying Liu. S.T. authored the text, performed cPPA synthesis, prepared microcapsules, characterized materials (NMR, SEM, release profiles) and analyzed the results. Liuyan Tang worked with S.T. in NMR, pH, release profiles measurements and titration. Dr. Xiaocun Lu and Huiying Liu worked with S.T. in NMR and results analysis. This chapter has previously been published in the following reference: **Tang, S.**; Tang, L.; Lu, X.; Liu, H.; Moore, J. S., "Programmable Payload Release Triggered by a Specific Ion Co-activation Effect", *J. Am. Chem. Soc.* **2018**, *140*, 94-97. **DOI:** 10.1021/jacs.7b11022. The materials are reproduced/adapted with permission.

(1) Warren, J. C.; Stowring, L.; Morales, M. F. The Effect of Structure-Disrupting Ions on the Activity of Myosin and Other Enzymes. *J. Biol. Chem.* **1966**, *241*, 309–315.

(2) Clapham, D. E. Calcium Signaling. *Cell* **1995**, *80*, 259–268.

(3) Clapham, D. E. Calcium Signaling. *Cell* **2007**, *131*, 1047–1058.

(4) Allbritton, N. L., Meyer, T. Localized Calcium Spikes and Propagating Calcium Waves. *Cell Calcium* **1993**, *14*, 691–697.

(5) Lang, F. Mechanisms and Significance of Cell Volume Regulation. *J. Am. Coll. Nutr.* **2007**, *26*, 613S–623S.

(6) Bilkova, E.; Pleskot, R.; Rissanen, S.; Sun, S.; Czogalla, A.; Cwiklik, L.; Róg, T.; Vattulainen, I.; Cremer, P. S.; Jungwirth, P.; Coskun, Ü. Calcium Directly Regulates Phosphatidylinositol 4,5-Bisphosphate Headgroup Conformation and Recognition. *J. Am. Chem. Soc.* **2017**, *139*, 4019–4024.

(7) Lo Nostro, P.; Ninham, B. W. Hofmeister Phenomena: An Update on Ion Specificity in Biology. *Chem. Rev.* **2012**, *112*, 2286–2322.

(8) Hofmeister, F. Zur Lehre von Der Wirkung Der Salze - Zweite Mittheilung. *Arch. Exp. Pathol. Pharmakol.* **1888**, *24*, 247–260.

(9) Yang, Z. Hofmeister Effects: An Explanation for the Impact of Ionic Liquids on Biocatalysis. *J. Biotechnol.* **2009**, *144*, 12–22.

(10) Okur, H. I.; Kherb, J.; Cremer, P. S. Cations Bind Only Weakly to Amides in Aqueous Solutions. *J. Am. Chem. Soc.* **2013**, *135*, 5062–5067.

(11) Heyda, J.; Okur, H. I.; Hladílková, J.; Rembert, K. B.; Hunn, W.; Yang, T.; Dzubiella, J.; Jungwirth, P.; Cremer, P. S. Guanidinium Can Both Cause and Prevent the Hydrophobic Collapse of Biomacromolecules. *J. Am. Chem. Soc.* **2017**, *139*, 863–870.

(12) Zhang, Y. J.; Furyk, S.; Bergbreiter, D. E.; Cremer, P. S. Specific Ion Effectis on the Water Solubility of Acromolecules: PNIPAM and the Hofmeister Series. *J. Am. Chem. Soc.* **2005**, *127*, 14505–14510.

(13) Zhang, Y.; Cremer, P. S. The Inverse and Direct Hofmeister Series for Lysozyme. *Proc. Natl. Acad. Sci. U. S. A.* **2009**, *106*, 15249–15253.

(14) Chen, X.; Yang, T.; Kataoka, S.; Cremer, P. S. Specific Ion Effects on Interfacial Water Structure near Macromolecules. *J. Am. Chem. Soc* **2007**, *129*, 12272–12279.

(15) Furyk, S.; Zhang, Y.; Ortiz-Acosta, D.; Cremer, P. S.; Bergbreiter, D. E. Effects of End Group Polarity and Molecular Weight on the Lower Critical Solution Temperature of poly(N-Isopropylacrylamide). *J. Polym. Sci., Part A Polym. Chem.* **2006**, *44*, 1492–1501.

(16) Zhang, Y.; Furyk, S.; Sagle, L. B.; Cho, Y.; Bergbreiter, D. E.; Cremer, P. S. Effects of Hofmeister Anions on the LCST of PNIPAM as a Function of Molecular Weight. *J. Phys. Chem. C.* **2007**, *111*, 8916-8924.

(17) Kunz, W.; Lo Nostro, P.; Ninham, B. W. W. The Present State of Affairs with Hofmeister Effects. *Curr. Opin. Colloid Interface Sci.* **2004**, *9*, 1–18.

(18) Kunz, W. Specific Ion Effects in Colloidal and Biological Systems. *Curr. Opin. Colloid Interface Sci.* **2010**, *15*, 34–39.

(19) Gibb, C. L. D.; Oertling, E. E.; Velaga, S.; Gibb, B. C. Thermodynamic Profiles of Salt Effects on a Host-Guest System: New Insight into the Hofmeister Effect. *J. Phys. Chem. B* **2015**, *119*, 5624–5638.

(20) Gibb, C. L. D.; Gibb, B. C. Anion Binding to Hydrophobic Concavity Is Central to the Salting-in Effects of Hofmeister Chaotropes. *J. Am. Chem. Soc.* **2011**, *133*, 7344–7347.

(21) Vrbka, L.; Vondrásek, J.; Jagoda-Cwiklik, B.; Vácha, R.; Jungwirth, P. Quantification and Rationalization of the Higher Affinity of Sodium over Potassium to Protein Surfaces. *Proc. Natl. Acad. Sci.* **2006**, *103*, 15440–15444.

(22) Fox, J. M.; Kang, K.; Sherman, W.; Heroux, A.; Sastry, G. M.; Baghbanzadeh, M.; Lockett, M. R.; Whitesides, G. M. Interactions between Hofmeister Anions and the Binding Pocket of a Protein. *J. Am. Chem. Soc.* **2015**, *137*, 3859–3866.

(23) Esser-Kahn, A. P.; Odom, S. A.; Sottos, N. R.; White, S. R.; Moore, J. S. Triggered Release from Polymer Capsules. *Macromolecules* **2011**, *44*, 5539–5553.

(24) White, S. R.; Moore, J. S.; Sottos, N. R.; Krull, B. P.; Santa Cruz, W. A.; Gergely, R. C. R. Restoration of Large Damage Volumes in Polymers. *Science* **2014**, *344*, 620–623.

(25) DiLauro, A. M.; Abbaspourrad, A.; Weitz, D. A.; Phillips, S. T. Stimuli-Responsive Core-Shell Microcapsules with Tunable Rates of Release by Using a Depolymerizable Poly(phthalaldehyde) Membrane. *Macromolecules* **2013**, *46*, 3309–3313.

(26) Peterson, G. I.; Larsen, M. B.; Boydston, A. J. Controlled Depolymerization: Stimuli-Responsive Self-Immolative Polymers. *Macromolecules* **2012**, *45*, 7317–7328.

(27) Tang, S.; Yourdkhani, M.; Casey, C. M. P.; Sottos, N. R.; White, S. R.; Moore, J. S. Low-

Ceiling-Temperature Polymer Microcapsules with Hydrophobic Payloads via Rapid Emulsion-Solvent Evaporation. *ACS Appl. Mater. Interfaces* **2017**, *9*, 20115–20123.

(28) DiLauro, A. M.; Robbins, J. S.; Phillips, S. T. Reproducible and Scalable Synthesis of End-Cap-Functionalized Depolymerizable Poly(phthalaldehydes). *Macromolecules* **2013**, *46*, 2963–2968.

(29) Wong, A. D.; DeWit, M. A.; Gillies, E. R. Amplified Release through the Stimulus Triggered Degradation of Self-Immolative Oligomers, Dendrimers, and Linear Polymers. *Adv. Drug. Deliv. Rev.* **2012**, *64*, 1031–1045.

(30) Marcus, Y. *Ion Properties*; CRC Press, 1997; Vol. 1.

(31) Lutter, J. C.; Wu, T.; Zhang, Y. Hydration of Cations□: A Key to Understanding of Specific Cation on Aggregation Bahaviors of PEO-PPO-PEO Triblock Copolymers. *J. Phys. Chem. B.* **2013**, *117*, 10132.

(32) Hess, B.; Van Der Vegt, N. F. A. Cation Specific Binding with Protein Surface Charges. *Proc. Natl. Acad. Sci. U. S. A.* **2009**, *106*, 13296–13300.

(33) Duignan, T. T.; Parsons, D. F.; Ninham, B. W. Collins's Rule, Hofmeister Effects and Ionic Dispersion Interactions. *Chem. Phys. Lett.* **2014**, *608*, 55–59.

(34) Collins, K. D. Why Continuum Electrostatics Theories Cannot Explain Biological Structure, Polyelectrolytes or Ionic Strength Effects in Ion-Protein Interactions. *Biophys. Chem.* **2012**, *167*, 33–49.

(35) Wang, L. H.; Zhang, Z. D.; Hong, C. Y.; He, X. H.; You, W.; You, Y. Z. Anion-Dipole Interactions Make the Homopolymers Self-Assemble into Multiple Nanostructures. *Adv. Mater. (Weiheim. Ger.)* **2015**, *27*, 3202–3207.

(36) Kaitz, J. A.; Diesendruck, C. E.; Moore, J. S. End Group Characterization of Poly(phthalaldehyde): Surprising Discovery of a Reversible, Cationic Macrocyclization Mechanism. *J. Am. Chem. Soc.* **2013**, *135*, 12755–12761.

(37) Seefeldt, S. S.; Jensen, J. E.; Fuerst, E. P. Log-Logistic Analysis of Herbicide Dose-Response Relationships. *Weed Technol.* **1995**, *9*, 218–227.

CHAPTER 5 : DEPOLYMERIZATION TRIGGERED BY LEWIS ACIDS AND COACTIVATORS

5.1 INTRODUCTION

The cationic polymerization and depolymerization mechanisms of cPPA are known to go through the same cationic intermediates (Figure 5.1).[1,2] This indicates that the Lewis acid initiators for cPPA polymerization are potential chemical stimuli for cPPA depolymerization. In the SICA effect studies from Chapter 4, we have analyzed a series of anions and cations that co-activate cPPA depolymerization with Brønsted acids. To further expand the stimuli library for triggered cPPA depolymerization in a mild reaction environment, in this chapter, we demonstrated Lewis acids such as divalent or transition metal ions triggered cPPA depolymerization and the ion co-activation effect was applicable to these Lewis acid and accelerated the depolymerization rates.

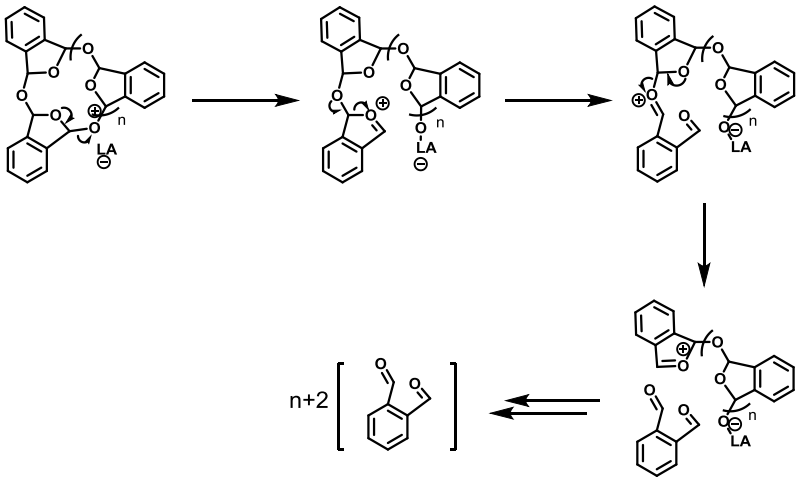

Figure 5.1. Proposed Lewis acid catalyzed cPPA depolyerization mechanism redraw from reference [3–5].

5.2 EFFECT OF LEWIS ACIDS ON CPPA DEPOLYMERIZATION

To test the Lewis acid effects on cPPA depolymerization, three metal cations (Li^+, Zn^+, Mg^+) with different acidities were selected as listed in Table 5.1.[6] We mainly focused on studying the metal ions based Lewis acids because of our interest to develop ion-triggered microcapsules for batteries and anticorrosion applications. Therefore, Lewis acids such as boron halides were not examined here. The Lewis acidities of these metal ions are collected from references.[6,7] The Lewis acidities were represented by Kamlet-Taft parameter α, which described the ability to donate a hydrogen bond or accept an electron pair.[6] The calculation of α was based on equation 5.1 and 5.2 from reference [6],

$$\alpha = A_+ / (-43.8) \qquad 5.1$$

$$A_+ = -(3.72)z_+^2 / r_+ - 3.78R_{D+} \qquad 5.2$$

where z_+ is the charge of the cations, r_+ is the radius (in nm) of the cations, and R_{D+} is the molar refractivity (cm^3/mol) of the cations.

Table 5.1. Lewis Acidities of the Examined Metal Ions in the Literature [6]

Ions	Kamlet-Taft Value α
Li (I)	1.24
Zn (II)	4.65
Mg (II)	4.66

We examined Li (I), Mg (II), and Zn (II) salts with two different counter anions: chloride (Cl^-) and bistriflimide ($TFSI^-$). A polar aprotic solvent, tetrahydrofuran (THF-d_8), was selected to

prepare cPPA solutions (M_n=55 kDa, PDI=1.6, 5 mg/mL) for the depolymerization studies with the Lewis acids (0.01 M-0.1 M in THF-d_8). Unlike the cPPA microcapsule's suspensions in methanol (cPPA is not soluble in methanol) used in Chapter 3 and Chapter 4, cPPA is soluble in THF and forms a homogeneous solution. We studied the cPPA/THF solutions with Lewis acids to analyze the intrinsic effects of Lewis acids on cPPA depolymerization and exclude the effects of interfaces in microcapsule's suspensions. THF also has good solubility for all examined Lewis acid compounds at the desired concentrations (0.01 M-0.1 M) (except for $MgCl_2$).

The cPPA depolymerization rates in the presence of different Lewis acids were studied by their corresponding depolymerization mol % at 48 h. The ^{1}H NMR spectra of cPPA/THF/Lewis acids solutions were collected after 48 h treatment *in situ*. The depolymerization mol % was calculated by comparing the integration of the depolymerization products peaks (*o*-PA, aromatic protons, 4 H, 7.77-8.00 ppm) over the integration of the remained cPPA polymer peaks (acetal protons, 2 H, 6.30-7.15 ppm). For the Cl^- salts, the depolymerization rates were Mg (II) (70 ± 1 mol %) > Li (I) (64 ± 4 mol %) > Zn (II) (7 ± 1 mol %), as reflected by the depolymerization mol % at 48 h (Figure 5.2a). For the $TFSI^-$ salts, the depolymerization rates were Mg (II) (92 ± 8 mol %) ≈ Zn (II) (90 ± 10 mol %) > Li (I) (50 ± 7 mol %) (Figure 5.2b). For the $TFSI^-$ salts, the ordering of depolymerization rates correlated with the Lewis acidities of the metal cations as listed in Table 5.1. This supports the hypothesis that the Lewis acids are chemical stimuli to trigger cPPA depolymerization without Brønsted acids. Notably, for the chloride salts, the ordering of depolymerization rates did not correlate with the Lewis acidities, which indicated that the metal ions were not the sole contributor that caused the depolymerization.

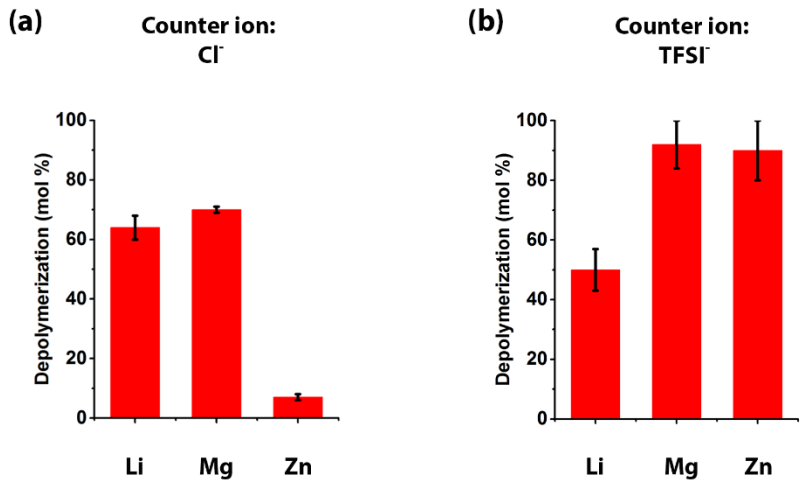

Figure 5.2. Comparison of depolymerization rates in cPPA/THF/Lewis acids solutions, as represented by depolymerization mol % at 48 h. cPPA: M_n=55 kDa, PDI=1.6, 5 mg/mL in THF-d_8; Lewis acids: 0.01 M in THF-d_8. Note: $MgCl_2$ saturated solutions were used, because it is not fully soluble in THF at the concentration of 0.01M.

To further validate the importance of metal ions in cPPA depolymerization, a control study was performed with solutions containing crown ethers to form complexes with metal ions (12-crown-4 for lithium salts and 15-crown-4 for magnesium and zinc salts).[8] The depolymerization mol % in cPPA/THF/Lewis acids/crown ethers solutions at 48 h was plotted in Figure 5.3. For both $TFSI^-$ and Cl^- salts, the addition of crown ethers inhibited the depolymerization, evidenced by the less pronounced depolymerization than solutions without the crown ethers (Figure 5.2, Figure 5.3). The formation of metal ion-crown ether complexes reduced the availability of metal ions to catalyze the cPPA depolymerization. These results corroborate our hypothesis that metal ions catalyze the cPPA depolymerization. Also notably, in crown ether solutions containing LiCl, $MgCl_2$, or $Mg(TFSI)_2$, more than 30 mol % depolymerization was observed after 48 h. The resulting depolymerization in the crown ether

solutions is presumably triggered by Brønsted acids generated from hydrolysis of the metal ions and decompositions of the ionic compounds.

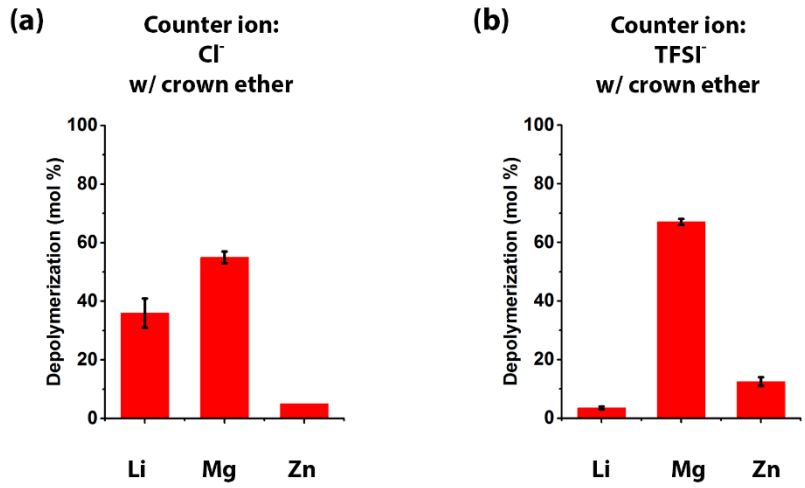

Figure 5.3. Depolymerization mol % in cPPA/THF/Lewis acids/crown ether solutions at 48 h. cPPA: M_n=55 kDa, PDI=1.6, 5 mg/mL in THF-d_8; Lewis acids: 0.01 M in THF-d_8; Crown ethers: 0.011 M in THF-d_8; 12-crown-4 was used for lithium salts and 15-crown-4 was used for magnesium and zinc salts. Note: $MgCl_2$ saturated solutions were used, because it is not fully soluble in THF at the concentration of 0.01M.

5.3 ION CO-ACTIVATION EFFECTS IN LEWIS ACID SOLUTIONS

Accelerated cPPA depolymerization rates in the Lewis acid solutions were achieved by adding LiCl as the co-activators. Generalizing the co-activation effects in Lewis acid solutions is beneficial to develop ion-triggered materials in mild environments. LiCl is chosen as the co-activator (0.1 M in THF-d_8) because it effectively accelerates cPPA depolymerization rates (Chapter 3 and 4) and is soluble in THF up to 1 M. The depolymerization mol % at 48 h was used to estimate and compare the depolymerization rates in solutions with or without adding the co-activator, LiCl. Similarly, the depolymerization mol % was calculated by comparing the integration of the depolymerization products peaks (*o*-PA, aromatic protons, 4 H, 7.80-8.05 ppm)

over the integration of the remained cPPA polymer peaks (acetal protons, 2 H, 6.30-7.15 ppm). LiCl effectively accelerated the depolymerization rates (Figure 5.4b) compared with solutions without LiCl (Figure 5.4a). The solution pH values in Table 5.2 also suggested that the depolymerization occurred in a mild acidic solutions (pH= 3~4). It should be noted that the behavior of LiCl in THF solutions and methanol solutions are different. In THF solutions, LiCl by itself catalyzed the cPPA depolymerization, but did not lead to depolymerization in cPPA microcapsule/methanol suspensions after 2 weeks. The difference in depolymerization kinetics can be attributed to a faster depolymerizaiton rate in homogeneous (cPPA/THF solutions) than in heterogeneous (cPPA microcapsules/methanol suspensions) systems.[9] Further investigation on the solvent effect and interface effect of cPPA depolymerization will provide more insights on the depolymerization kinetics and co-activation effect mechanisms.

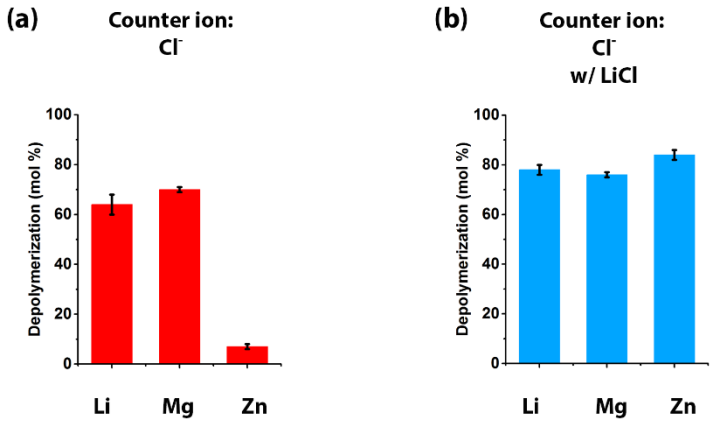

Figure 5.4. Comparison of depolymerization rates in cPPA/THF/Lewis acids solutions with or without co-activator LiCl, as represented by depolymerization mol % in different solutions at 48 h. cPPA: M_n=55 kDa, PDI=1.6, 5 mg/mL in THF-d_8; Lewis acids: 0.01 M in THF-d_8; Co-activator: LiCl 0.1 M in THF-d_8. Note: $MgCl_2$ saturated solution was used as it is not fully soluble in THF at the concentration of 0.01M.

5.4 EXPERIMENTAL DETAILS

5.4.1 Materials and Instrumentations

Unless otherwise noted, all chemicals were obtained from Sigma Aldrich and used as received. The monomer *o*-PA (98%, Alfa-Aesar) was purified by hot filtration followed by a single recrystallization according to a literature procedure.[10] DCM was obtained from an anhydrous solvent delivery system equipped with activated alumina columns. All glassware for polymerization was oven dried prior to use. The synthesis of cPPA (M_n=55 kDa, PDI=1.6) followed previous literature procedures with minor modifications.[11]

The molecular weight of cPPA was determined by an analytical gel permeation chromatograph (GPC) analyses were performed with a Waters1515 Isocratic HPLC pump, a Waters (2998) Photodiode Array Detector, a Waters (2414) Refractive Index Detector, a Waters (2707) 96-well autosampler, and a series of 4 Waters HR Styragel 3wcolumns (7.8 x 300mm, HR1, HR3, HR4, and HR5) in THF at 30 °C. The GPC was calibrated using monodisperse polystyrene standards.

NMR spectra were recorded using a Bruker 500 MHz spectrometer with broad-band CryoProbe and automation. Chemical shifts were reported in δ (ppm) relative to the residual solvent peak THF-d_8 (1.72 ppm). The depolymerization mol % in cPPA homogeneous solutions were measured *in situ* after 48 h treatment, and the quantification was determined by comparing the integration of the depolymerization products peaks (*o*-PA, aromatic protons, 4 H, 7.77-8.00 ppm) over the integration of the remained cPPA polymer peaks (acetal protons, 2 H, 6.30-7.15 ppm). pH indicator was bromocresol purple. pH measurements for solutions used a pH meter

(Metrohm 827 pH lab) equipped with a H^+ Ion Selective Electrode (ISE). The electrode was calibrated using buffers pH = 4 and pH = 7. Apparent pH values were measured by pH paper.

5.4.2 Representative NMR Spectra of cPPA Depolymerization in Lewis Acid Solutions

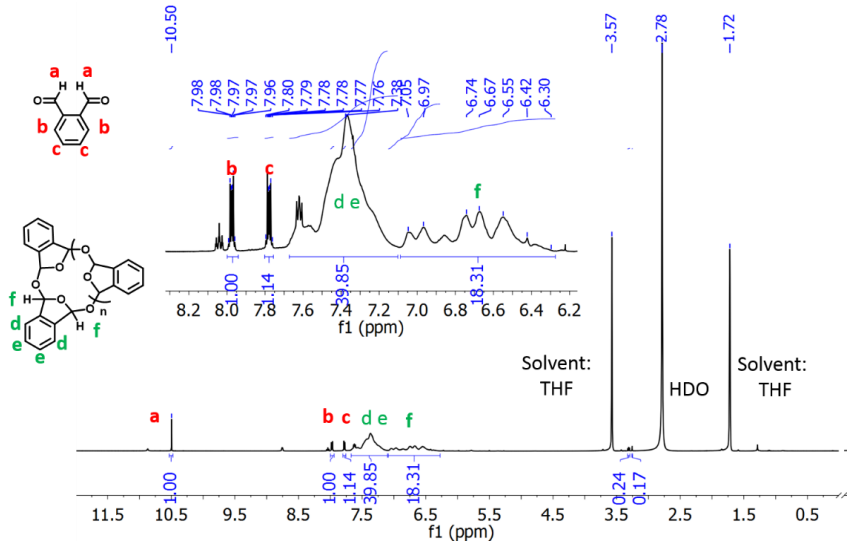

Figure 5.5. ^1H NMR spectra of cPPA (M_n=55 kDa, ~5mg/mL) depolymerization catalyzed by 0.01 M $ZnCl_2$ after 48 h. Solvent: THF-d_8.

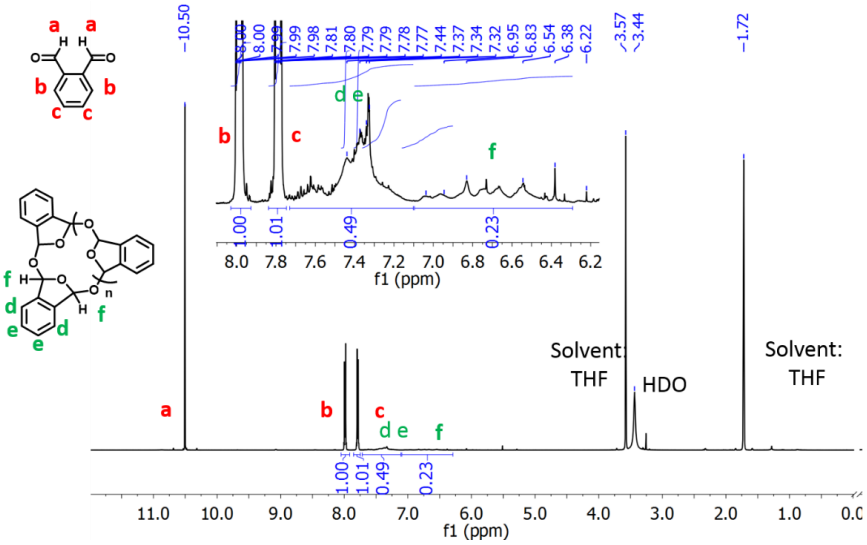

Figure 5.6. ^1H NMR spectra of cPPA (M_n=55 kDa, ~5mg/mL) depolymerization catalyzed by 0.01 M $ZnCl_2$ and co-activated by 0.1 M LiCl after 48 h. Solvent: THF-d_8.

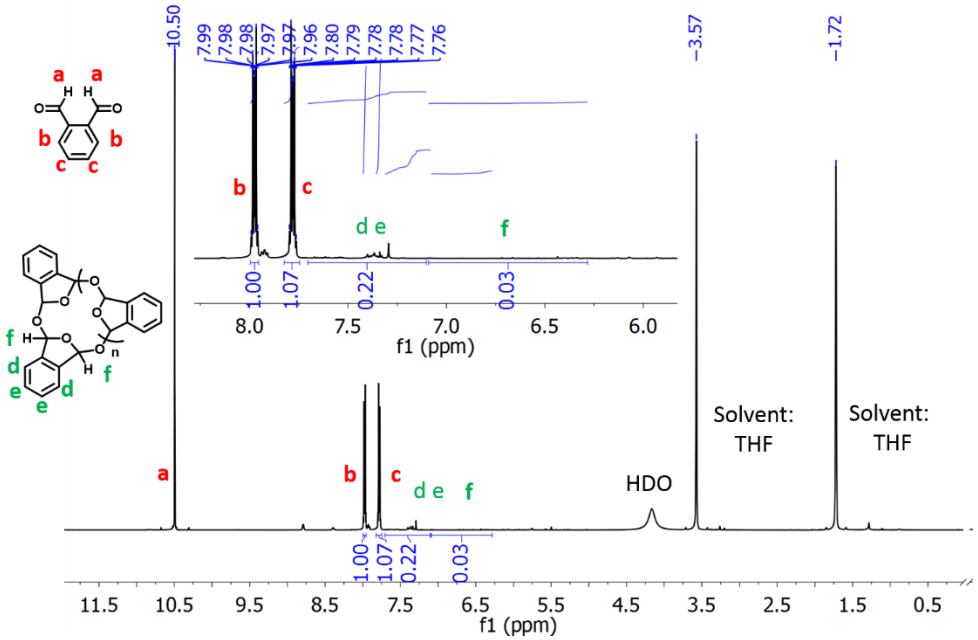

Figure 5.7. ^{1}H NMR spectra of cPPA (M_n=55 kDa, ~5mg/mL) depolymerization catalyzed by 0.01 M Zn(TFSI)$_2$ after 48 h. Solvent: THF-d_8.

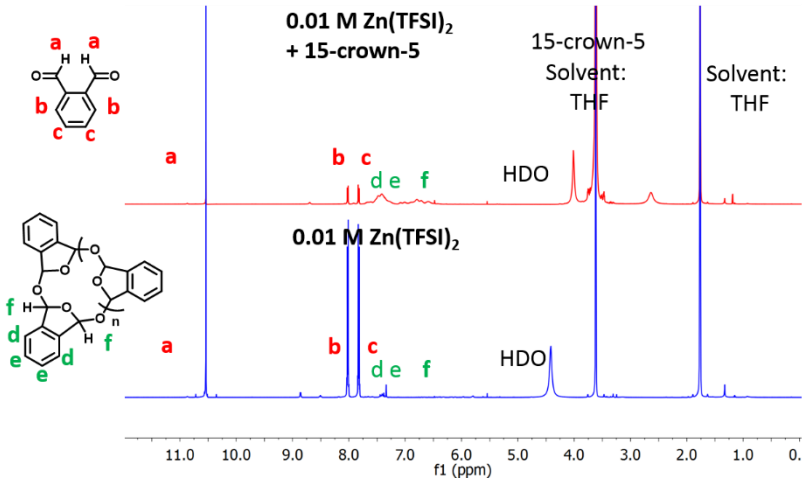

Figure 5.8. ^{1}H NMR spectra of cPPA (M_n=55 kDa, ~5mg/mL) depolymerization catalyzed by 0.01 M Zn(TFSI)$_2$ in THF-d_8 with or without crown ethers 15-crown-5 in the solutions at 48 h. Red trace represented a cPPA/THF solution containing both Lewis acids 0.01 M Zn(TFSI)$_2$ and 0.011 M 15-crown-4 to inhibit the Lewis acid catalysts by forming metal ion crown ether complexes. Blue trace represented a cPPA/THF solution containing Lewis acids 0.01 M Zn(TFSI)$_2$) and no crown ethers.

5.4.3 pH Measurement of Lewis Acid/THF Solutions

Table 5.2 pH Measurements of Lewis Acid/THF Solutions

Solutions	pH meter	Apparent pH
0.01 M LiCl	4.142	4
0.01 M LiCl+ 0.1 M LiCl	3.701	4
0.01 M LiTFSI	3.575	4
0.01 M $MgCl_2$	3.852	4
0.01 M $MgCl_2$ + 0.1 M LiCl	3.193	4
0.01 M $Mg(TFSI)_2$	0.064	4
0.01 M $ZnCl_2$	1.540	4
0.01 M $ZnCl_2$ + 0.1 M LiCl	3.726	4
0.01 M $Zn(TFSI)_2$	-3.479	4

5.5 REFERENCES

(1) Aso, C.; Tagami, S. Polymerization of Aromatic Aldehydes. III. The Cyclopolymerization of Phthalaldehyde and the Structure of the Polymer. *Macromolecules* **1969**, *3*, 414–419.

(2) Kaitz, J. A.; Diesendruck, C. E.; Moore, J. S. End Group Characterization of Poly(phthalaldehyde): Surprising Discovery of a Reversible, Cationic Macrocyclization Mechanism. *J. Am. Chem. Soc.* **2013**, *135*, 12755–12761.

(3) Schwartz, J. M.; Phillips, O.; Engler, A.; Sutlief, A.; Lee, J.; Kohl, P. A. Stable, High-Molecular-Weight Poly(phthalaldehyde). *J. Polym. Sci. Part A Polym. Chem.* **2017**, *55*, 1166–1172.

(4) Feinberg, A. M.; Hernandez, H. L.; Plantz, C. L.; Mejia, E. B.; Sottos, N. R.; White, S. R.; Moore, J. S. Cyclic Poly(phthalaldehyde): Thermoforming a Bulk Transient Material. *ACS Macro Lett.* **2018**, *7*, 47–52.

(5) Tsuda, M.; Hata, M.; Nishida, R.; Oikawa, S. Acid-Catalyzed Degradation Mechanism of Poly(phthalaldehyde): Unzipping Reaction of Chemical Amplification Resist. *J. Polym. Sci., Part A Polym. Chem.* **1997**, *35*, 77–89.

(6) Marcus, Y. *Ion Properties*; CRC Press, 1997; Vol. 1.

(7) Marcus, Y.; Kamlet, M. J.; Taft, R. W. Linear Solvation Energy Relationships: Standard Molar Gibbs Free Energies and Enthalpies of Transfer of Ions from Water into Nonaqueous Solvents. *J. Phys. Chem.* **1988**, *92*, 3613–3622.

(8) Pedersen, C. J. Cyclic Polyethers and Their Complexes with Metal Salts. *J. Am. Chem. Soc.* **1967**, *89*, 2495–2496.

(9) Yeung, K.; Kim, H.; Mohapatra, H.; Phillips, S. T. Surface-Accessible Detection Units in Self-Immolative Polymers Enable Translation of Selective Molecular Detection Events into Amplified Responses in Macroscopic, Solid-State Plastics. *J. Am. Chem. Soc.* **2015**, *137*, 5324–5327.

(10) DiLauro, A. M.; Robbins, J. S.; Phillips, S. T. Reproducible and Scalable Synthesis of End-Cap-Functionalized Depolymerizable Poly(phthalaldehydes). *Macromolecules* **2013**, *46*, 2963–2968.

(11) Kaitz, J. A.; Diesendruck, C. E.; Moore, J. S. End Group Characterization of Poly(phthalaldehyde): Surprising Discovery of a Reversible, Cationic Macrocyclization Mechanism. *J. Am. Chem. Soc.* **2013**, *135*, 12755–12761.

CHAPTER 6 : EFFORTS TOWARDS MECHANISMS OF SPECIFIC ION CO-ACTIVATION EFFECT ON TRANSIENT POLYMER MICROCAPSULES

6.1 INTRODUCTION

In Chapter 3 and Chapter 4, we investigated a specific ion co-activation effect (SICA) on cPPA microcapsules. From the ion specificity studies, we discovered that the ion co-activation effect is related to anion solvation properties, showing Hofmeister behavior. All investigated chaotropic anions (Cl^-, Br, NO_3^-, SCN^-, I^-, ClO_4^-) were found to co-activate cPPA depolymerization due to favorable anion-polymer interactions. As anions become less solvated from Cl^- to ClO_4^-, the co-activation effect decreased from Cl^- to NO_3^- and increased from SCN^- to ClO_4^-, showing a non-monotonic trend. This suggested that the SICA effect resulted from several contributions and the dominating mechanisms depended on the anion species. Similar non-monotonic trends were reported in previous literatures on specific anion-polymer interactions, where different anions were dominated by different types of interactions that modulated the polymer solubility in water.[1] For example, Zhang *et al*. reported specific anion-poly (*N*-isopropylacrylamide) (pNIPAM) interactions that modulated the lower critical solution temperatures (LCST) of pNIPAM based on three mechanisms.[1] Kosmotropic anions lowered the LCST by polarizing the hydration layers of the pNIPAM amide groups. Chaotropic anions such as Cl^- and Br^- lowered the LCST by increasing the surface tension and destabilizing the hydrophobic hydration layers of the pNIPAM backbones. Chaotropic anions such as SCN^- and ClO_4^- increased the LCST by directly binding to the amide groups which enhanced the solubility of pNIPAM.

Inspired by these interaction models, we considered the cPPA backbone structures and proposed two chaotropic anion-cPPA interaction models and mechanisms for their co-activation effect (Figure 6.1). In the first model, anions interact with cationic cPPA depolymerization intermediates *via* electrostatic interaction, which stabilizes the depolymerization intermediates and leads to the accelerated depolymerization rates (Figure 6.1, left). In the second model, anions associate with cPPA microcapsules/methanol solid/liquid interfaces *via* solvent assisted hydrophobic interaction.[2,3] The affinity of anions to the microcapsule's interfaces leads to the accelerated depolymerization rates (Figure 6.1, right). In this chapter, we studied the proposed models to probe the SICA effect mechanisms. To analyze the effect of anions on the cPPA depolymerization intermediates, we studied small molecule acetalization reactions of the monomer *o*-PA with methanol in different triggering solutions to mimic the effect of anions on the depolymerization intermediates. To understand the importance of the interfaces, we compared the SICA effect in homogeneous cPPA solutions and heterogeneous cPPA microcapsule's suspensions.

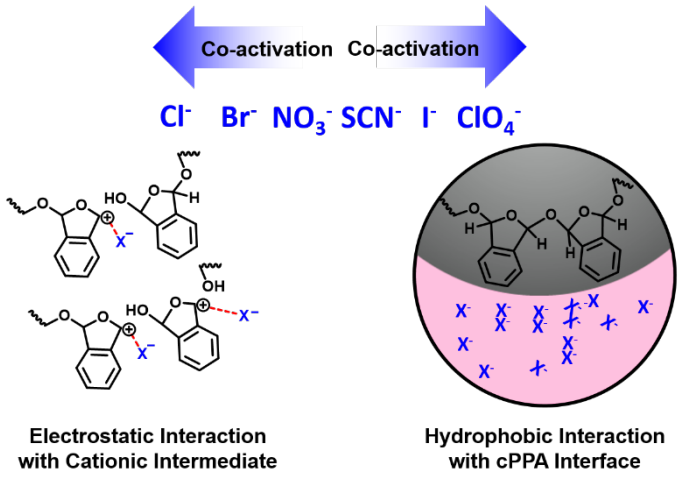

Figure 6.1.Proposed chaotropic anion-cPPA interaction models. (a) Electrostatic interactions between chaotropic anions and cPPA depolymerization intermediates (left). (b) Solvent assisted hydrophobic interactions between chaotropic anions and cPPA microcapsules/methanol (solid/liquid) interfaces (right).

6.2 SPECIFIC ION CO-ACTIVATION EFFECT IN HOMOGENEOUS AND HETEROGENEOUS SYSTEMS

To understand whether the existence of cPPA microcapsules/methanol (solid/liquid) interfaces affect the co-activation, we compared the cPPA depolymerization kinetic profiles in heterogeneous (cPPA microcapsules/methanol suspensions, solid/liquid interfaces) and homogeneous (cPPA/tetrahydrofuran (THF) solutions, no interfaces) systems (Figure 6.2). In heterogeneous systems, cPPA microcapsules (~5 mg/mL) were suspended in methanol-d_4 (black trace 0.01 M TFA, blue trace 0.01 M TFA + 1 M LiCl, red trace 0.01 M TFA + 1 M LiSCN) as shown in Chapter 3 and 4. In homogeneous systems, cPPA (M_n=55 kDa, PDI=1.6, ~5 mg/mL) was dissolved in THF-d_8 (no interfaces, black trace 0.01 M TFA, blue trace 0.01 M TFA + 1 M LiCl, red trace 0.01 M TFA + 1 M LiSCN) to form a solution. In homogeneous and heterogeneous systems, the co-activation effects of LiCl and LiSCN were found to be different. In both microcapsule's suspensions (heterogeneous) and cPPA solutions (homogeneous), LiCl accelerated the depolymerization rates regardless of the existence of the interfaces. This indicates that LiCl's co-activation does not rely on an interface. In contrast, LiSCN only accelerated the depolymerization rates in the heterogeneous microcapsule's suspensions. The less pronounced co-activation effect of LiSCN in homogeneous cPPA solutions suggests that LiSCN's co-activation is related to interfaces. The different co-activation effects in heterogeneous and homogeneous systems support the hypothesis that the co-activation effects of LiCl and LiSCN were dominated by different mechanisms resulted from different anion-polymer interactions.

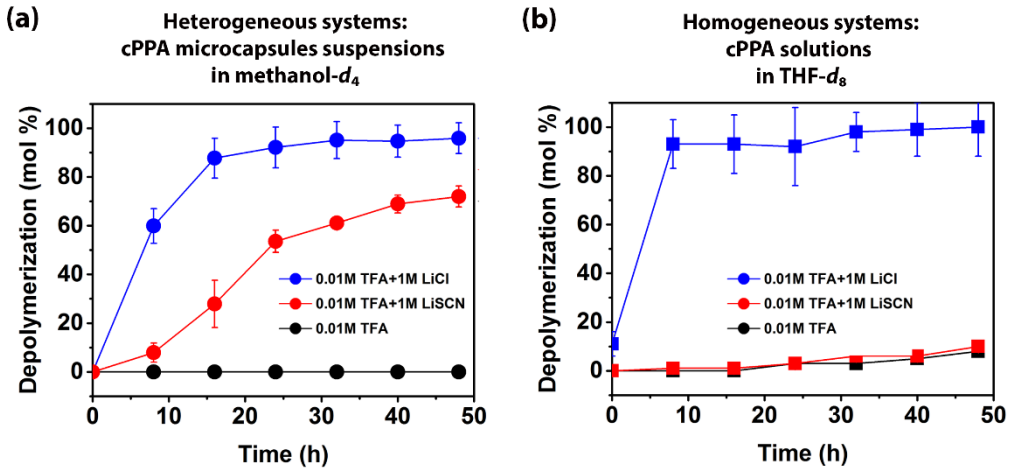

Figure 6.2. cPPA depolymerization profiles in heterogeneous and homogeneous systems. (a) cPPA depolymerization profiles in heterogeneous systems (replot from Chapter 4): cPPA microcapsule's suspensions in methanol-d_4 (~5 mg/mL). The triggering solutions contain 0.01 M TFA (black), 0.01 M TFA + 1 M LiCl (blue) or 0.01 M TFA + 1 M LiSCN (red). (b) cPPA depolymerization profiles in homogeneous systems: cPPA solutions in THF-d_8 (~5 mg/mL). The triggering solutions contain 0.01 M TFA (black), 0.01 M TFA + 1 M LiCl (blue) or 0.01 M TFA + 1 M LiSCN (red).

Intrigued by the observation above, we further compared the co-activation effects of other chaotropic anions in the heterogeneous and homogeneous systems to determine the anion species whose co-activations are related to interfaces (Figure 6.3). The co-activation effects were represented by the depolymerization mol % at 16 h, and a higher depolymerization percentage indicated an increased co-activation effect. In heterogeneous systems (Figure 6.3a), all examined chaotropic anions resulted in accelerated depolymerization rates, showing co-activation effects. In homogeneous systems (Figure 6.3b), LiCl, LiBr, and $LiClO_4$ co-activated the cPPA depolymerization, but $LiNO_3$, LiSCN, and LiI led to much less pronounced co-activation effects. This indicates that the co-activation effects of $LiNO_3$, LiSCN and LiI are related to the cPPA microcapsule's interfaces. We explain that the dependence on the interface derives from these anions (i.e. SCN^-) are more hydrophobic (than i.e. Cl^- and Br^-) and have greater affinities to the

hydrophobic cPPA microcapsule's interfaces.[4] The anions at cPPA interfaces could attract hydronium ions and lead to decreased interfacial pH values that accelerate the depolymerization rates. [5,6] Another possibility is that the anions at the interfaces have a plasticizing effect on the shell walls, which cause a faster diffusion of payloads across the shell walls.[1] And these contributions at the interfaces may result in the co-activation effect of $LiNO_3$, LiSCN and LiI.

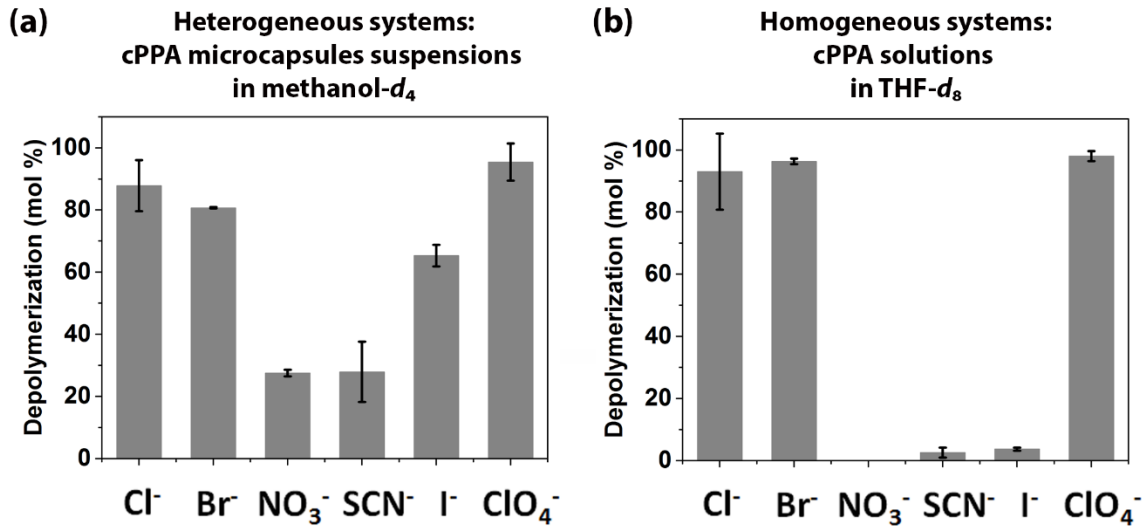

Figure 6.3. Comparison of the SICA effect in heterogeneous and homogeneous systems (a) The SICA effect in heterogeneous systems (replot from Chapter 4): cPPA microcapsule's suspensions in methanol-d_4 (~5 mg/mL). The triggering solutions contain 0.01 M TFA and 1 M lithium salts with different anions. (b) The SICA effect in homogeneous systems: cPPA solutions in THF-d_8 (~ 5 mg/mL). The triggering solutions contain 0.01 M TFA and 1 M lithium salts with different anions. In both systems, the SICA effect was evaluated by the depolymerization mol % at 16 h. A higher depolymerization mol% indicated an increased co-activation effect. Note: Saturated solution was used for LiSCN/THF solution due to its low solubility.

6.3 PROBE CO-ACTIVATION EFFECT ON DEPOLYMERIZATION INTERMEDIATES

To test the effect of anions on the cationic cPPA depolymerization intermediates, the acid catalyzed acetalization reactions of the monomer *o*-PA with methanol was used as a mimic reaction because the depolymerization intermediates of cPPA were similar in structures to the

intermediates generated during the formation of *o*-PA acetals as shown in Figure 6.4. To elucidate the effect of anions on the reaction energy profiles, we monitored the kinetics of acetal formation in the presence and absence of co-activators by NMR spectroscopy.

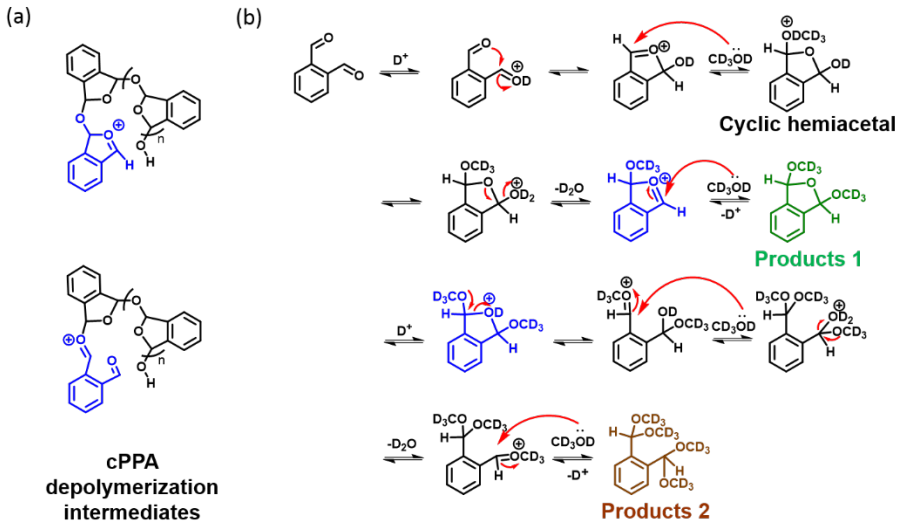

Figure 6.4. (a) cPPA depolymerization cationic intermediates. (b) Acid catalyzed formation of o-PA acetals in deuterated methanol. Note: Stereoisomers for Product 1 and cyclic hemiacetals were not illustrated here.

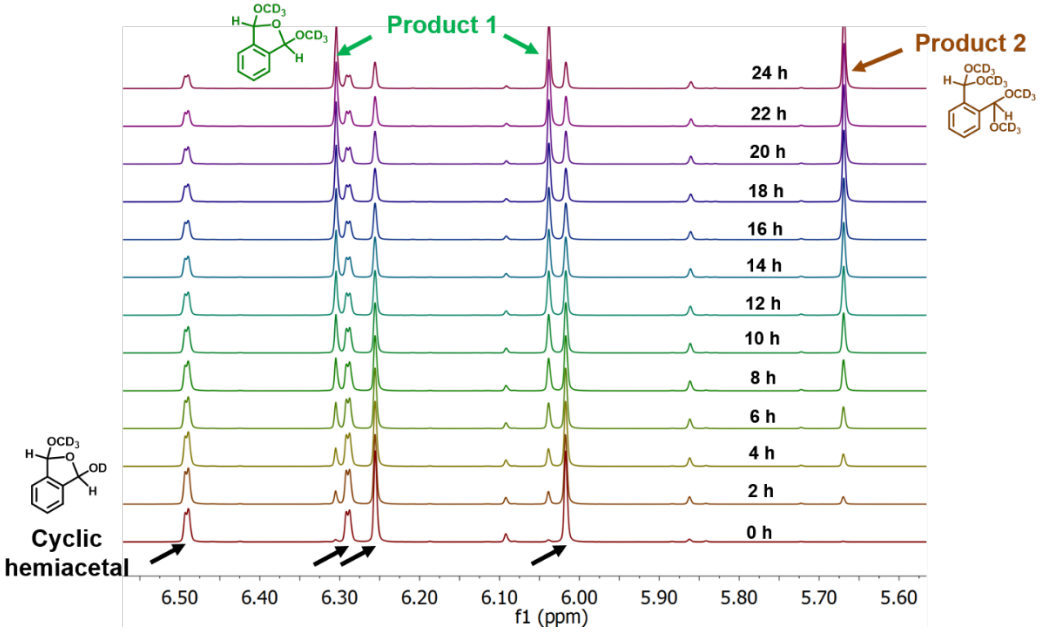

Figure 6.5. Representative time sequenced ^{1}H NMR spectra of o-PA (~25 mg/mL, 0.18 M) acetalization reactions catalyzed by TFA (1 mM in methanol-d_4). ^{1}H NMR spectra were collected immediately after dissolving o-PA in the triggering solutions. Only small amounts of o-PA remained in the first ^{1}H NMR spectra, and the majority of the starting materials are cyclic

Figure 6.5. (cont.) hemiacetals (black arrows). Consumption rates of the hemiacetals were calculated by comparing the molarity of hemiacetals with the total molarities of all types of acetals (product 1, product 2, and hemiacetals) and remained o-PA.

To examine the kinetics of the model small molecule reaction, starting materials *o*-PA (~25 mg/mL, 0.18 M) was dissolved in methanol-d_4 containing 1 mM TFA (salt-free) to form a homogeneous solution (Figure 6.5). Immediately after the mixing, time-dependent NMR spectra were collected every 2 h (over 24 h) to monitor the conversion of *o*-PA to Product 1 and 2. The majority of the starting material *o*-PA was found readily converted to cyclic hemiacetals in the first collected NMR spectra (Figure 6.5, arrow, 0 h). Therefore, we monitored the reaction kinetics by calculating the consumption of the cyclic hemiacetals, which was determined by comparing the molarity of cyclic hemiacetals with the total molarities of all types of acetals (product 1, product 2, and cyclic hemiacetals) and remained *o*-PA. The kinetic profiles in different triggering solutions, 1 mM TFA (red), 1 mM TFA + 10 mM LiCl (blue), and 1 mM TFA + 10 mM LiSCN (green), were compared in Figure 6.6a. Apparently, the addition of LiCl in the acidic solutions accelerated the consumption of the cyclic hemiacetals (blue) compared with the kinetics in salt-free acidic solutions (red) and acidic solutions with LiSCN (green). A control study was performed to monitor the conversion of cyclic hemiacetals in acid-free ionic solutions (Figure 6.6b). In both acid-free 10 mM LiCl solutions (blue circles) or acid-free 10 mM LiSCN solutions (green circles), less than 5 mol % hemiacetals were consumed, indicating a much slower reaction kinetics without acid catalysts and both LiCl and LiSCN did not affect the reaction kinetics intrinsically. These results are also consistent with the results discussed in 6.2, where LiCl and LiSCN showed different co-activation behaviors in homogeneous solutions. Observation of a co-activation effect in forming the small molecule acetals indicated that LiCl's co-activation on cPPA is possibly related to stabilizing the intermediates in the reaction kinetics.

On the contrary, the presence of LiSCN did not accelerate the reactions. This was expected because the co-activation effect of LiSCN is hypothesized to rely on the interfaces. [2,7]

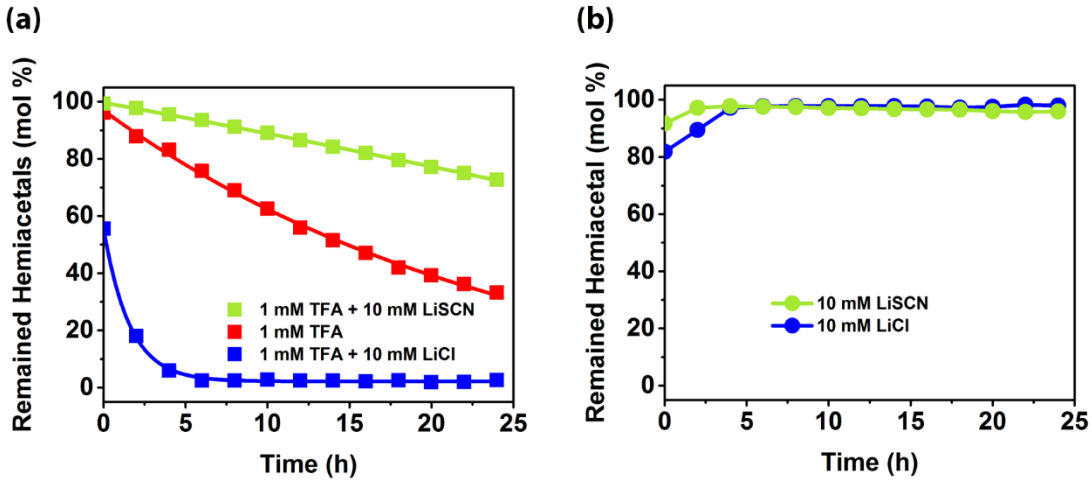

Figure 6.6. Kinetic profiles of hemiacetals consumption in varied triggering solutions. (a) Hemiacetals consumption profiles in 1 mM TFA (red), 1 mM TFA + 10 mM LiCl (blue), 1 mM TFA + 10 mM LiSCN (green), solvent: methanol-d_4. (b) Hemiacetals consumption profiles in 10 mM LiCl (blue, acid-free) and 10 mM LiSCN (green, acid-free), solvent: methanol-d_4. Consumption rates of the hemiacetals were calculated by comparing the molarity of hemiacetals with the total molarities of all types of acetals (Product 1, Product 2, and hemiacetals) and remained o-PA. The data plots in (a) were fitted with an exponential decay model.

We further hypothesize that the LiCl's co-activation effect on cPPA is a result of chloride anion interacts with the degradation cationic intermediates by electrostatic interactions which stabilize the intermediates involved in the initial ring opening. This step was proved to be the rate limiting step in cPPA chain unzipping pathway in a previous computational study.[8] Because the intermediates generated during the conversion from Product 1 to Product 2 have a similar structure with the cPPA depolymerization intermediates generated during the ring opening step (Figure 6.7b), we probed the effect of LiCl on this rate limiting step by monitoring the conversion kinetics of Product 1 to Product 2 in different triggering solutions: 1 mM TFA (red), 1 mM TFA + 10 mM LiCl (blue), and 1 mM TFA + 10 mM LiSCN (green) (Figure 6.8). The addition of LiCl in the acidic solutions (blue) accelerated the conversion of Product 1 to Product

2 compared with the kinetics in salt-free acidic solutions (red). Observation of a co-activation effect in forming the small molecule acetals indicated that LiCl's co-activation on cPPA is possibly related to stabilizing the intermediates in the reaction kinetics. In comparison, acidic LiSCN solutions did not show acceleration effect on this kinetics study (green). This indicated that LiSCN and LiCl affected cPPA depolymerization in different mechanisms.

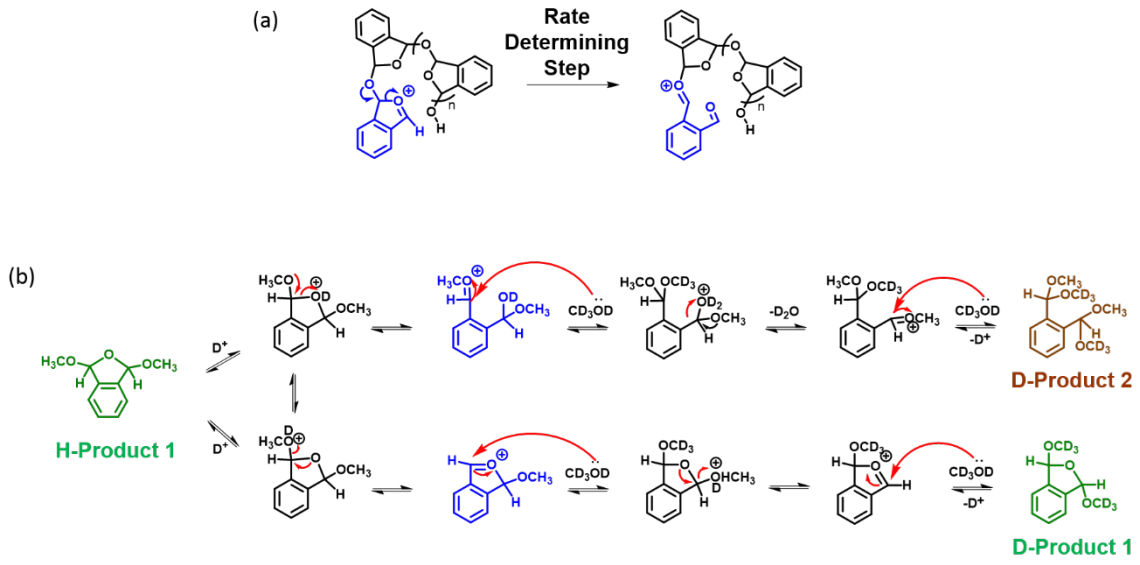

Figure 6.7. (a) Rate limiting step of cPPA depolymerization: initial ring opening. (b) Acid catalyzed conversion of Product 1 to Product 2 which mimics the ring opening step. Note: Stereoisomers for Product 1 and cyclic hemiacetals were not illustrated here.

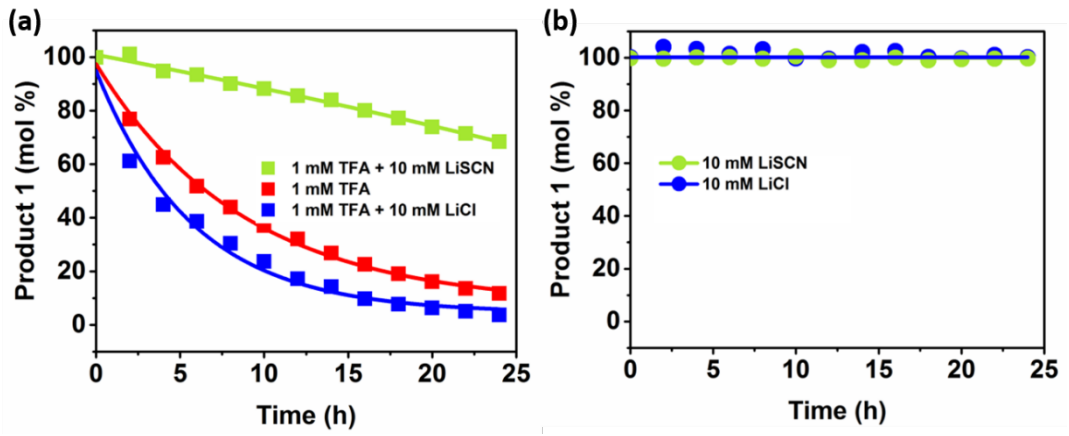

Figure 6.8. Kinetic profiles of Product 1 consumption in varied triggering solutions. (a) Product 1 consumption profiles in 1 mM TFA (red), 1 mM TFA + 10 mM LiCl (blue), 1 mM TFA + 10 mM LiSCN (green), solvent: methanol-d_4. (b) Product 1 consumption profiles in 10 mM LiCl (blue, acid-free) and 10 mM LiSCN (green, acid-free), solvent: methanol-d_4. Consumption rates of the Product 1 were calculated by comparing the molarity of hemiacetals with the total molarities of all types of acetals (Product 1, Product 2, and hemiacetals) and remained o-PA. The data plots in (a) were fitted with an exponential decay model.

6.4 SUMMARY: PROPOSED APPROACHES TO ASSIGN MULTI-SCALE CONTRIBUTIONS IN THE SPECIFIC ION CO-ACTIVATION EFFECT

So far, we have demonstrated that the SICA effect is contributed by multiple factors. Possible contributions include changes in the bulk solutions induced by addition of salts, interfaces of microcapsules and ionic effect on molecular level depolymerization pathway. This session will propose experimental approaches to examine and assign the contributions at each level.

6.4.1 Contribution of Bulk Solutions

Mixing salts in acidic solutions can cause changes in acidities and polarities in the bulk solutions. Therefore,

$$D_{Bulk} = D_{pH\ Bulk} + D_{polarity\,bulk} \quad 6.1$$

To extract the contribution of acid in the depolymerization, in Figure 3.11, we have shown an acid concentration dependent model using cPPA depolymerization profiles in different concentrations of TFA. Plotting depolymerization (mol %) in TFA solutions against the corresponding solution pH value, a sigmoidal shaped relationship will be established.

$$D_{pH\ Bulk}(mol\%) = \frac{D_{\min} - D_{\max}}{1 + (\frac{pH}{pH_{D=50}})^{n}} + D_{\max}$$

where D_{min} is the depolymerization mol % at 16 h at the highest pH values (lowest acid concentration), D_{max} is the depolymerization mol % at 16 h in the solution with the lowest pH values (highest acid concentration). And n is order exponent. $pH_{D=50}$ is the pH value of the solution with depolymerization (mol %) =50 mol % at 16 h. And pH is the bulk solvent pH values measured by pH meter. Using this model, we can determine the depolymerization percentage contributed by the bulk solvent at different pH levels.

The contributions of solvent polarity change can be probed by the encapsulant, Nile red, which is known as an indicator of polarity by the shift of emission spectrum.[17] Polarity contributions can be tested by measuring the shift of max emission with increasing concentration of salts. The excitation spectrum was obtained from the payload release profiles. In preliminary tests, we collected the emission spectrums in different salt concentrations and compared their maximum emission wavelength. The resulting peak wavelengths shifted less than 3 nm for all the ionic solutions, indicating that the polarity changes are negligible.

6.4.2 Contribution of Interfaces

After deducting the contribution of acidities, to extract the contribution of interfaces, we have compared cPPA depolymerization kinetic profiles in heterogeneous (cPPA microcapsules/methanol suspensions, solid/liquid interfaces) and homogeneous

(cPPA/tetrahydrofuran solutions, no interfaces) systems (Figure 6.2). As discussed in 6.2, NO_3^-, SCN^-, I^- showed much less pronounced SICA effect, indicating that the accelerated depolymerization was likely only contributed by the existence of an interface, which was originated from the hydrophobicity of these anions. Several changes are expected due to hydrophobicity, including surface pH changes, surface polarity changes, solvation and plasticizing effect. Surface pH and surface polarity changes are characterized by *in situ* fluorescence imaging. pH indicators and polarity indicators can be encapsulated in the microcapsules and the dye trapped in the shell wall is used to monitor the environment changes at the interface. Solvation and plasticizing effect can be probed by measuring release profiles of microcapsules in acid-free salt solutions and use release profiles in acid-free salt-free solutions as a control study. The payload release is driven by diffusion only and is used to determine the shell wall barrier properties to reflect the anion solvation and plasticizing effect.

6.4.3 Contributions at the Molecular Level

The small molecule model used in 6.3 suggested that Cl^- affect the depolymerization at a molecular level by interacting with the depolymerization intermediates. It will be valuable to see computation results using *o*-PA as the model molecule and calculate the energy landscape in these small molecule acetals with or without the presence of chloride. One step forward is to use a 3 or 4-monomer oligomer and examine the depolymerization kinetics of cPPA from *ab initio* computation.[16]

Another possible mechanism of LiCl's co-activation is that the anion-polymer interactions altered the depolymerization pathway by inhibiting the nucleophilic solvents to capture the cationic intermediates. When the depolymerization intermediates are captured by solvent molecules, the depolymerization proceeds through a step-wise manner instead of a

domino-like manner.[11] If the Cl^- inhibits the solvent capture, a step-wise pathway will be shifted to an unzipping pathway in LiCl solution. Monitoring the production of *o*-PA (by NMR) and the reduction of cPPA molecular weight (by GPC) during the depolymerization will be useful to understand the effect of anions on these pathways.

6.5 EXPERIMENTAL DETAILS

Unless otherwise noted, all chemicals were obtained from Sigma Aldrich and used as received. The monomer *o*-PA (98%, Alfa-Aesar) was purified by hot filtration followed by a single recrystallization according to a literature procedure.[9] DCM was obtained from an anhydrous solvent delivery system equipped with activated alumina columns. All glassware for polymerization was oven dried prior to use. The synthesis of cPPA (M_n=55 kDa, PDI=1.6) followed previous literature procedures with minor modifications.[10]

The molecular weight of cPPA was determined by an analytical gel permeation chromatograph (GPC) analyses were performed with a Waters1515 Isocratic HPLC pump, a Waters (2998) Photodiode Array Detector, a Waters (2414) Refractive Index Detector, a Waters (2707) 96-well autosampler, and a series of 4 Waters HR Styragel 3wcolumns (7.8 x 300mm, HR1, HR3, HR4, and HR5) in THF at 30 °C.

NMR spectra were recorded using a Bruker 500 MHz spectrometer with broad-band CryoProbe and automation. Chemical shifts were reported in δ (ppm) relative to the residual solvent peak methanol-d_4 (3.31 ppm) and THF-d_8 (1.72 ppm). The depolymerization profiles of microcapsule's suspensions were reproduced from Chapter 3 and 4. Depolymerization mol % at 16 h for different anions were extracted from Chapter 3 and 4. The depolymerization mol % in cPPA homogeneous solutions were measured *in situ* after 48 h treatment, and the quantification was determined by comparing the integration of the depolymerization products peaks (*o*-PA,

aromatic protons, 4 H, 7.77-8.00 ppm) over the integration of the remained cPPA polymer peaks (acetal protons, 2 H, 6.30-7.15 ppm).

6.6 REFERENCES

(1) Zhang, Y. J.; Furyk, S.; Bergbreiter, D. E.; Cremer, P. S. Specific Ion Effectis on the Water Solubility of Acromolecules: PNIPAM and the Hofmeister Series. *J. Am. Chem. Soc.* **2005**, *127*, 14505–14510.

(2) Lund, M.; Vrbka, L.; Jungwirth, P. Specific Ion Binding to Nonpolar Surface Patches of Proteins. *J. Am. Chem. Soc.* **2008**, *130*, 11582–11583.

(3) Marcus, Y. *Ion Properties*; CRC Press, 1997; Vol. 1.

(4) Lo Nostro, P.; Ninham, B. W. Hofmeister Phenomena: An Update on Ion Specificity in Biology. *Chem. Rev.* **2012**, *112*, 2286–2322.

(5) Salis, A.; Ninham, B. W. Models and Mechanisms of Hofmeister Effects in Electrolyte Solutions, and Colloid and Protein Systems Revisited. *Chem. Soc. Rev.* **2014**, *43*, 7358–7377.

(6) Yang, Z. Hofmeister Effects: An Explanation for the Impact of Ionic Liquids on Biocatalysis. *J. Biotechnol.* **2009**, *144*, 12–22.

(7) Lund, M.; Vácha, R.; Jongwirth, P. Specific Ion Binding to Macromolecules: Effects of Hydrophobicity and Ion Pairing. *Langmuir* **2008**, *24*, 3387–3391.

(8) Tsuda, M.; Hata, M.; Nishida, R.; Oikawa, S. Acid-Catalyzed Degradation Mechanism of Poly(Phthalaldehyde): Unzipping Reaction of Chemical Amplification Resist. *J. Polym. Sci., Part A Polym. Chem.* **1997**, *35*, 77–89.

(9) DiLauro, A. M.; Robbins, J. S.; Phillips, S. T. Reproducible and Scalable Synthesis of End-Cap-Functionalized Depolymerizable Poly(Phthalaldehydes). *Macromolecules* **2013**, *46*, 2963–2968.

(10) Kaitz, J. A.; Diesendruck, C. E.; Moore, J. S. End Group Characterization of Poly(Phthalaldehyde): Surprising Discovery of a Reversible, Cationic Macrocyclization Mechanism. *J. Am. Chem. Soc.* **2013**, *135*, 12755–12761.

(11) Feinberg, A. F.; Moore, J. S. Unpublished results

CHAPTER 7 : OUTLOOK: HOFMEISTER EFFECT ON MACROMOLECULES AND POTENTIAL APPLICATIONS IN AUTOCATALYTIC PAYLOAD RELEASE FROM TRANSIENT POLYMER MICROCAPSULES

7.1 MOTIVATION

In Chapter 3 to Chapter 6, we have introduced the concept of SICA on cPPA microcapsules, which is useful for controlling the depolymerization and payload release kinetics. We have concluded in Chapter 3 and 4 that this SICA effect is related to anion solvation behavior. In Chapter 6, mechanism studies have shown that the SICA effect on cPPA depolymerization is potentially contributed by multi-scale factors: an electrostatic interaction that mediates the depolymerization kinetics at a molecular level (Cl^-) and an anion-cPPA shell wall hydrophobic interaction that affects the depolymerization kinetics at an interfacial level (SCN^-). The aim of this chapter is to expand considerations on the SICA effect of the cPPA microcapsules, understand theoretical approaches to illustrate SICA effect molecular level mechanisms, and propose crude models for developing autocatalytic payload release based on the cPPA microcapsules and the SICA effect.

7.2 CURRENT STATE OF HOFMEISTER EFFECT

Univalent ions result in specific changes in electrolyte solutions, colloids, surfactants, emulsions, and polymer/protein solubility, known as the Hofmeister series.[1–3] The specific ion effects modulate material's properties *via* non-covalent interactions, which offer convenient and reversible routes to achieve environmental responsive materials. Experimental and computational studies have devoted to understand mechanisms of the Hofmeister series, whereas their molecular level origin is still in debate. Different from the classical Debye–Hückel and Derjaguin-Landau-Verwey-Overbeek (DLVO) theory where the electrostatic interactions were considered, the specific ion effect is contributed by ion geometry, solvation behavior and

dispersion force. It has been recognized that these contributions either compensate or contradict with each other, resulting in ion specific behavior.[2]

7.2.1 Hofmeister Effect in Organic Solvents

The ion specific hydration behavior is one of the contributions accounted for the Hofmeister effect. It raises the question whether the Hofmeister behavior exists in non-aqueous or mixed solvents. Several studies have investigated the specific ion effect on pNIPAM solubility in alcohol-water mixed solutions.[4-6] As the molar fraction of methanol increases in the methanol-water solvent mixture, the LCST of pNIPAM decreases first and then increases, known as the reentrant behavior.[7] It is hypothesized that the reentrant behavior was caused by the formation of solvent complexes, which reduce the accessibility of water molecules for the solute pNIPAM. It was found that the minimum value of LCST (transition point) for a solvent mixture is dependent on the anions in the solution. Wang *et al*. have found SCN^- and ClO_4^- depressed the reentrant behavior (increasing minimum LCST), while Cl^-, Br^-, and NO_3^- enhanced the reentrant behavior (decreasing minimum LCST). They accounted the ion specific reentrant behavior to the effect of ions on the solvent complexes (Figure 7.1). SCN^- and ClO_4^- broke the methanol-water complexes, thereby increasing the accessibility of water molecules to pNIPAM and its solubility. In contrast, Cl^-, Br^-, and NO_3^- did not affect the formation of solvent complexes. In another study, Xu *et al*. investigated ion specific pNIPAM solubility in mixed solvents of water and different polyhydric alcohols.[5] Ion specific effect was found to be amplified in alcohols that require more water molecules for alcohol hydrophobic solvation or can form stronger intermolecular hydrogen bonding with water (Figure 7.2). Similarly, this was attributed to the effect of ions on the formation of water-solvent complexes.

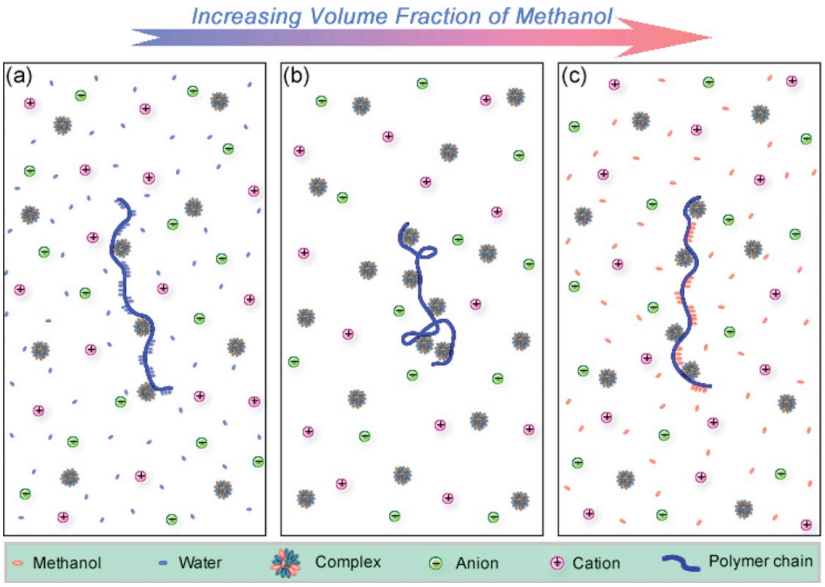

Figure 7.1. Schematic illustration of pNIPAM solvation behavior in (a) water, (b) water-methanol complexes, and (c) methanol. Reprinted with permission from reference[7] Copyright © 2012 American Chemical Society.

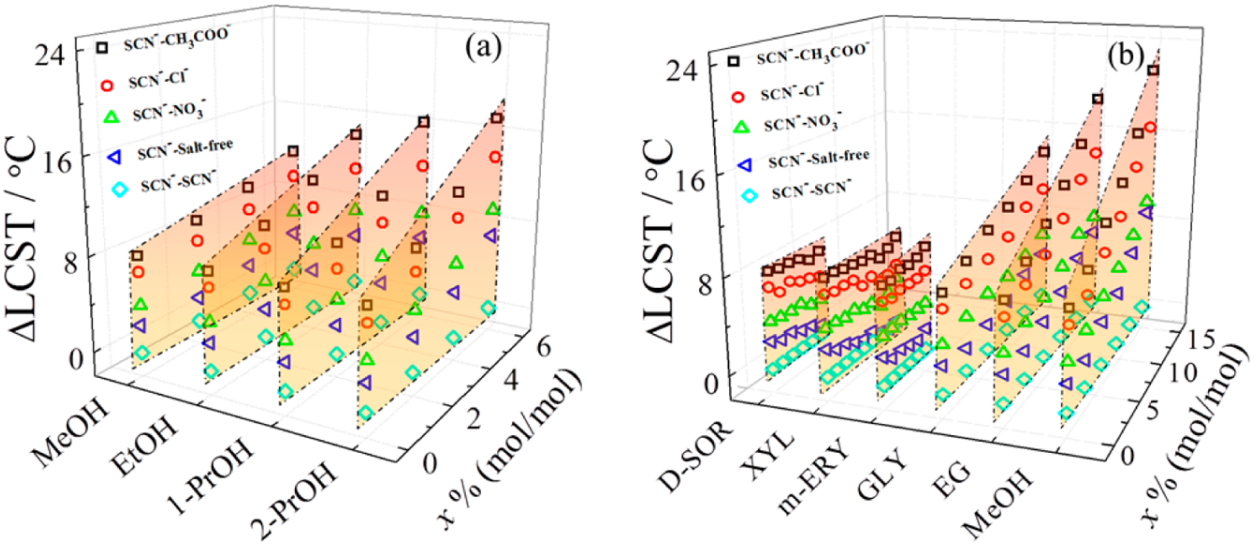

Figure 7.2. Ion specific LCST of pNIPAM in different alcohol solutions. (a) The ion specific LCST was amplified in the order of MeOH<EtOH<1-PrOH<2-PrOH, as the number of water molecules required for the hydrophobic hydration of alcohols increases. (b)The ion specific LCST of pNIPAM was amplified in the order of MeOH<ethylene glycol<glycerol<meso-erythritol<xylitol<D-sorbitol, as the tendency of forming intermolecular hydrogen bonding decreases. Na^+ is the common cation. Reprinted with permission from reference[5]. Copyright © 2014 American Chemical Society.

7.2.2 Simulation Studies in the Hofmeister Effect

To understand the molecular level mechanisms, molecular dynamics (MD) simulations have been adapted in several studies to understand the ion-(bio)molecule and ion-polymer interactions.[8–11] Four types of interactions are generally considered to contribute to the ion specific effect: (1) Coulomb and Lennard-Jones interactions; (2) short range dispersion or London type forces; (3) solvent assisted hydrophobic interactions; (4) ion pairing or Law of Water Matching Affinity. Currently, it is still challenging to differentiate these contributions *via* simulation approach. Nevertheless, physical insights of ion-(bio)molecule affinity and ion distribution are obtained in MD simulation by constructing two coarse-grained models, with charged groups exposed or buried in the nonpolar surfaces.[12] Ion distribution on the (bio)molecules was calculated by *g(r)* (Figure 7.3). In several studies, Cl^- and F^- were found to locate primarily around charged groups. And SCN^- was found distributed around nonpolar groups. [9,11–15]

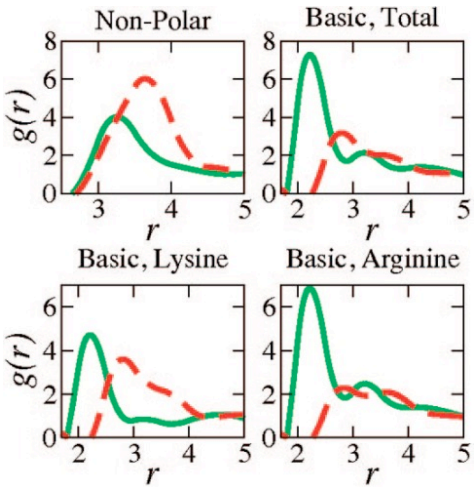

Figure 7.3. Radial distribution of Cl^- (green) and I^- (red) around basic (cationic) and nonpolar groups on Lysozyme. Reprinted with permission from reference [12]. Copyright © 2008 American Chemical Society)

7.3 MODELS FOR AUTOCATALYTIC PAYLOAD RELEASE FROM TRANSIENT POLYMER MICROCAPSULES

Understanding the co-activation effect will introduce a new type of microcapsule system capable of self-catalyzing its payload release. The payload amplification can be initiated by breaking few microcapsules and the released payloads further trigger the shell wall disassembly and delivery of payloads. This type of auto-acceleration microcapsules can be achieved by encapsulating the co-activators (ionic compounds). To estimate the critical encapsulation parameters and probe the feasibility of this system, in this chapter, important parameters are analyzed for modeling a self-catalyzed microcapsule system. Two scenarios are considered: (a) diffusion rate of the ionic compound in the bulk solution is much faster than the payload release rate from microcapsules ($D_{\text{ion-solvent}} \gg D_{\text{ion-μc}}$, bulk solution trigger); (b) diffusion rate of the ionic compound is much slower than the payload release rate ($D_{\text{ion-solvent}} \ll D_{\text{ion-μc}}$, flow trigger).

We define, *R(t)* is payload (salts) released in the medium that contributes to co-activation, normalized to [0, 100]. For both scenarios, an equation describing the relation of payload release half-life and salt concentration (in bulk solution) is needed as a calibration curve. For the calibration, cPPA microcapsules (no co-activators encapsulated) are suspended in an acidic medium containing different concentrations of salts. We assume the initial acid concentration A_0 remains constant during the payload release. This relation can be obtained by plotting payload release half-life $t'_{R_{50}}$ against triggering solutions of varied salt concentration *S*.

$$t'_{R_{50}} = F(A_0, S) \qquad 7.1$$

The payload release half-life is obtained by data fitting as shown in Chapter 3 and 4,

$$R(t) = \frac{R_0 - R_f}{1 + (\frac{t}{t'_{R_{50}}})^n} + R_f \qquad 7.2$$

where R_0 is release % at t = 0 h, R_f is release % at $t = \infty$, and n is order exponent. $t'_{R_{50}}$ is the apparent release half-life, corresponding to where $R(t) = \frac{R_f - R_0}{2}$. For simplification, we only use apparent release half-life $t'_{R_{50}}$ in the models.

For autocatalytic payload release systems, cPPA microcapsules encapsulated with salts were suspended in an acidic solvent medium containing acid concentration A_0 and salt concentration S_0. The acid concentration remains constant over time, while the salt concentration is a function of time, so

$$t'_{R_{50}} = F(A_0, S(t)) \qquad 7.3$$

To obtain the payload release equation in the autocatalytic payload release system, it is essential to solve *S(t)* for each scenario.

7.3.1 Autocatalytic Payload Release Triggered by Co-Activators in the Bulk Solutions ($D_{\text{ion-solvent}} \gg D_{\text{ion-μc}}$)

First we analyze the scenario where diffusion rate of the ionic compound in the bulk solvent is much faster than the diffusion rate of the payload across the shell walls ($D_{\text{ion-solvent}} \gg D_{\text{ion-μc}}$). This scenario is a simple extension based on the investigated system in Chapter 3 and 4, where the co-activation is a bulk solution trigger. Here we need to account for the increasing co-activator concentrations released from the microcapsules.

The real time salt concentration *S(t)* is dependent on the initial salt concentration in the bulk solvent (S_0), ultimate salt concentration when all payloads are released (*X)* and the released percentage at a certain time point, *R(t),*

$$S(t) = S_0 + R(t)X \qquad 7.4$$

Apparently, X is dependent on the composition of individual microcapsule and the microcapsules suspensions:

$$X = \frac{mL}{MW_{salts}V} \qquad 7.5$$

where, m (mg) is the mass of microcapsules suspended in the medium, L is the loading percentage of salts inside the microcapsules (wt %), and V (mL) is the volume of solution medium, MW_{salts} (g/mol) is the molecular weight of salts.

Therefore,

$$S(t) = S_0 + \frac{R(t)mL}{MW_{salts}V} \qquad 7.6$$

Substitute equation 7.4 into 7.3, then

$$t'_{R_{50}} = F(A, S_0 + R(t)X) \qquad 7.7$$

So the payload release profiles for this scenario is,

$$R(t) = \frac{R_0 - R_f}{1 + (\frac{t}{F(A_0, S_0 + R(t)X)})^n} + R_f = \frac{R_0 - R_f}{1 + (\frac{t}{F(A_0, S_o + R(t)\frac{mL}{MW_{salts}V})})^n} + R_f \qquad 7.8$$

Reorganizing *R(t)* to the left, then *R(t)* is determined by A_0, S_0, m, L, MW_{salts}, V, indicating a high concentration of microcapsules suspension, a high loading efficiency of salts and a low molar mass ionic compound as encapsulant favors a faster payload release rate in this auto-acceleration model.

7.3.2 Autocatalytic Payload Release Triggered by a Flow of Co-Activators ($D_{\text{ion-solvent}} \ll D_{\text{ion-}\mu c}$).

Next we consider the scenario where diffusion rate of the ionic compound in the bulk solution is much slower than the diffusion rate of the payload across the shell walls ($D_{\text{ion-solvent}} \ll D_{\text{ion-}\mu c}$). Similarly, a calibration equation is needed as we described in 7.3.1.

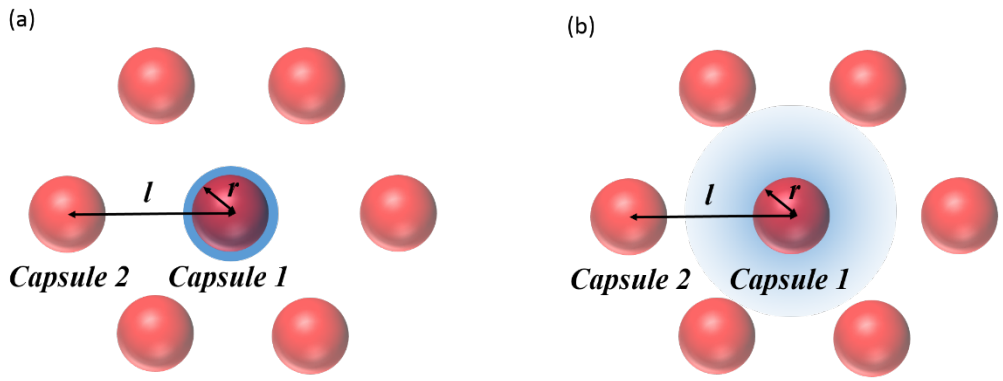

Figure 7.4. Schematic illustration of auto-catalytic microcapsules triggered by a flow of co-activators.

A typical system in this scenario is suspending microcapsules in viscous medium, such as glycerol. We assume the triggering solution (acid A_0, salt S_0) is introduced in only one individual microcapsule, as the "initiator microcapsule" ***Capsule 1*** (Figure 7.4a). In this scenario, the release is two stage, stage 1 is ***Capsule 1*** release ionic compound and self-catalyze. Since $D_{\text{ion-solvent}} \ll D_{\text{ion-μc}}$, for ***Capsule 1***, the autocatalytic payload release is triggered by the salts surrounded the ***Capsule 1*** (blue). This is the same as the bulk triggering scenario. Therefore,

$$S_{capsule1}(t) = S_o + R_{capsule1}(t)\frac{mL}{MW_{salts}V} \qquad 7.9$$

$$R_{capsule1}(t) = \frac{R_0 - R_f}{1+\left(\frac{t}{F\left(A_0, S_o + R_{capsule1}(t)\frac{mL}{MW_{salts}V}\right)}\right)^n} + R_f \qquad 7.10$$

Here, $V = V_{capsule1}$, $m = m_{capsule1}$, so $R_{capsule1}(t)$ is determined by A_0, S_0, ρ, L, MW_{salts}, indicating a high density of microcapsule, a high loading efficiency of salts and a low molar mass ionic compound as encapsulant favors a faster payload release rate in ***Capsule 1,*** the initiation stage.

Next is the second stage, "the propagation microcapsule", ***Capsule 2*** (Figure 7.4). For this stage, we need to consider the geometry of the microcapsules and spatial distance of the

microcapsules array. Assume that the microcapsules are monodisperse and their radius is *r* and the distance between the centers of any two microcapsules is equal to l and the microcapsules are packed in a hexagonal pattern. The diffusion coefficient of the salts is $D_{\text{ion-solvent}}$. Therefore the concentration of salts that trigged ***Capsule 2*** is described by the Fick's second law,

$$\frac{\partial(R_{capsule1}(t)+S_0)}{\partial t} = D_{ion-solvent}\frac{\partial^2(R_{capsule1}(t)+S_0)}{\partial(l-2r)^2} \quad 7.11$$

For ***Capsule 2,***

$$S(t) = D_{ion-solvent}\frac{\partial^2(R_{capsule1}(t)+S_0)}{\partial(l-2r)^2} + R_{capsule2}(t) \quad 7.12$$

So, the payload release profiles for ***Capsules 2*** is

$$R_{capsule2}(t) = \frac{R_0 - R_f}{1+\left(\frac{t}{F(A_{0,}D_{ion-solvent}\frac{\partial^2(R(t)+S_0)}{\partial(l-2r)^2}+R_{capsule2}(t))}\right)^n} + R_f \quad 7.13$$

Therefore, in this scenario, the distance between microcapsules are critical to achieve auto-acceleration microcapsules. The boundary condition is that the concentration of salts that diffused to ***Capsules 2*** should be higher than the initial salts concentration S_0 that triggered payload release of ***Capsule 1.***

$$\frac{\partial(R_{capsule1}(t)+S_0)}{\partial t} = D_{ion-solvent}\frac{\partial^2(R_{capsule1}(t)+S_0)}{\partial(l-2r)^2} > \mathrm{S_o}$$

Therefore, the maximum distance between two microcapsules can be determined. Based on these equations, similarly, the release profiles of ***Capsules 3, 4, 5, ….***can also be deducted.

7.3.3 Challenges in Preparing Autocatalytic Microcapsules

One challenge for preparing the autocatalytic microcapsules is the limited ionic compound that can be encapsulated inside the cPPA microcapsules. This solvent evaporation method that based the oil-in-water single emulsion template favors a high boiling point, high viscosity payload such as jojoba oil. However, typically, these types of payloads has limited

solubility for salts that can reach desired concentration range. For example, to reach final concentration of 0.2 M LiCl with 20 mg microcapsules suspended in 1 mL methanol, a loading efficiency of 42 wt% of LiCl in microcapsules is required. Several attempts have been made to synthesize these microcapsules with LiCl dispersed in jojoba oil or glycerol, but these products have < 5wt% LiCl loaded and poor shell wall stability. Another attempt to improve the loading efficiency is to encapsulate quaternary ammonium compound with long alkane substitutes. In this case, the shell wall stability is still a concern as the ammonium compound resides in the shell wall during encapsulation. This could cause uncontrolled degradation of cPPA shell wall.[16] As the ionic compound is soluble in aqueous carrier, encapsulating ionic compound with double emulsion method is more promising moving forward.

7.4 REFERENCES

(1) Salis, A.; Ninham, B. W. Models and Mechanisms of Hofmeister Effects in Electrolyte Solutions, and Colloid and Protein Systems Revisited. *Chem. Soc. Rev.* **2014**, *43*, 7358–7377.

(2) Lo Nostro, P.; Ninham, B. W. Hofmeister Phenomena: An Update on Ion Specificity in Biology. *Chem. Rev.* **2012**, *112*, 2286–2322.

(3) Kunz, W.; Lo Nostro, P.; Ninham, B. W. W. The Present State of Affairs with Hofmeister Effects. *Curr. Opin. Colloid Interface Sci.* **2004**, *9*, 1–18.

(4) Liu, L.; Kou, R.; Liu, G. Ion Specificities of Artificial Macromolecules. *Soft Matter* **2016**, *13*, 68–80.

(5) Xu, Y.; Liu, G. Amplification of Hofmeister Effect by Alcohols. *J. Phys. Chem. B* **2014**, *118*, 7450–7456.

(6) Liu, L.; Wang, T.; Liu, C.; Lin, K.; Ding, Y.; Liu, G.; Zhang, G. Mechanistic Insights into Ampli Fi Cation of Speci Fi c Ion E Ff Ect in Water – Nonaqueous Solvent Mixtures. *J. Phys. Chem. B* **2013**, *117*, 2535.

(7) Wang, T.; Liu, G.; Zhang, G.; Craig, V. S. J. Insights into Ion Specificity in Water – Methanol Mixtures via the Reentrant Behavior of Polymer. *Langmuir* **2012**, *28*, 1893–1899.

(8) Vrbka, L.; Jungwirth, P.; Bauduin, P.; Touraud, D.; Kunz, W. Specific Ion Effects at Protein Surfaces: A Molecular Dynamics Study of Bovine Pancreatic Trypsin Inhibitor and Horseradish Peroxidase in Selected Salt Solutions. *J. Phys. Chem. B.* **2006**, *110*, 7036–7043.

(9) Rembert, K. B.; Paterova, J.; Heyda, J.; Hilty, C.; Jungwirth, P.; Cremer, P. S. Molecular Mechanisms of Ion-Specific Effects on Proteins. *J. Am. Chem. Soc.* **2012**, *134*, 10039–10046.

(10) Jungwirth, P.; Tobias, D. J. Specific Ion Effects at the Air/Water Interface. *Chem. Rev.* **2006**, *106*, 1259–1281.

(11) Lund, M.; Vácha, R.; Jongwirth, P. Specific Ion Binding to Macromolecules: Effects of Hydrophobicity and Ion Pairing. *Langmuir* **2008**, *24*, 3387–3391.

(12) Lund, M.; Vrbka, L.; Jungwirth, P. Specific Ion Binding to Nonpolar Surface Patches of Proteins. *J. Am. Chem. Soc.* **2008**, *130*, 11582–11583.

(13) Heyda, J.; Okur, H. I.; Hladílková, J.; Rembert, K. B.; Hunn, W.; Yang, T.; Dzubiella, J.; Jungwirth, P.; Cremer, P. S. Guanidinium Can Both Cause and Prevent the Hydrophobic Collapse of Biomacromolecules. *J. Am. Chem. Soc.* **2017**, *139*, 863–870.

(14) Vrbka, L.; Vondrásek, J.; Jagoda-Cwiklik, B.; Vácha, R.; Jungwirth, P. Quantification and

Rationalization of the Higher Affinity of Sodium over Potassium to Protein Surfaces. *Proc. Natl. Acad. Sci.* **2006**, *103*, 15440–15444.

(15) Kim, S.-H.; Kim, J. W.; Cho, J.-C.; Weitz, D. Double-Emulsion Drops with Ultra-Thin Shells for Capsule Templates. *Lab Chip* **2011**, *11*, 3162–3166.

(16) Tang, L.; Moore, J. S. Unpublished results